UNIVERSITY OF CALIFORNIA SAN DIEGO

Turbulence and mixing at topographic boundaries

A dissertation submitted in partial satisfaction of the
requirements for the degree Doctor of Philosophy

in

Oceanography

by

Bethan Lily Wynne-Cattanach

Committee in charge:

Professor Matthew H. Alford, Chair
Professor Jennifer A. MacKinnon
Professor Sarah G. Purkey
Professor Sutanu Sarkar

2024

The Dissertation of Bethan Lily Wynne-Cattanach is approved, and it is acceptable in quality and form for publication on microfilm and electronically.

University of California San Diego

2024

EPIGRAPH

Bod y cynta' i weld y môr
yna'r agosa down
at ddarganfod yn llygad agored

yr arlais cyn inni ddidol
yr aeliau sydd rhwng nef a daear,
gwagle a gweilgi.

Awn yn llawen tua'i chwerthin:
cyrraedd at ymyl fflowns ei chwedlau,
tafodau glas yn traethu gwirebau.

Am ennyd syllwn heb allu deall
ble mae'r dyfnder, y dwyfol nad yw'n datgan
ei hun wrth swatio'n y dirgel.

A gweld o'r newydd, nad yw'r moroedd
yn llai mirain, er i longau ddryllio
ar greigiau, cans yno bydd y cyffro

sy'n iasu yn ein geni'n frau o'r newydd.
Gweld y môr gynta' yw'r cynta'
y down at ddarganfod gwir ryfeddod.

— *Menna Elfyn "Y cynta' I weld y môr (Seeing the Sea)"*

TABLE OF CONTENTS

LIST OF FIGURES

LIST OF TABLES

ACKNOWLEDGEMENTS

I would like to thank my advisor Matthew Alford for his constant kindness and support over the last 5 years. I am incredibly grateful for the knowledge, scientific insights and time that he has shared with me and for exemplifying what it means to be a scientist and a leader. I would like to acknowledge my committee, Jen MacKinnon, Sarah Purkey and Sutanu Sarkar for their feedback and support as I have progressed through my PhD. I would also like to thank Gunnar Voet for his invaluable contributions to all three of my chapters. I am grateful to all of my other co-authors: Nicole Couto, Arnaud Le Boyer, Henri Drake, Raffaele Ferrari, Xiaozhou Ruan, Kurt Polzin, Alberto Naveira Garabato, Carl Spingys, Hans van Haren, Herlé Mercier and Marie-José Messias. Thank you for the insights and comments over many zoom meetings and drafts and for demonstrating the importance and benefits of scientific collaboration. Participating in a project like BLT has been an honour.

I have been lucky enough to spend several months of the last few years at sea and I owe my new-found love of sea-going research to the Captain and crews of the RRS Discovery and thank them for welcoming us so warmly onboard and providing a fun and safe environment in which to do science.

Of vital importance to my experience and the smooth-running of our experiments has been the wonderful, talented team of engineers in MOD. Thank you to Sara Goheen, Helen Dufel, San Nguyen, Mike Goldin, Jonny Ladner, Spencer Kawamoto and all the other engineers and technicians who keep our instruments working and our morale high while at sea. I would also like to thank all the other PIs, students and post docs in MOD for creating such a warm and rich scientific environment. My journey into oceanography would not have happened if it weren't for Mattias Green at Bangor University. Thank you for sharing your excitement for science and encouraging me to pursue this path.

My experience at Scripps would not have been the same without the wonderful

group of scientists I was lucky enough to have in my cohort. I would like to thank my local support group in NH101 for making me feel like I had found my people as we worked through problem sets and counted pelicans together.

To Pascal, Linnea, Tricia, Duncan, Athina and Max for being there every Wednesday to talk through the ups and downs of graduate school, British baking and the world we live in. I am lucky to have friendships that cross oceans and continents and am grateful to Elin, Ffion, Gareth, Kate, Clare, Hannah, Tim, Max, Mark, Niall, Pearse and many others for helping me to reach graduate school in the first place and for making lockdowns and a pandemic bearable.

A very special thank you to my family. To my parents for encouraging my curiosity, creativity and for your constant love and support. To my brother Kieran, I am so incredibly proud to be your sister, thank you for always reminding me of what is important.

Finally, thank you to Alex for everything over the past 5 years, I'm not sure how I would have made it through without you.

Chapter 1, in full, is a reprint of the material as it appears in Journal of Geophysical Research: Oceans 2022. DOI:10.1029/2022JC018674. Wynne-Cattanach, Bethan L.; Alford, Matthew H., MacKinnon, Jennifer A.,Voet, Gunnar. The dissertation author was the primary investigator and author of this paper.

Chapter 2, in full, has been submitted for publication of the material as it may appear in Nature, 2024, Wynne-Cattanach, Bethan L., Couto, Nicole, Drake, Henri F., Ferrari, Raffaele, Le Boyer, Arnaud, Mercier, Herlé, Messias, Marie-José, Ruan, Xiaozhou, Spingys, Carl P., van Haren, Hans, Voet, Gunnar, Polzin, Kurt L, Naveira Garabato, Alberto and Alford, Matthew H.. The dissertation author was the primary investigator and author of this paper.

Chapter 3, in part, is currently being prepared for submission for publication of the material. Wynne-Cattanach, Bethan L., Alford, Matthew H., Voet, Gunnar, Le Boyer,

Arnaud, Couto, Nicole, Naveira Garabato, Alberto, Spingys, Carl P., Polzin, Kurt L. and van Haren, Hans. The dissertation author was the primary investigator and author of this material.

VITA

2017	Bachelor of Arts, School of Mathematics, Trinity College, University of Dublin
2018	Master of Science, School of Ocean Sciences, Bangor University
2024	Doctor of Philosophy, Scripps Institution of Oceanography, University of California San Diego

PUBLICATIONS

Wynne-Cattanach, Bethan L., Nicole Couto, Henri F., Raffaele Ferrari, Arnaud Le Boyer, Herle Mercier, Marie José Messias, Xiaozhou Ruan, Carl P. Spingys, Hans van Haren, Gunnar Voet, Kurt L. Polzin, Alberto Naveira Garabato, Matthew H. Alford. "Observational evidence of diapycnal upwelling within a sloping submarine canyon." *Nature* (2024, in review).

Alford, Matthew H., **Bethan Wynne-Cattanach**; Arnaud Le Boyer; Nicole Couto; Gunnar Voet; Carl Spingys; Bieito Fernandez Castro; Alex Forryan; Alberto Naveira-Garabato. "Buoyancy flux and mixing efficiency from direct, near-bottom turbulence measurements in a submarine canyon." *Journal of Physical Oceanography* (2024, submitted)

van Haren, Hans, Gunnar Voet, Matthew H. Alford, Bieto Fernández-Castro, Alberto Naveira Garabato, **Bethan L. Wynne-Cattanach**, Herle Mercier, Marie José Messias. "Near-slope turbulence in a Rockall canyon." *Deep Sea Research: Part I* (2024, in review).

Wynne-Cattanach, Bethan L., Matthew H. Alford, Jennifer A. MacKinnon, and Gunnar Voet. "Measurements of Turbulence Generated by Wake Eddies Near a Steep Headland." *Journal of Geophysical Research: Oceans* 127, no. 8 (2022): e2022JC018674.

Couchman, Miles M.P., **Bethan L. Wynne-Cattanach**, Matthew H. Alford, Colm-cille P. Caulfield, Rich R. Kerswell, Jennifer A. MacKinnon, and Gunnar Voet. "Data-Driven Identification of Turbulent Oceanic Mixing From Observational Microstructure Data." *Geophysical Research Letters* 48, no. 23 (2021): e2021GL094978.

ABSTRACT OF THE DISSERTATION

Turbulence and mixing at topographic boundaries

by

Bethan Lily Wynne-Cattanach

Doctor of Philosophy in Oceanography

University of California San Diego, 2024

Professor Matthew H. Alford, Chair

Internal tides and currents interacting with sub-surface topography such as continental slopes, islands and seamounts give rise to turbulent processes. The subsequent mixing of waters of different densities is important for maintaining the global overturning circulation. This thesis investigates the turbulent processes occurring at two different topographic features; a steep headland in the eastern Pacific and a continental slope canyon in the north-west Atlantic.

Tidal currents and mean-flows interacting with headlands and islands give rice to turbulent wakes. In Chapter 1, surveys in the wake of a steep headland in both tidal and mean flow regimes reveal turbulent wakes driven by shear and vorticity in the

flow. Recent theoretical literature has suggested that turbulence at steep topographic features may drive upwelling necessary to close the abyssal overturning circulation. In Chapter 2, a novel near-bottom dye release within a steep canyon provides the first direct evidence of this upwelling and suggests that current 1-d models of near-bottom processes are insufficient to understand the importance of bottom boundary upwelling processes. In Chapter 3, this work is extended using a suite of moorings which observe convergence and divergence in the along-canyon direction indicative of exchange between the boundary and interior, a process that is not included in 1-d models.

Introduction

Turbulence, and the subsequent mixing of water properties, play important roles in regulating the global climate and ecosystems, modifying the distribution of heat, salt, nutrients, carbon dioxide and other important tracers. Understanding the geography of ocean turbulence is therefore vital for our ability to model the climate and predict its impact on biodiversity.

Work to understand the global distribution of mixing began in the 1960s. In particular, Walter Munk's seminal work "Abyssal Recipes" used full-depth profiles in the deep ocean to infer that a constant eddy diffusivity and upwelling velocity would be sufficient to maintain the vertical distributions of the measured tracers. Munk 1966 suggested that internal tides may drive this mixing in the ocean interior.

The 1980s and 90s saw the development of tools and methods for estimating the eddy diffusivity from turbulent microstructure. These studies found diffusivities an order of magnitude smaller than the value predicted by Munk (Moum and Osborn 1986; Gregg 1989; Ledwell et al. 1993; Toole et al. 1994; Kunze and Sanford 1996) However, observations also showed that the diffusivity was not constant as Munk had predicted, instead suggesting that mixing was enhanced near rough topography and features (Toole et al. 1994; Lueck and Mudge 1997; Polzin et al. 1997; Ledwell et al. 2000; St. Laurent et al. 2001; Toole 2007; Waterhouse et al. 2014).

In contrast to Munk 1966's hypothesis, the observed mixing profile that increases towards the seafloor instead suggests that waters downwell in the interior (Polzin et al. 1997). A water parcel that experiences more mixing from below than above in a

stably stratified ocean will become denser and will therefore sink. It is an open question where the upwelling occurs, but recent theoretical work suggests that the water mass transformation is confined to bottom boundary layers (BBLs) along steeply sloping topography. At the boundary, turbulent buoyancy fluxes must decrease to zero to satisfy the no flux boundary condition, therefore a parcel of water experiences more mixing from above than below, and thus upwells ((Ferrari et al. 2016; McDougall and Ferrari 2017).

Tracer releases, microstructure measurements and numerical simulations completed as part of the BBTRE and DIMES experiments demonstrate that downwelling occurs in the interior and that close to topography water is upwelled (Ledwell et al. 2000; St. Laurent et al. 2001; Mashayek et al. 2017). In both of these experiments, the tracers were released within the interior, at least 500 m above the nearby topography. The tracer was advected into the BBL by lateral motions. The vertical velocity estimated from the tracer is therefore the net velocity over a period where the tracer was in the BBL and the interior and does not directly tell us about the upwelling in the BBL. Microstructure measurements in these experiments were no closer than 20m from the bottom, therefore, may not fully capture the turbulence within the BBL.

Mixing at topographic boundaries is able to return deep water formed at the poles to the surface, a key branch of the overturning circulation. Small scale processes near topography play a significant role in maintaining the general ocean circulation and closing the global energy budget (Munk and Wunsch 1998; Wunsch and Ferrari 2004). Where exactly the mixing occurs has implications for the formation and circulation of abyssal waters (Saenko and Merryfield 2005; Melet et al. 2013).

Relevant topographic features include ridges (Rudnick et al. 2003; Voet et al. 2020; Musgrave et al. 2016), seamounts (Lueck and Mudge 1997; Armi 1978; Carter et al. 2006), continental slopes (Nash et al. 2004; Klymak et al. 2011), canyons (Lee et al. 2009; Gregg et al. 2011; Zhao et al. 2012; Wain et al. 2013; Alford and MacCready 2014; Waterhouse

et al. 2017; Alberty et al. 2017; Hamann et al. 2019), headlands (Edwards et al. 2004; Chang et al. 2013) and abyssal hills (Ledwell et al. 2000). Mixing at topography is largely driven by the dissipation of internal waves that are either generated locally (Nikurashin and Legg 2011), or remotely (Klymak et al. 2010).

In the coastal ocean, vertical transport of nutrients is important for biological productivity in the regions. Wind-driven upwelling is particularly prevalent along eastern boundaries (Brink 2016). However, topographic features such as headlands and islands can also influence the upwelling within coastal regions (Heywood et al. 1990; Roughan et al. 2005; Gove et al. 2016). At large Reynolds number ($Re = \frac{UD}{\nu}$ where U is the upstream velocity, D is the size of the obstacle and ν is the viscosity) flow past an object separates from the boundary, generating a turbulent wake behind the object. Observations and numerical simulations provide evidence of mixing and upwelling of cold, nutrient-rich water within the wakes of headlands and islands (Deleersnijder et al. 1992; Wolanski et al. 1996; Johnston and Read 2007; Chang et al. 2013). The structure of the wake and the distribution of vorticity can be altered by variability in the upstream flow (Geyer and Signell 1990; Signell and Geyer 1991; Mackinnon et al. 2019), the shape and size of the obstacle (Signell and Geyer 1991) and the local stratification (Lin and Pao 1979; Perfect et al. 2018).

However, measurements of turbulent microstructure are limited near topographic features due to the difficulty of sampling so close to the seafloor. Understanding the spatial distribution of turbulence and mixing within the bottom boundary layer, and at topographic features such as headlands is crucial to our understanding of how important tracers are transported.

The general objective of this work is to explore the turbulent dynamics resulting from flow-topography interactions to help inform our understanding of their effect on larger-scale processes. This thesis will be comprised of three chapters. The first will address the turbulence generated in the wake of an island during the Flow Encountering

Abrupt Topography experiment. The second and third chapters will be analyses of data sets that were collected as part of the first leg of the Boundary Layer Turbulence and Abyssal Recipes field program.

Background

Estimates of turbulence

Dissipation of Turbulent Kinetic Energy

When looking at turbulence in the ocean, it is common to use the Reynold's decomposition and assume that a flow field $\mathbf{U}$ can be separated into a mean component $\overline{\mathbf{u}}$ and a fluctuating, or turbulent, component $\mathbf{u}'$ such that $\mathbf{U} = \overline{\mathbf{u}} + \mathbf{u}'$. Turbulence is characterised by a non-zero turbulent kinetic energy (TKE), $KE_{\text{turb}} = \frac{1}{2}\overline{\mathbf{u}'^2}$. The evolution of TKE is described (in Einstein notation) by

$$\left(\frac{\partial}{\partial t} + \bar{U}_j \frac{d}{dx_j}\right)\overline{u_i'^2} = \frac{\partial}{\partial x_j}\left(-\frac{1}{\rho_0}\overline{u_i' p'}\delta_{i,j} + \nu\frac{\partial}{\partial x_j}\frac{\overline{u_i'^2}}{2} - \overline{u_j' u_i' u_i'}\right) \underbrace{-\nu\left(\frac{\partial u_i'}{\partial x_j}\right)^2}_{\epsilon} \underbrace{-\overline{u_j' u_i'}\frac{\partial}{\partial x_j}\overline{U_i}}_{P} + \underbrace{\overline{b'w'}}_{B} \tag{1}$$

The first two terms on the right hand side describe the transport of TKE, the third describes the dissipation of TKE, the fourth describes the production of TKE and the fifth describes the buoyancy flux. Osborn 1980 assumed that the transport terms could be neglected, therefore in a steady state we have the balance

$$\epsilon = P + B \tag{2}$$

The mixing efficiency is defined as the ratio of energy lost to potential energy to the total energy lost and is given by

$$R_f = \frac{B}{B + \epsilon}. \tag{3}$$

Parametrising the buoyancy flux by the eddy diffusivity ($B = -K_\rho N^2$) gives

$$K_\rho = \frac{R_f \epsilon}{(1 - R_f) N^2} \tag{4}$$

where $\frac{R_f}{(1-R_f)}$ is known as the mixing coefficient Γ (Polzin et al. 2014). The buoyancy flux can thus be written as

$$B = \Gamma \epsilon \tag{5}$$

where Γ is the mixing efficiency and, based on laboratory and numerical experiments, is often assumed to be approximately 0.2 (Peltier and Caulfield 2003). However, this value may vary, particularly in the abyssal ocean near topographic features Mashayek et al. 2017 and can depend on the mixing mechanism (Chalamalla and Sarkar 2015; Ivey et al. 2021). A variable mixing efficiency is necessary for the buoyancy flux to decrease to zero within the BBL (Ferrari et al. 2016) and has significant implications on the global overturning circulation (Cimoli et al. 2019).

Dissipation of Thermal Variance

When interested in the mixing of a passive scalar, such as temperature, by turbulence we can consider the advection-diffusion equation for the fluctuating part of the temperature field. The temperature can be decomposed in a similar way to the velocity as $T = \overline{T} + T'$. The evolution equation for the temperature variance is given by

$$\left(\frac{\partial}{\partial t} + \overline{\mathbf{U}} \cdot \nabla\right) \frac{\overline{T'^2}}{2} = \kappa \nabla^2 \frac{\overline{T'^2}}{2} - \nabla \cdot \overline{\mathbf{u}' T'^2 / 2} - \underbrace{\overline{T' \mathbf{u}'} \cdot \nabla \bar{T}}_{\frac{P_T}{2}} - \underbrace{\kappa \overline{\nabla T' \cdot \nabla T'}}_{\frac{\chi_T}{2}}. \tag{6}$$

Again, the first two terms on the right hand side describe the transport. The production of temperature variance is given by the third term and the dissipation of tracer variance is given by the fourth term. Osborn and Cox 1972 assumed that there is a balance

between production and dissipation of thermal variance such that

$$\chi_T = P_T. \tag{7}$$

Assuming that horizontal gradients are negligible, this gives

$$-2\overline{w'T'}\frac{\partial \overline{T}}{\partial z} = 2\kappa\overline{\nabla T' \cdot \nabla T'} \tag{8}$$

where $\overline{w'T'}$ is the vertical heat flux and can be parameterised by the eddy diffusivity as

$$\overline{w'T'} = -K_T\frac{\partial \overline{T}}{\partial z} \tag{9}$$

Therefore,

$$K_T = \frac{\chi_T}{2(\partial\overline{T}/\partial z)^2}. \tag{10}$$

Further assuming that $K_\rho = K_T$ means that we can obtain estimates of ϵ from χ as

$$\epsilon_\chi = \frac{N^2\chi_T}{2\Gamma T_z^2}. \tag{11}$$

or estimates of the buoyancy flux as

$$B = -\frac{\chi_T}{2\frac{\partial T}{\partial z}}. \tag{12}$$

Non-dimensional Parameters

Richardson Number

The Richardson number, defined as $Ri^{-1} = \frac{S^2}{N^2}$ where $N^2 = -\frac{g}{\rho_0}\frac{\partial \rho}{\partial z}$ is the stratification and $S^2 = (\frac{\partial u}{\partial z})^2 + (\frac{\partial v}{\partial z})^2$ is the squared shear, describes the tendency for a Kelvin-Helmholtz instability to occur. It has been shown in an inviscid, stably stratified fluid

that the flow will be unstable when $Ri < 1/4$ (Miles 1961; Miles and Howard 1964).

Rossby Number

The Rossby number is the ratio of inertial forces to the local Coriolis force and describes the strength of the local vorticity relative to Coriolis. Rossby number is given by $Ro = \frac{v_x - u_y}{f}$ where v_x is the partial derivative of the meridional velocity with respect to the zonal direction, u_y is the partial derivative of the zonal velocity with respect to the meridional direction, $v_x - u_y$ is the vorticity and f is the local inertial frequency.

Mixing Mechanisms

Shear driven mixing

Vertically sheared flow in the stratified ocean can lead to turbulence when the sheared flow is able to overcome the tendency for fluid to remain stratified. The resulting instability, known as a Kelvin-Helmholtz (K-H) intability, is common throughout the ocean (Geyer et al. 2010). The Richardson number will be used to aid in identifying shear instabilities.

Convective mixing

Convective mixing occurs where denser water is moved above lighter water, causing the density profile to be gravitationally unstable. Convective events in the BBL may be driven by the transport of dense water over light water by a sheared flow on a slope (Seim and Fer 2011; Lorke et al. 2005).

Chapter 1

Measurements of turbulence generated by wake eddies near a steep headland

Tidal and low-frequency flows interact with abrupt topographic features, giving rise to a variety of small-scale phenomena including lee waves, vortical motions and turbulence. With the goal of identifying the processes that transfer momentum and energy between the larger-scale and smaller-scale flows, detailed tidally-resolving shipboard surveys were conducted near a sharp and steep headland north of Velasco Reef, Palau, in the Western Pacific. We present velocity, microstructure and rapid-cycling Conductivity, Temperature and Depth (CTD) measurements, contextualized with a nearby 10-month moored record, to examine wake and vortex structures. Observed flow near Velasco Reef was layered and multi-directional in depth such that the “downstream" side of the headland depended on depth. Downstream of the headland, during a period where mean flow dominated over the tide in the top 100 m of the water column, turbulent kinetic energy dissipation rates were enhanced by up to 3 orders of magnitude relative to those upstream. During a period dominated by tides, the flow reversed periodically and wake eddies were associated with turbulent dissipation rates up to $O(10^{-5})$ W kg^{-1}. Turbulent dissipation rates in the wake increased with inverse Richardson number for both tidal and mean flows past the headland, and were larger for stronger vorticity flows. Our analysis suggests that the eddies themselves lead to shear instabilities

and subsequent turbulence, either through tilting or their limited vertical extent. We associate the enhanced downstream dissipation with a combination of breaking internal tides and either these eddy processes or a multi-scaled turbulent wake.

1.1 Introduction

Currents impinging on islands, headlands and submarine ridges can lead to the generation of vortices and internal waves downstream (Edwards et al. 2004; Chang et al. 2013). These processes and the eventual transition to turbulence lead to the loss of kinetic energy and momentum in the wake and weaken the incident currents (Wolanski et al. 1984; Johnston et al. 2019). The vertical transport generated by mixing in the wake has been seen to increase chlorophyll concentrations and may also enhance biological productivity in the region (Heywood et al. 1990; Gove et al. 2016). It is therefore important to understand the turbulence and mixing generated in the lee of topographic features such as islands and headlands.

This study was motivated by observations collected around Velasco Reef, a promontory at the northern end of the Pacific archipelago of Palau. The complex topography at this location, consisting of both a steep headland and a deep water ridge, leads to the formation of both wake eddies (Mackinnon et al. 2019) and lee waves (Voet et al. 2020). We are interested in understanding how these wake processes may head to turbulence downstream of the headland.

Previous observations of turbulence at headlands and islands have often focused on measurements in the immediate vicinity of topographic obstacles to quantify the turbulent drag leading to flow separation (Edwards et al. 2004; Mackinnon et al. 2019). The few observational studies that have collected measurements of turbulent dissipation in the wake of a headland or island have shown an association between dissipation and shear (Chang et al. 2013; Wijesekera et al. 2020).

While several studies have shown evidence of flow separation and eddy formation (Geyer and Signell 1990; Heywood et al. 1996; Mackinnon et al. 2019), limited observational efforts have attempted to understand the processes generating turbulence within topographic wakes. Modelling wake processes is also limited since abrupt topographic features like headlands and islands are often poorly represented and therefore the resulting small-scale turbulent dynamics are not well parametrised.

Flow separates from topography due to the frictional forces acting on the current as it passes the body. In the idealised conditions of flow past a cylinder the resulting dynamics downstream can be characterised using the Reynolds number ($Re = \frac{UD}{\nu}$). This parameter is dependent only on the diameter of the obstacle (D), the velocity upstream (U) and the molecular viscosity (ν). It expresses the balance between the inertial and viscous forces in the horizontal momentum equation. At geophysical scales such as those relevant for flow past an island, an effective Reynolds number is commonly used (Re_{eff}) where the molecular viscosity is replaced with a variable eddy viscosity, A_z (Pattiaratchi et al. 1987; Heywood et al. 1990; Chang et al. 2013). At large enough Re_{eff}, flow separation occurs and eddies are shed. As Re_{eff} increases further the wake becomes increasingly unsteady and turbulent. The eddy viscosity relevant for flow separation at Velasco Reef is likely set by near-bottom turbulence and places the wake in a potentially eddy-shedding regime (Mackinnon et al. 2019).

Regions of vorticity generation, such as topographic wakes, are susceptible to centrifugal-symmetric instabilities (CSIs) (Molemaker et al. 2015). Flows become unstable to CSIs when the Ertel potential vorticity (q) is the opposite sign to the local Coriolis frequency (f). That is, $qf < 0$ where

$$q = \nabla b \cdot (\nabla \times \boldsymbol{u} + \boldsymbol{f}), \tag{1.1}$$

b is the buoyancy and $\boldsymbol{u}$ is the velocity vector (Haine and Marshall 1998). In thermal

wind balance, Equation 1.1 can be rewritten as

$$q = \frac{1}{N^2 f}(1 + Ro - Ri^{-1}) \tag{1.2}$$

where $N^2 = -\frac{g}{\rho_0}\frac{\partial \rho}{\partial z}$ is the stratification, $Ro = \frac{\zeta}{f}$ is the Rossby number, ζ is the vertical vorticity, $Ri^{-1} = \frac{S^2}{N^2}$ is the inverse Richardson number and $S^2 = (\frac{\partial u}{\partial z})^2 + (\frac{\partial v}{\partial z})^2$ is the squared shear. Therefore, in the northern hemisphere regions where $Ri^{-1} > 1 + Ro$ are susceptible to CSIs.

The currents incident on Velasco Reef have both a mean and tidal component (Mackinnon et al. 2019). Velocity measurements around headlands in oscillatory tidal flows have shown that the lee eddy structures are highly time dependent, with asymmetric wakes on either side of the headland (Geyer and Signell 1990; Mackinnon et al. 2019). The presence of a baroclinic tide, generated when the barotropic tide forces stratified water over topography (Llewellyn Smith and Young 2003; Klymak and Gregg 2004; Nash et al. 2006), can introduce vertical shear that leads to the tilting of wake vortices (Farmer et al. 2002; Pawlak et al. 2003; Canals et al. 2009). Tilted vortices may dissipate faster than vertically aligned vortices either by generating enough vertical shear to overcome the stratification or through overturns due to the resulting horizontal component of the vorticity (Pawlak et al. 2003; Boulanger et al. 2007; Canals et al. 2009; Meunier et al. 2010). The tendency for overturning to occur can be described using the inverse Richardson number. In particular, for $Ri^{-1} > 4$, shear dominates over stratification, leading to Kelvin-Helmholtz instabilities and turbulent mixing (Miles 1961; Miles and Howard 1964).

Enhanced turbulence at topographic features may also be attributed to the internal tide. Turbulent dissipation can occur close to the generation site of the internal tide via non-linear wave-wave interactions (Polzin 2004; Nikurashin and Legg 2011), convective overturns (Klymak et al. 2008; Alford et al. 2011; Chalamalla and Sarkar 2015), and strain

Table 1.1. Overview of hypotheses for mechanisms generating turbulence in a geophysical wake, the relevant parameters and the expected relationship between the dissipation rate of turbulent kinetic energy (ϵ), the Rossby number (Ro) and the inverse Richardson number (Ri^{-1}).

	Processes	**Important parameters**	**Expectation**
I	Flow separation with a turbulent wake and no coherent vortices.	Re_{eff}	ϵ is not a function of Ri^{-1} nor Ro. No coherent eddies are visible.
II	Wake contains turbulence and coherent vortices.	Re_{eff}, Ro	ϵ is a function of Ro, not Ri^{-1}. Re_{eff} less than in (I).
III	Turbulence driven by vertical shear due to the eddies themselves.	Ro, Ri^{-1}	Ro and Ri^{-1} correlated. ϵ is a function of both Ro and Ri^{-1}.
IV	Turbulence is due to lateral instabilities of eddies.	Ro	ϵ is enhanced when $q = 1 + Ro - Ri^{-1} < 0$
V	Breaking internal tides dominate.	Ri^{-1}	ϵ is a function of Ri^{-1} and Ro is irrelevant.

as isopycnals are heaved up and down (Klymak et al. 2008). Remotely generated low mode internal tides interacting with steep slopes (Nash et al. 2004; Klymak et al. 2011) can lead to turbulence. The internal tide can also generate shear instabilities (Lien and Gregg 2000).

As briefly summarised above, turbulence can be generated in several ways when flow encounters complex topography. However, it can be challenging to isolate specific mechanisms with observations. Here, we use direct measurements of the dissipation rate of turbulent kinetic energy (hence forth referred to as "turbulent dissipation" or ϵ) and estimates of the Rossby Number and inverse Richardson number to identify the dominant processes leading to turbulence generation around Velasco Reef. Five hypotheses for the possible mechanisms emerge from the literature. We classify each process based on the relationship between ϵ, Ro and Ri^{-1} in each case (Table 1.1).

The observations presented here were collected during two different flow regimes. The first was a mean flow scenario where we observed dominant eastward mean flow in the upper 100m of the water column. The second was a tidal regime where flow oscillated between eastward and westward past Velasco Reef. We discuss the turbulent dissipation observed in both scenarios and identify the dominant processes generating turbulence in the wake. The structure of the paper is as follows. In Section 1.2 we describe the data and the methods used for data collection and analysis. In Section 1.3.1 we describe the background flow conditions. Section 1.3.2 discusses the mean flow scenario and we describe the resulting turbulence. The tidal scenario is discussed in Section 1.3.3 and we highlight the formation of vortices at the headland. Section 1.4 discusses the relationship between the observed turbulent dissipation rate and inverse Richardson number and Rossby number and we suggest which of the hypotheses in Table 1.1 are most likely given our observations. Finally, Section 1.5 summarises the work.

1.2 Data & Methods

The data presented in this study were collected at Velasco Reef, Palau as part of the Flow Encountering Abrupt Topography (FLEAT) project funded by the Office of Naval Research. The purpose of the FLEAT program was to improve understanding of the processes occurring when ocean currents encounter islands and ridges. Particularly, how energy and momentum from these large-scale currents is lost and transferred to smaller scales and eventually, to turbulence. The archipelago of Palau was chosen as the focus region for FLEAT due to its location in the path of the westward flowing North Equatorial Current (NEC) and the eastward flowing North Equatorial Counter Current (NECC) (Schönau and Rudnick 2015). These meandering currents cause variability in the large scale flow hitting the islands (Simmons et al. 2019) that, in turn, influence the

wake downstream (Zeiden et al. 2019). At smaller scales, tidal and near-inertial motions interact with the islands and reefs of Palau (Mackinnon et al. 2019; Siegelman et al. 2019). Together, these create a varying broadband incident current that leads to temporal and spatial variability in the turbulence and dynamics produced when the flow interacts with the islands (Mackinnon et al. 2019; Merrifield et al. 2019; St. Laurent et al. 2019; Wijesekera et al. 2020). The northern end of Palau is topographically complex, with both a headland and a ridge. Both tidal lee waves, generated by flow over the ridge, and wake eddies, shed from the tip of the headland, were expected. The connection between internal tides near topography and wave breaking has been noted several times (Rudnick et al. 2003; Klymak et al. 2012; Nagai and Hibiya 2015; Alford et al. 2015), including here at Velasco Reef (Voet et al. 2020), therefore our focuses in this paper are the additional processes that are simultaneously occurring; namely, lateral processes associated with flow separation and vortex shedding.

Velasco Reef is a steep-sided sunken atoll rising up from depths exceeding 3000 m to $15-20$ m at the rim of the lagoon. A ridge extends northward from the northern tip of the reef, with a water depth of approximately 1000 m at the top of the ridge. The eastern flank of the ridge is very steep, dropping to $\sim$ 3000 m depth in less than 4 km. The western flank is less steep, reaching depths of $\sim$ 2000 m in approximately 8 km (Figure 1.1). This study focuses on the region surrounding the northern tip of the reef.

Shipboard observations were conducted in the vicinity of Velasco Reef to measure the variety of processes present here (Figure 1.1). Turbulent dissipation rate was measured directly using the Modular Microstructure Profiler (Alford and Gregg 2001). Additionally, indirect estimates of turbulence were made from the inertial subrange of microconductivity measured with the FastCTD system (Alford and Pinkel 2000a; Moum and Nash 2009). The shipboard Acoustic Doppler Current Profilers (ADCPs) provided velocity measurements. A mooring offshore of the tip of the reef provided temporal context.

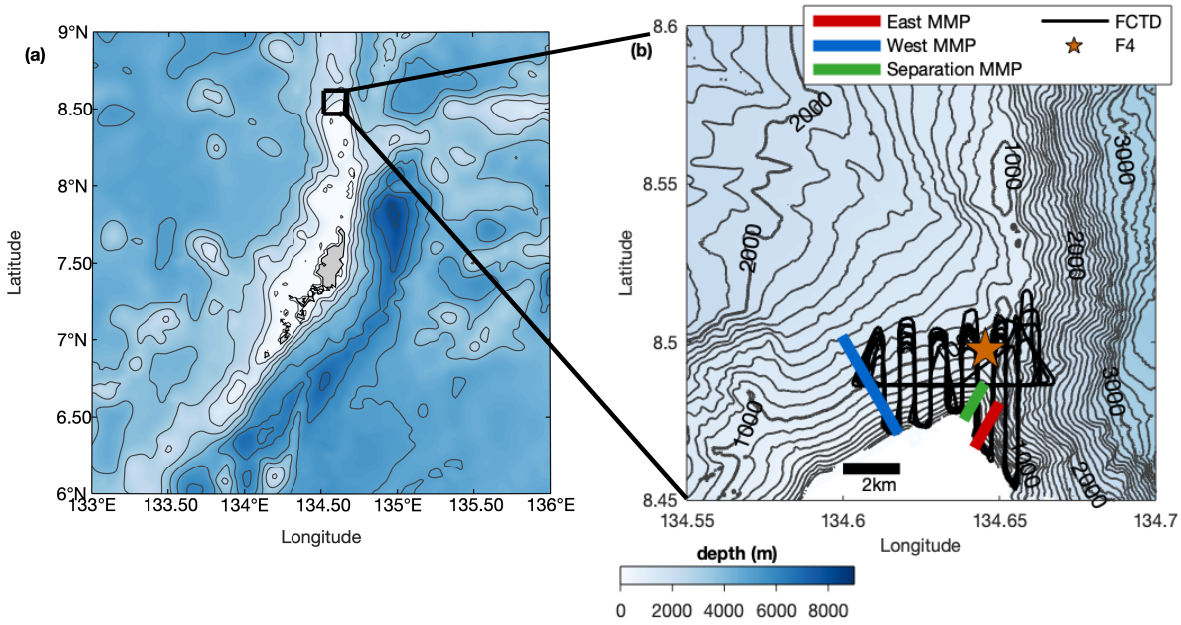

Figure 1.1. The full island chain of Palau is shown in (a) with the region of focus for this study marked with the black box. Contours show isobaths at 1000 m intervals. Observations used for this analysis are shown in (b). These include 3 sets of MMP microstructure lines, the FCTD radiator surveys and the F4 mooring located in 880 m of water. Thin grey contours show isobaths at 100 m intervals and thick grey contours show isobaths at 1000 m intervals.

1.2.1 Moorings

Background currents around Velasco Reef were measured by two arrays of moorings deployed from June 2016 to April 2017. Detailed discussion of the records from the various mooring sensors can be found in Mackinnon et al. (2019), Wijesekera et al. (2020) and Zeiden et al. (2021). For this study, we used velocity records from the F4 mooring, deployed due north of the headland in 880 m of water (Figure 1.1, star). We used the moored velocity records for the period June 9, 2016, to June 19, 2016, as context for the shipboard surveys (Figure 1.2). In the depth range relevant to this study, two ADCPs were mounted at around 60 m: an upward-looking 300 kHz RDI Workhorse Monitor and a downward-looking 75 kHz Workhorse Long Ranger.

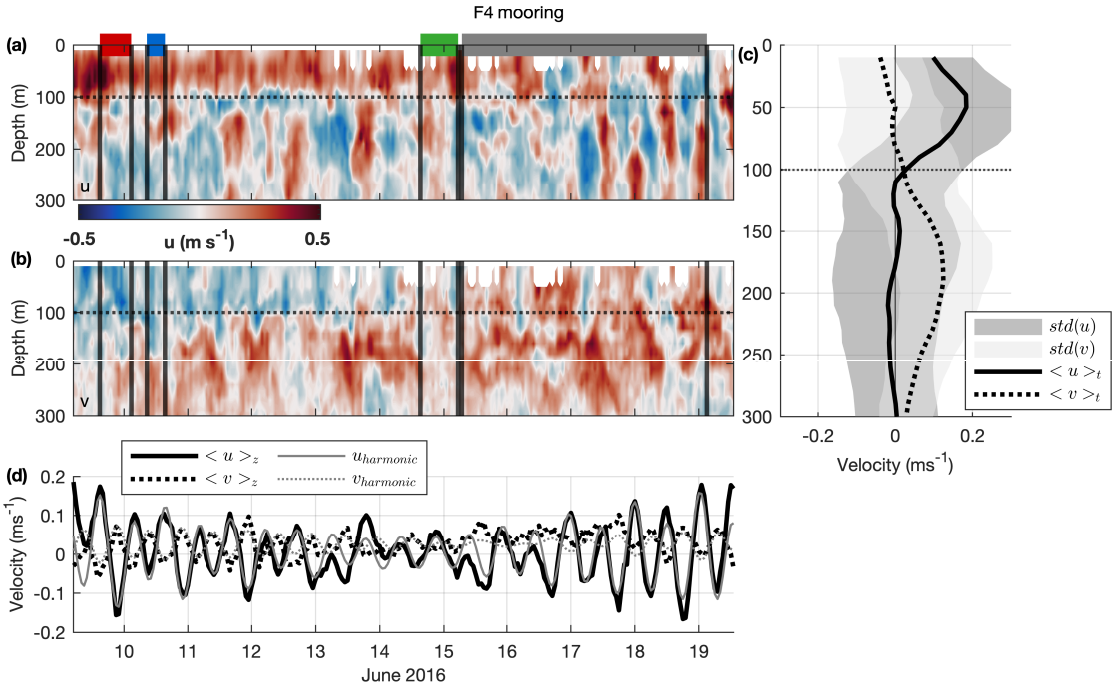

Figure 1.2. Time series of zonal velocity (a) and meridional velocity (b) at the F4 mooring for the duration of the repeat microstructure and FCTD measurements (June 9th-19th, 2016). Vertical lines indicate the start and end times of the separate microstructure lines (bar colours at the top correspond to those in Figure 1.1) and Fast CTD surveys (grey bar). The time average and standard deviation of u and v for the record from June 9th-19th 2016 are shown in (c). The depth averages of u and v are shown in (d) together with a harmonic fit to each velocity component using the tidal components M2, O1, K1 and S2. The dotted line at 100 m in (a), (b) and (c) marks the approximate boundary between the upper and lower layers.

1.2.2 MMP

The Modular Microstructure Profiler (MMP), developed by Mike Gregg at the Applied Physical Laboratory, University of Washington, and subsequently modernised and operated by the Multiscale Ocean Dynamics Group at Scripps Institution of Oceanography, is a tethered microstructure profiler (Alford and Gregg 2001; Hamann et al. 2018). It was equipped with a pumped Seabird CTD, an altimeter which allowed the instrument to be profiled to ~10 m above the bottom in shallow water, two airfoil shear probes and two FP07 thermistors. From the shear data we computed the dissipation

rate of turbulent kinetic energy (ϵ [W kg^{-1}]) in standard fashion as

$$\epsilon = 7.5\nu \int_{k_0}^{k_c} \phi_{u_z}^2(k)dk \tag{1.3}$$

where ϕ_{u_z} is the spectrum of the shear, ν is the kinematic viscosity and k is the vertical wavenumber. The shear spectrum was calculated over 0.5 m vertical bins for each profile and was then integrated between the lowest wavenumber k_0 and a cutoff wavenumber k_c. The cutoff was determined iteratively as the wavenumber where the Nasmyth universal spectrum reached 90% of its total variance (Wesson and Gregg 1994; Gregg 1998).

A total of 382 profiles collected along three offshore lines were used in this analysis. The lines started at the 50 m isobath and extended up to 4 km offshore. While water depths along the lines reached as deep as 1800 m the profiles only went to a maximum depth of 300 m, the instrument's pressure rating. The MMP provided centimeter scale resolution in the vertical and was dropped at 0.7 m s^{-1}. Horizontal resolution was highest in shallower water where profiles took less time. Maximum spacing between profiles was approximately 200 m along the line.

1.2.3 FastCTD

The FastCTD (FCTD) system (Klymak et al. 2008) consists of a rapid profiling tethered body attached to a direct drive, self rendering electric winch. A SBE49 CTD and a dual-needle microconductivity probe (an in-house version of the SBE7) were mounted on the instrument (Alford and Pinkel 2000a). The vehicle was allowed to free fall on the downcast at speeds of 3-5 ms^{-1}. Following Alford and Pinkel (2000a), we estimated the dissipation of thermal variance (χ) from the microconductivity profiles. Each value of χ was calculated over a 2-second segment of the profile. We then used the method described by Moum and Nash (2009) to estimate ϵ from χ, given by

$$\epsilon_\chi = \frac{N^2 \chi}{2\Gamma T_z^2}. \tag{1.4}$$

A cutoff of $T_z > 1 \times 10^{-4}$ °C m^{-1} was used in the calculation of ϵ_χ (Alford and Pinkel 2000a). While ϵ and ϵ_χ may differ due to both physical or sampling-related reasons (Gregg et al. 2018; Taylor et al. 2019; Couchman et al. 2021) agreement between ϵ and ϵ_χ computed from MMP data (not shown) was generally within a factor of 2.

1.2.4 Shipboard Velocity

Velocities along the ship surveys were measured from the Teledyne RDI 75 and 150 kHz ADCPs onboard the *R/V Revelle*. Data from the two instruments were combined to give a total depth range of 700 m with 8 m vertical resolution above 250 m and 16 m vertical resolution below. The velocity profiles were averaged to a 2-minute temporal resolution.

1.2.5 Sampling Strategy

To understand the various wake phenomena at Palau, as described in Section 1.1, both temporal and spatial information were necessary. Semi-diurnal and diurnal tides are both relevant at Palau (Figure 1.2d). Resolving the two tidal frequencies while also covering space required a combination of instruments. The MMP provided direct estimates of turbulence; however, the instrument profiled slowly so we were unable to cover large areas. The FCTD, on the other hand, was able to achieve ~6 times more horizontal resolution than the MMP owing to a much greater fall speed. Therefore, it was decided to limit the spatial extent of the MMP survey and focus on obtaining lines of MMP profiles that would enable us to resolve the tides. Three offshore lines were chosen around the north end of the reef. One on the eastern side, one on the western side and the third at the tip of the headland, where the flow was expected to separate (Figure 1.1). These will be referred to from here on as the east, west and separation lines

respectively. The profiles were done while steaming at 1 knot in the offshore direction, then the ship returned to the beginning of the line to repeat. The MMP observations spanned from June 9th to June 14th during which the east line was repeated 6 times, the separation line 8 times and the western line twice. The eastern and separation lines were repeated for 12 hours, giving coverage of one semi-diurnal tidal cycle. Note that the diurnal tide and near-inertial motions were aliased into the MMP signals (the local inertial period is 3.4 days). The separation line was occupied for a second time from June 19 to June 20. We omit these observations from this study because by this time the flow conditions had changed and are therefore not comparable to the other MMP measurements in the context of this study. However, discussion of the second occupation can be found in Mackinnon et al. (2019).

Following the MMP surveys, the FCTD was used to provide a more complete picture of the spatial variability in the dynamics around the headland. The ship completed a radiator pattern from east to west around the headland while steaming at 2.5-3 knots as the FCTD was profiled up and down (Figure 1.1). Profiles extended to 1400 m in deep water. The radiator was repeated 9 times from June 15-19th (Figure 1.2). Each radiator took 9 hours to complete. The length of the survey introduced space-time aliasing of higher frequency signals, such as the semi-diurnal tide, into the velocity and turbulent dissipation measurements presented in the remainder of this study. We can use a simple thought experiment to understand how the aliasing may present itself in our record. Consider a spatially uniform velocity field that varies at a semi-diurnal frequency in time. A 9 hour radiator through this velocity field will see variations in the velocity that appear to change with space. A survey from east to west beginning during the eastward phase of the tide will see eastward flow on the eastern side of the survey domain and westward flow on the western side of the survey domain. Our measurements showed similar features to this, with the added complexity of eddies that were shed from the headland during the different phases of the tide.

1.2.6 Calculation of Non-Dimensional Parameters

Inverse Richardson Number

For both the MMP and the FCTD, the inverse Richardson Number (Ri^{-1}) was estimated using velocity information from the shipboard ADCP and stratification from the Seabird CTD on board the instrument. We decided to use only the 8 m resolution portion of the shipboard ADCP record since 16 m was too coarse to capture the scale of the shear instabilities. The CTD data had a vertical resolution of 0.5 m. For the calculation of Ri^{-1}, the profiles of N^2 were gridded onto the same depth and time grid as the ADCP. The estimates of the inverse Richardson number were then calculated as $Ri_8^{-1} = \frac{S^2}{N_8^2}$. We use the subscript $(\cdot)_8$ to denote that our estimates have an 8 m vertical resolution.

Rossby Number

The Rossby number (Ro) was estimated from the shipboard ADCP velocities measured during the FCTD radiator survey. Data from each pass of the radiator were binned into 500 m (zonal) $\times$ 225 m (meridional) bins, centered around the latitudinal lines of the radiator pattern. Velocities within each bin were then averaged together. The gridded velocities were used to calculate the vorticity $\zeta = \frac{\partial v}{\partial x} - \frac{\partial u}{\partial y}$ and subsequently the two-dimensional Rossby number. While the aliasing described in Section 1.2.5 is apparent in the velocities, each estimate of the zonal gradient of the meridional velocity ($\frac{\partial v}{\partial x}$) was calculated from adjacent transects separated by approximately 1 hour and each eddy observed was covered by 2 to 3 sequential south-north transect lines. The Rossby number therefore provides a synoptic view of each eddy and is appropriate for our analysis which focuses on the statistics of the flow.

1.3 Results

1.3.1 Background Flow Conditions

Harmonic analysis of the F4 mooring record, done using T_TIDE (Pawlowicz et al. 2002), showed that both diurnal (O1, K1) and semi-diurnal (M2, S2) tides were important at Palau (Figure 1.2). The tidal flows followed the bathymetry around the northern end of Velasco Reef (Wijesekera et al. 2020). Although weaker than the tidal signals, near-inertial waves were also observed (Mackinnon et al. 2019; Siegelman et al. 2019). On average, flow was westward past Velasco Reef, consistent with the westward flow of the NEC. However, flow was strongly eastward at times, particularly in July 2016, as a result of interactions between the NEC, NECC and the bathymetry around Palau (Zeiden et al. 2021).

The barotropic (depth-averaged) currents from the mooring (Figure 1.2d) show that the strongest tidal currents occurred during the early MMP surveys and at the end of the FCTD record due to the spring/neap cycle. The FCTD sampling began shortly after neap tide when the maximum amplitude of the velocities were smaller. The time mean flow (Figure 1.2c) was layered and multi-directional in depth, and during this time period it consisted of two layers. The first was an eastward layer, with an average velocity magnitude of 0.12 m s^{-1} that reached from the surface to 100 m. Below this the mean flow was northward with an average velocity magnitude of 0.08 m s^{-1}.

From June 9th to 14th flow was southeastward in the upper 100 m. The mean current was strong enough that there was no flow reversal due to the tides. Below 100 m the mean flow was weak compared to the tides. From June 15th onward the zonal tidal flow overcame the mean current such that the current direction oscillated east and west. Over the course of the record the meridional component in the top 100 m transitioned from southward to northward.

We will discuss two different flow scenarios distinguished by the background

flow conditions. From June 9th to 15th the mean flow dominates in the upper layer; this will be the first scenario. After June 15th, the tide dominates.

1.3.2 Mean Flow Scenario

Despite the east and west MMP lines being done during spring tide and the separation line being done at neap tide, the mooring record showed that the surveys along the three MMP lines were completed during eastward zonal flow in the upper layer (Figure 1.2). The eastward flowing layer in the top 100 m was also present away from the mooring along all three lines (Figure 1.3). We therefore used the three sets of observations together to compare conditions upstream (west line), downstream (east line) and at the flow separation point (separation line). Observations from all transects of each line can be found in the Supporting Information.

The average values of Ri_8^{-1} are shown on the same 8 m vertical grid as the velocities. While Ri_8^{-1} at these vertical scales and averaged over several hours was not greater than the critical value of 4, the patterns provide physical intuition for where instabilities occur at smaller scales. On average the turbulent dissipation rate was highest at the eastern line in the upper 100 m levels up to $O(10^{-5})$ W kg^{-1} (Figure 1.3). This corresponds to the depth range where flow was eastward, placing the eastern line on the downstream side of the headland. Ri_8^{-1} also tended to be highest in the upper 100 m at the eastern line. The western line saw much weaker dissipation, in particular in the top 100 m where ϵ was between 10^{-9} and 10^{-8} Wkg^{-1}, up to 3 orders of magnitude less than upstream at the eastern line. The regions of increased Ri_8^{-1} at the western line were associated with bands of strong shear between layers. The turbulent dissipation at the separation line was high at all depths and decreased with distance offshore, as was also seen during the later occupation of the line (Mackinnon et al. 2019). Below 100 m, there was not a clear upstream side to the headland owing to the greater importance of the tidal over mean flows.

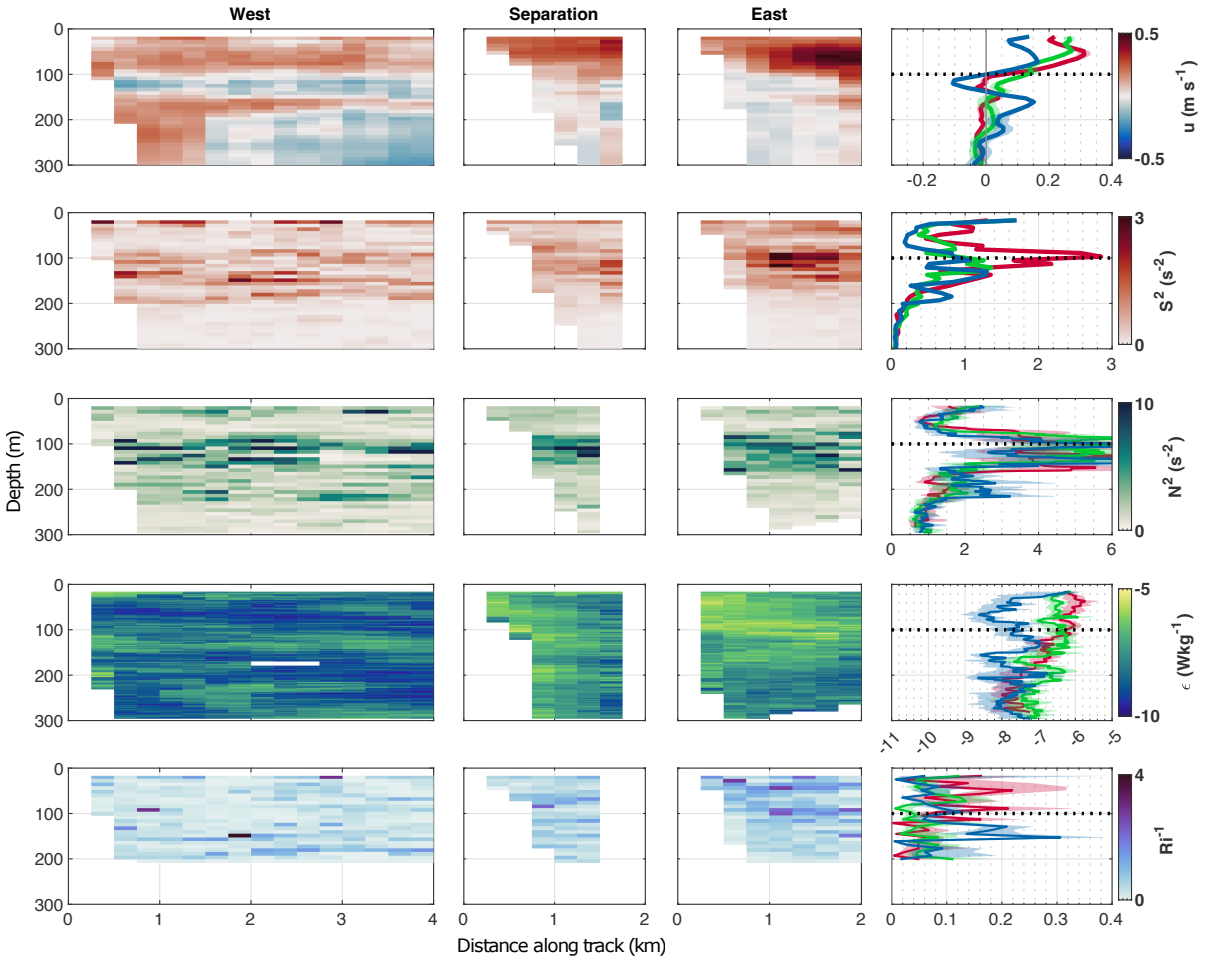

Figure 1.3. The West, Separation and East columns show the average (from top to bottom) meridional velocity, squared shear, stratification, turbulent dissipation rate and Ri^{-1} along the three lines. The fourth column shows the full time average profiles of the same quantities for the West (blue), East (red) and Separation (green) lines. Shaded regions show the 95% confidence intervals. The dotted line at 100 m marks the approximate boundary between the upper and lower layers

1.3.3 Tidal Flow Scenario

During the second half of the experiment the mean flow in the upper layer subsided such that flow was tidally dominated throughout the water column (Figure 1.2). The FCTD survey was conducted during this period.

Here we highlight three of the nine surveys conducted around the headland. The full set of surveys can be found in the Supporting Information. Note that the velocities

and Rossby number from passes 6-9 were also shown in Mackinnon et al. (2019). As they discussed, cyclonic and anti-cyclonic O(1 km) eddies were seen around the headland. Cyclonic eddies are shed during the westward phase of the tide, while anti-cyclonic eddies were shed during the eastward phase. However, the addition of a mean flow lead to asymmetries in the strength of the vorticity, with clockwise vortices being the most predominant (Mackinnon et al. 2019). Here, we expand on the discussion by including the earlier passes (passes 1-5) and estimates of the turbulent dissipation rate in our analysis. The velocities at the beginning of the record, shortly after neap tide, were small and vorticity was less coherent (e.g. Figure 1.3.3, panels 3A-E). Velocity magnitudes observed during the first 3 passes did not exceed 0.4 m s^{-1} and averaged 0.1 m s^{-1}. Over the course of the 5 days during which sampling took place, the velocities strengthened, with maximum velocities of 0.7 m s^{-1} by the 9th pass and averages of 0.2 m s^{-1}. With the increase in velocity the Rossby number (orange/purple coloured contour lines in Figure 1.3.3) also increased. Stronger, more coherent vortices were seen during the latter half of the record (e.g. Figure 1.3.3, panels 6A and 8D with $|Ro|$ of 42 and 70 respectively).

The depth structure of the velocity and vorticity was very rich with multiple layers of flow in different directions. The stronger vortices stretched up to 100 m in height. However, the depth range and height varied with time. The vortices were also seen to tilt with depth. For example, in the 8th pass the core of the anti-clockwise vortex tilted to the west with depth (Figure 1.3.3 panels 8A-E).

By eye, it appears that the highest values of the turbulent dissipation (blue-yellow filled contour in Figure 1.3.3) were seen where there was strong vorticity (e.g. panels 6A, 8C). The turbulent dissipation was generally lower away from the vortex and when there were no strong vortices. However, some patches of high turbulent dissipation were seen where there was little to no vorticity in the 50-100 m depth range (e.g. panels 3A and 6A).

Figure 1.4. (a) FCTD surveys for passes (columns) 3, 6 and 8 conducted from east to west. Depth averages over the ranges 50-100 m (A), 100-150 m (B), 150-200 m (C), 200- 250 m (D) and 250-300 m (E) are shown in each row. In each panel the turbulent dissipation rate (ϵ_χ (W kg^{-1})), estimated using microconductivity observations from the FCTD, is shown as filled contours. The Rossby number, $Ro = \frac{v_x - u_y}{f}$, is shown by coloured contour lines. Positive *Ro* (orange) indicates counter-clockwise rotation while negative *Ro* (purple) indicates clockwise rotation. The location of the F4 mooring is marked in panel D3 with the orange star. (b) shows the depth averaged velocity anomaly from the F4 mooring for the time period of the FCTD survey together with an M2 harmonic fit to the depth averaged velocity, shown in light grey. The duration of each radiator is shown by the black lines and labelled with the corresponding number of the radiator.

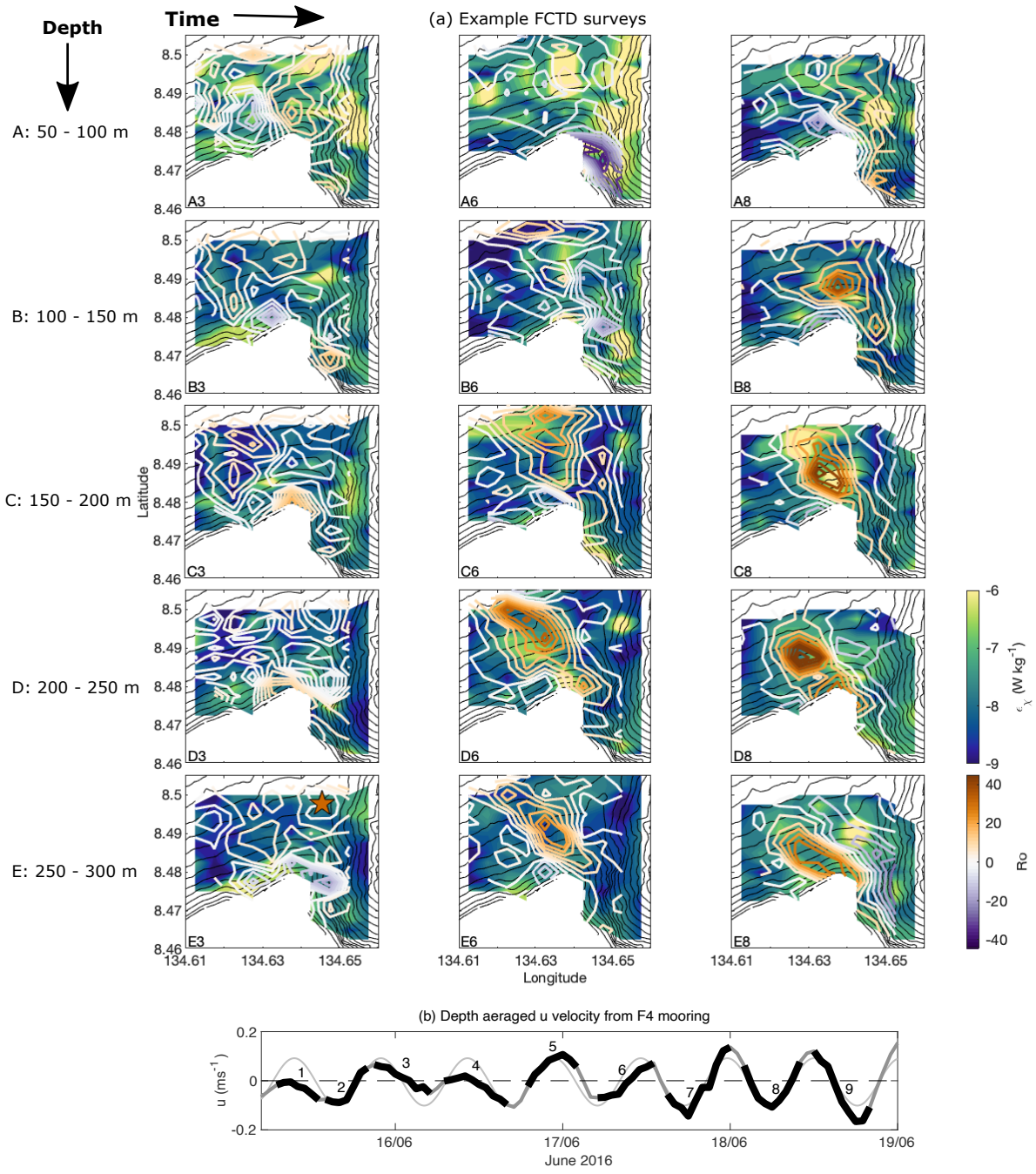
Depth
Time
(a) Example FCTD surveys
A: 50 - 100 m
B: 100 - 150 m
C: 150 - 200 m
D: 200 - 250 m
E: 250 - 300 m
A3
A6
A8
B3
B6
B8
C3
C6
C8
D3
D6
D8
E3
E6
E8
Latitude
Longitude
8.5
8.49
8.48
8.47
8.46
134.61
134.63
134.65
-6
-7
-8
-9
ϵ_χ (W kg^{-1})
40
20
0
-20
-40
Ro
(b) Depth aeraged u velocity from F4 mooring
u (ms^{-1})
0.2
0
-0.2
1
2
3
4
5
6
7
8
9
16/06
17/06
18/06
19/06
June 2016

1.4 Discussion

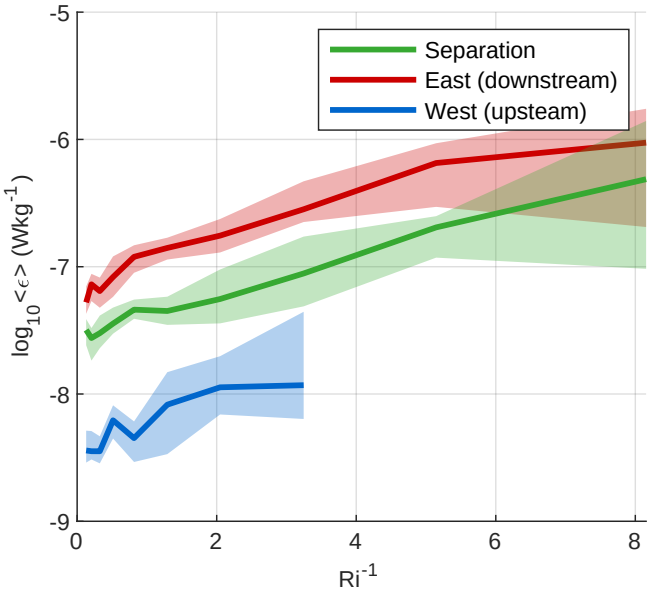

Figure 1.5. Dissipation rate of turbulent kinetic energy from MMP shear microstructure measurements (ϵ) as a function of inverse Richardson number for the West, Separation and East Lines above 100 m depth. Richardson number was binned evenly in log space and the median ϵ was calculated for each bin. Shaded regions show the 95% confidence interval on the median.

Our observations include a clear example of a geophysical wake. In the mean flow scenario observed, turbulent dissipation was enhanced by up to 3 orders of magnitude in the lee compared to upstream and up to a factor of 4 compared to the separation point (Figure 1.3). Turbulent dissipation rates up to 10^{-5} W kg^{-1} observed downstream by the MMP and close to wake eddies are comparable to the turbulent dissipation rates seen by Chang et al. (2013) at Green Island and by Hasegawa et al. (2004) at Aoga-Shima Island. Wijesekera et al. (2020) also observed similar levels of turbulence at Velasco Reef in December of 2016.

To investigate the mechanisms driving this enhanced dissipation and to identify which of our hypotheses (Table 1.1) are likely to be most important, we look at statistics

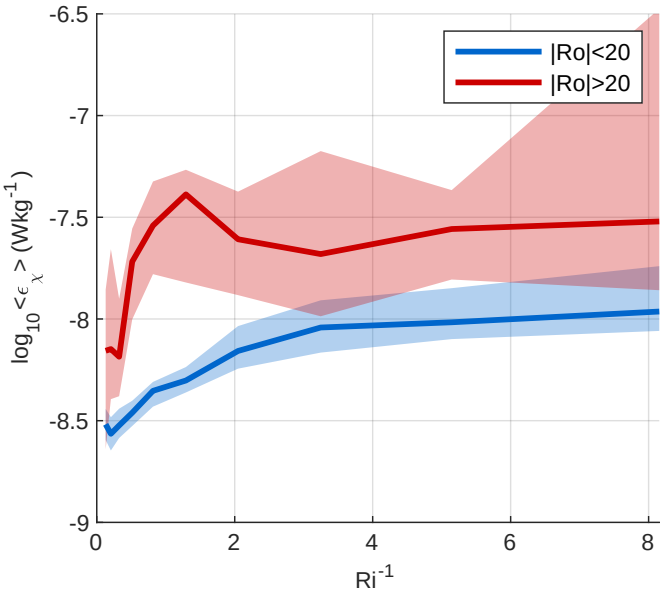

Figure 1.6. Dissipation rate of turbulent kinetic energy from FCTD microconductivity measurements (ϵ_χ) as a function of inverse Richardson number for low Rossby number ($|Ro| < 20$) and high Rossby number ($|Ro| > 20$) regions. Richardson number was binned evenly in log space and the median ϵ_χ was calculated for each bin. Shaded regions show the 95% confidence interval on the median.

of the inverse Richardson number and the Rossby number. First, we binned the turbulent dissipation observed in the top 100 m (the mean flow layer) from the MMP survey as a function of inverse Richardson number. The bins were designed to be equal in log space to account for more data at lower Ri_8^{-1}. The median value of ϵ was calculated and the error in the median was then estimated for each bin using bootstrapping. Figure 1.5 shows the binned median ϵ for the eastern, western and separation lines completed with the MMP. In agreement with the results in Figure 1.3, the largest values of the binned ϵ were seen on the eastern line, downstream of the mean flow. At all three of the lines, the turbulent dissipation increased as Ri_8^{-1} increased. The steepest increase occurred at low Ri_8^{-1}. High values of inverse Richardson number were not observed along the western line. At the eastern and separation lines, the rate of increase slowed above $Ri_8^{-1} = 4$ possibly since shear instabilities were already present and the increased

Richardson number did not lead to additional turbulent dissipation. The positive relationship between ϵ and Ri_8^{-1} seen at all three lines suggests that turbulence around the headland was generated by shear instabilities. However, turbulent dissipation at the lowest inverse Richardson numbers was elevated at the separation and eastern lines which suggests other generating mechanisms were also at work downstream and where the flow separated. We therefore investigate the dependence of the increased turbulent dissipation on the wake using the Rossby number.

Turbulent dissipation, ϵ_χ, from the FCTD was also binned using Ri_8^{-1} in the same way as for the MMP for all depth levels between 50 and 300 m. With the Rossby number information available from the FCTD sampling pattern, we were additionally able to split the data into weak and strong vorticity scenarios to investigate the relationship between the turbulence and the eddies observed in the lee of the headland (Figure 1.6). Turbulent dissipation and inverse Richardson number were positively correlated for both $|Ro| < 20$ and $|Ro| > 20$. The steepest increase in ϵ_χ was seen at low Ri_8^{-1}, as was also seen in the mean flow observations (Figure 1.5). The high Rossby number case was associated with higher turbulent dissipation than the low Rossby number case.

For the mean flow scenario, since we did not have extensive spatial coverage we are only able to say that turbulent dissipation was correlated with Ri_8^{-1} and was enhanced downstream of the headland. In the tidal flow scenario, we saw evidence of coherent vortex structures (Figure 1.3.3), consistent with an Re_{eff} in an eddy shedding regime (Mackinnon et al. 2019). Together with the result that ϵ was correlated with both Ro and Ri_8^{-1}, this suggests that we did not have a fully turbulent wake. We therefore discard Hypothesis I.

The instability criterion for CSI is dependent on the sign of the potential vorticity (Equation 1.1). If CSIs were a dominant mechanism for the generation of turbulence we would expect to see a relationship between the observed turbulent dissipation and the sign of the potential vorticity. We find that although dissipation is greater when $q < 0$,

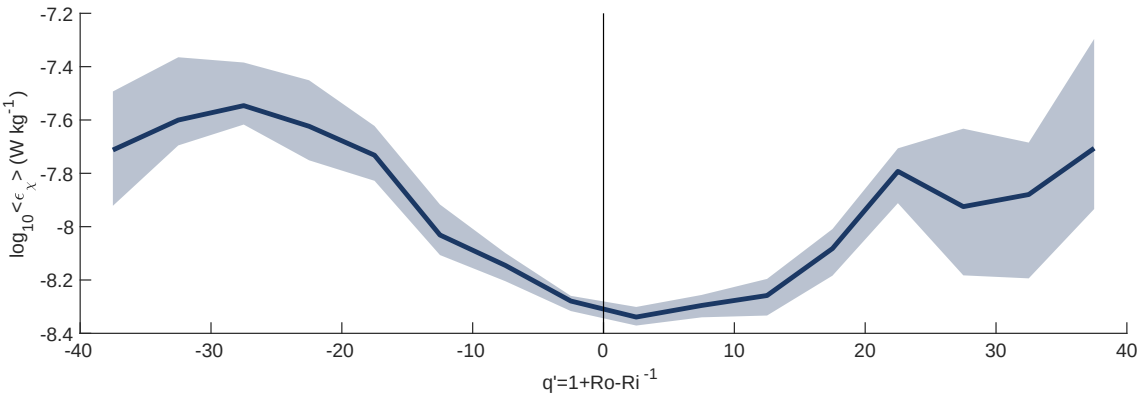

Figure 1.7. Median dissipation rate of turbulent kinetic energy from FCTD microconductivity measurements (ϵ_χ) as a function of the normalised potential vorticity $q' = N^2 fq = 1 + Ro - Ri_8^{-1}$. Shaded regions show the 95% confidence interval on the median.

it is enhanced for both positive and negative vorticity (Figure 1.7). We also note that the flow conditions here lead to a prevalence of positive vorticity eddies (Figure 1.3.3) (Mackinnon et al. 2019). Therefore, Hypothesis IV is unlikely to describe the processes relevant for the largest eddies, but CSIs may occur elsewhere around the headland.

Both tilted and non-tilted vortices were seen here (Figure 1.8). For a non-tilted vortex, such as was seen in Radiator 6, the strongest shear was seen above or below the vortex due to the limited vertical extent of the region of strong vorticity. In the case of Radiator 6, the top of the vortex was within the strongly stratification depth region between 100 and 150 m, therefore the highest values of Ri_8^{-1} were seen below the vortex. On the other hand, a vortex with a tilted core causes the shearing of flow along its entire depth; therefore, regions of high Ri_8^{-1} cover a larger vertical extent than for a non-tilted vortex. In both cases, the region of highest Ro can be offset from the region of Ri_8^{-1}. Accounting for the vertical offset of the two variables by depth-averaging demonstrates a positive correlation between Ro and Ri_8^{-1}, that would otherwise not be apparent (Figure 1.8 (b)). Dissipation values are enhanced in the depth range of the eddies for both the tilted and the non-tilted vortex. Therefore, we find that ϵ is correlated

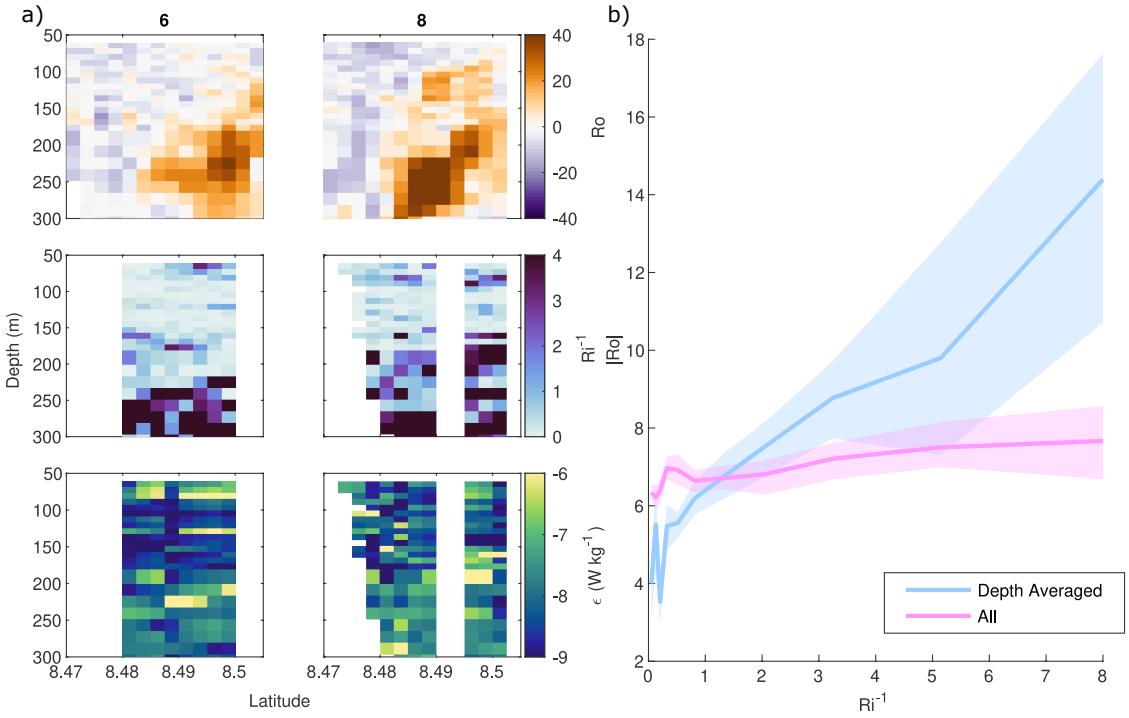

Figure 1.8. (a) Latitudinal sections at a longitude of 134.6275° of Ro (top) and Ri_8^{-1}(middle) and ϵ_χ through the CCW eddies seen in radiators 6 (left) and 8 (right). (b) $|Ro|$ binned by Ri_8^{-1} for all values (pink) and for depth averaged $|Ro|$ and Ri_8^{-1}(blue). Shaded regions show the 95% confidence interval on the mean within each bin

with both Ro and Ri_8^{-1} (Figure 1.6) and the eddies themselves generate regions that are unstable to shear instabilities.

If internal tides were the only mechanism of importance in this region (Hypothesis V), and breaking was driven by shear instabilities then we could expect a correlation between ϵ and Ri_8^{-1}, as we have observed. We would, however, not expect to see any relationship between ϵ and Ro. Other observations suggest that internal tide generation and breaking contribute to turbulent dissipation at the ridge (Voet et al. 2020). Additionally, our statistics are unable to capture other breaking mechanisms such as convective breaking. Therefore, while internal tides cannot be the only mechanism generating turbulence in this region we cannot discount their contribution. Shear driven breaking together with an independent process where ϵ is correlated with Ro would

give the results we observe. If the wake contained eddies at all scales, some of which were inherently turbulent then we would see a correlation between ϵ and Ro. Therefore, a combination of Hypothesis II and Hypothesis V would explain our observations.

As noted above, we observe that the eddies generate shear either due to tilting or due to their limited vertical extent. It is therefore possible that the observed positive correlation between $|Ro|$ and Ri_8^{-1} is caused by the eddies themselves. Since we do not disregard the importance of internal tide, we suggest that Hypothesis III together with Hypothesis V could also be the mechanisms driving increased dissipation in the wake.

1.5 Conclusions

This paper has presented observations of turbulence in the vicinity of Velasco Reef, Palau. The dissipation rate of turbulent kinetic energy (ϵ) was measured both directly, using shear probes on the Modular Microstructure Profiler (MMP), and indirectly from microconductivity measurements on the FastCTD (FCTD). The MMP data were collected along three lines, two of which where tidally resolving, around the northern end of Velasco Reef, Palau. The locations of the lines were chosen to provide observations upstream, downstream and at the separation point of the flow past the promontory. The FCTD survey was a radiator pattern that, although not tidally resolving, provided spatial information about processes in proximity to the reef. The superposition of tides and mean flow create time varying upstream conditions and thus a highly variable wake structure in both space and time. Two different regimes occurred during the deployments. The first was observed during the MMP survey. In this regime, eastward mean flow dominated over the tides in the top 100 m of the water column. Turbulent dissipation was found to be several orders of magnitude higher downstream of the headland, indicating wake turbulence. The second regime was seen during the FCTD survey when flow reversals occured at semi-diurnal frequencies due to the tides. We observed

vortices that were shed from the headland at tidal frequencies, particularly close to spring tide. The vortices varied in strength with depth, likely due to the complicated layered structure of the upstream flow. These vortices were again associated with turbulent dissipation of up to 10^{-5} W kg^{-1}, comparable to other estimates in oceanic wakes (Hasegawa et al. 2004; Chang et al. 2013; Wijesekera et al. 2020).

Analysis of the inverse Richardson number and Rossby number associated with the flow around the headland showed that turbulence was related to both shear and vorticity in the wake. We suggest that this relationship is due to the vortices themselves generating shear, supported by observations of enhanced ϵ in regions of shearing eddies. We note that the contribution to epsilon from breaking internal tides co-located with a turbulent wake can create similar correlations between ϵ, Ro and Ri_8^{-1}.

Complex flow-topography interactions such as those seen at Velasco Reef are likely to be common in many other parts of the coastal ocean. The methods used in this study could be extended to observational studies in other regions to better understand the relative importance of mechanisms such as vortex shear and centrifugal-symmetric instabilities in generating turbulence in oceanic wakes. Increased understanding of the prevalence of these different mechanisms will allow for improved parametrisations of wake processes in models with both physical and biological applications.

1.6 Acknowledgements

We thank Captain Murline, the crew of the R/V Revelle, our FLEAT colleagues and staff of the Coral Reef Research Foundation for their assistance in facilitating this experiment. This work would not have been possible without the hard work and talent of the engineers of the Multiscale Ocean Dynamics group at Scripps. We are grateful to Jonathan Nash and his team at OSU for providing the mooring used in this study. This work was supported by ONR Grants N00014-15-1-2264, N00014-15-1-2320,

N00014-15-1-2592, and N00014-16-1-3070.

Chapter 1, in full, is a reprint of the material as it appears in Journal of Geophysical Research: Oceans 2022. DOI:10.1029/2022JC018674. Wynne-Cattanach, Bethan L.; Alford, Matthew H., MacKinnon, Jennifer A.,Voet, Gunnar. The dissertation author was the primary investigator and author of this paper.

Chapter 2

Observational evidence of diapycnal upwelling within a sloping submarine canyon

Small-scale turbulent mixing drives the upwelling of deep water masses in the abyssal ocean as part of the global overturning circulation (Wunsch and Ferrari 2004). However, the processes leading to mixing and the pathways through which this upwelling occurs remain insufficiently understood. Recent observational and theoretical work (Ledwell et al. 2000; St. Laurent et al. 2001; Ferrari et al. 2016; De Lavergne, Madec, Le Sommer, Nurser, and Naveira Garabato 2016) suggests that deep water upwelling may be focused along the ocean's sloping seafloor; however, evidence has, to date, been indirect. Here, we present observations from a near-bottom dye release within a canyon on the North Atlantic continental slope. We observe upwelling across density surfaces at a rate of $O(100)$ m day^{-1} over three days, ~10,000 times higher than the global average value required to account for ~30 Sv of net upwelling globally (Munk 1966). The vigorous upwelling is coupled with adiabatic exchange of near-boundary and interior fluid. These results provide the first direct evidence of strong, bottom-focused diapycnal upwelling in the deep ocean, supporting previous suggestions that mixing at topographic features, such as canyons, leads to globally-significant upwelling (St. Laurent et al. 2001; Kunze et al. 2012; Thurnherr et al. 2020; Drake et al. 2022).

2.1 Introduction

The oceanic overturning circulation plays an important role in regulating the global climate by redistributing tracers such as heat, carbon and nutrients throughout the oceans. Transport across density surfaces (isopycnals) by turbulent mixing has long been recognised as a key part of the circulation. Beginning with Munk (1966), it has been argued that cross-isopycnal upwelling of deep water is primarily driven by the widespread mixing caused by breaking internal waves in waters deeper than ~2000 m (De Lavergne, Madec, Le Sommer, Nurser, and Naveira Garabato 2016; Lumpkin and Speer 2007; Talley 2013). The wind and the tides generate internal wave energy at a rate of ~1 TW each, sufficient to mix abyssal waters across the stable deep stratification to the ocean's ventilated mid-depth and upper layers (Egbert and Ray 2000). Observations in search of the necessary mixing found that turbulent diffusivity in the ocean interior was at least an order of magnitude smaller than the average value needed to close the abyssal buoyancy budget, implying the existence of regions of intense mixing to compensate for the low observed interior mixing and thus maintain the circulation (Wunsch and Ferrari 2004). More recent measurements have shown that mixing due to breaking internal waves typically intensifies towards the seafloor, particularly around rough topographic features (Polzin et al. 1997; Rudnick et al. 2003; van Haren and Gostiaux 2012; Waterhouse et al. 2014). In the ocean interior, a one-dimensional mixing profile integrating these observations (which yields an increase in mixing with depth) implies a divergent turbulent buoyancy flux leading to downwelling (Ledwell et al. 2000; St. Laurent et al. 2001). Thus, internal wave breaking in the interior might not produce the required upwelling as previously thought, leaving the question of how deep waters return to the surface.

To resolve this apparent paradox, it has been hypothesised that upwelling may be confined to near-bottom regions within which the buoyancy flux perpendicular to the

boundary must decrease to zero due to the requirement of no flux through the boundary itself (Ferrari et al. 2016; De Lavergne, Madec, Le Sommer, Nurser, and Naveira Garabato 2016; McDougall and Ferrari 2017). The convergent turbulent buoyancy flux leads to upwelling near the boundary. While the no flux condition assumes no geothermal heat flux through the seafloor, including geothermal heat flux reinforces upwelling at the boundary by warming deep waters from below (De Lavergne, Madec, Le Sommer, Nurser, and Naveira Garabato 2016; Mashayek et al. 2013).

Microstructure measurements at a Southern Ocean sill (Naveira Garabato et al. 2019; Spingys et al. 2021) and within a Mid-Atlantic Ridge fracture zone canyon (St. Laurent et al. 2001; Thurnherr et al. 2020) showed enhancement of turbulent dissipation with depth which suggested densification away from the boundary, but lightening along the steeply sloping topography. Numerical simulations of passive tracer releases showed that the tracer upwelled rapidly as it was advected into the near-boundary region (Mashayek et al. 2017; Drake et al. 2022). Together, these results suggest that boundaries may play an important role in upwelling and reinvigorating fundamental debates on the nature of boundary mixing (Armi 1978; Polzin and McDougall 2022). However, all evidence has, to date, been inferred indirectly from microstructure observations or numerical simulations and based on a range of debatable assumptions.

The near-bottom upwelling region needs to be reconciled with previous definitions of the boundary layer. A frictional bottom boundary layer due to a uniform shear flow above a flat surface is well-mixed and homogeneous. In the context of mixing driven by geostrophic flows (Ruan and Callies 2020), the boundary layer can be defined by the Ekman layer. One-dimensional models of steady flow on a planar slope give rise to a weakly stratified near-boundary region which has been labelled as the bottom boundary layer (Ferrari et al. 2016; McDougall and Ferrari 2017; Garrett 1979). These well-mixed regions are rarely observed over sloping bottoms, and so recent work has instead referred to the bottom boundary layer as the region where the

diapycnal transport is upwards (Holmes and McDougall 2020). However, above sloping topography where three-dimensional processes such as re-stratification, internal wave breaking and boundary-interior exchange play a role, the physics that gives rise to a convergent buoyancy flux near the bottom becomes murky. Because of the lack of a clear definition of this near-bottom region and because it is not well-mixed owing to the rapid exchange with the interior, we will refrain from referring to it as a bottom-boundary layer.

In this study, we present results from a dye release conducted as part of the Boundary Layer Turbulence and Abyssal Recipes (BLT Recipes) experiment. A major goal of the experiment was to provide observational confirmation of vigorous near-boundary abyssal upwelling and to explain the physics driving it. The experiment site chosen was the Rockall Trough (Figure 2.1), given its relatively flat, deep interior and steep sides. These characteristics enable a clear distinction between interior and boundary processes, which is essential for determining the driving forces behind the transformation of deep water. In particular, the study was conducted in a narrow, slope-incising canyon on the eastern side of the Rockall Trough. The canyon is 9 km wide at the mouth and 32 km long from the 2900 m isobath to the tip of the eastern branch of the canyon at the 1200 m isobath. On average, the canyon walls rise 400 m above the thalweg. The canyon splits into a southward and south-eastward branch around 54 14.0′ N, 11° 57.1′ W. Our measurements focused on the south-eastward branch of the canyon.

The BLT canyon, like many other canyons (Kunze et al. 2012; van Haren et al. 2022; Alberty et al. 2017), exhibits vigorous twice-a-day and once-a-day up- and down-canyon flow (Figure 2.2, Figure B.1d) associated with internal tides. Internal tides are generated when the depth-independent or barotropic tide flows over seafloor features. Observed kinetic energy is $2-3$ times larger than the barotropic tide and rises and falls according to the barotropic spring-neap cycle (Figure B.2a), indicating that flow within the canyon

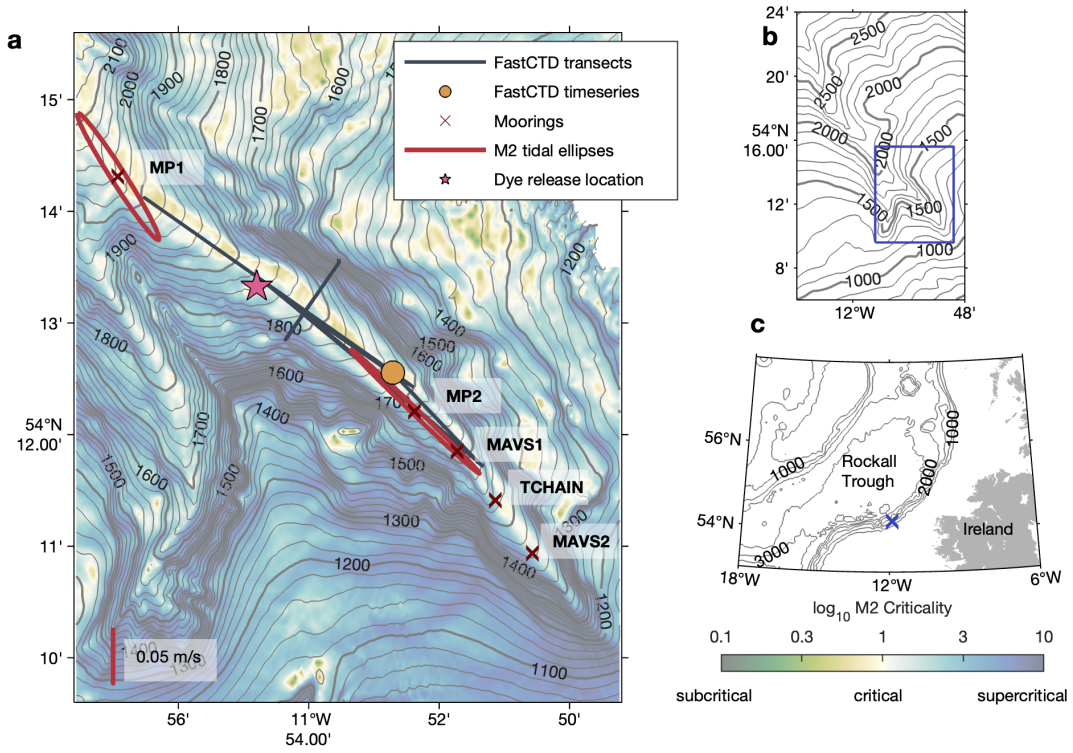

Figure 2.1. (a) Canyon bathymetry in the vicinity of the measurements used for this study was measured using a shipboard multi-beam during the BLT Recipes experiment. Thin contours are every 20 m and thick contours are every 100 m. Locations of the FastCTD transects (black lines), 12-hour time-series station (orange circle), moorings (MP1, MP2, MAVS1, TCHAIN and MAVS2) and dye release are shown. M2 tidal ellipses for the MP1 and MP2 moorings estimated from the average velocity within 100 m of the seafloor are shown with a scale bar of 0.05 m s^{-1}. Shading shows the logarithm of slope criticality to the M2 internal tide given the time-mean stratification from shipboard CTD stations during the 5-week-long experiment (not shown). (b) Bathymetry of the full canyon based on global bathymetry products. Thin contours are every 100 m, and thick contours are every 500 m. The blue box marks the region shown in panel (a). (c) Bathymetry of the Rockall Trough based on global bathymetry products, contours every 1000 m. The land is coloured in grey. The location of the canyon is marked by the blue cross.

is due to internal tides that are generated locally as opposed to propagating in from elsewhere. These motions strongly advect the temperature structure both laterally and vertically. The vertical displacements of 200 m are clear in Figure B.1. Because the up-canyon flow is sheared, differential advection reduces stratification (Figure B.1b)

and eventually causes warm water to be swept below cold water each cycle following peak up-canyon flow (Figure B.1, zoom panel), causing strong turbulence (Figure B.1b). This mechanism, known as convective instability, is demonstrated more quantitatively to be acting as the internal tide breaking mechanism in our canyon (A.C.N.G., C.P.S., M.H.A., Bieto Fernández-Castro, K.P., G.V., B.L.W.C., N.C., Alexander Forryan, H.F.D., X.R., H.M., M.-J.M., Eleanor E. Frajka-Williams, R.F. (in prep.)) and has been seen atop numerous other continental slopes (van Haren et al. 2022; Nash et al. 2007; Alford et al. 2011).

The tendency for internal tides to break when interacting with topography depends on the ratio of the topographic slope (α) to the propagation angle

$$s = \sqrt{\frac{\omega^2 - f^2}{N^2 - \omega^2}} \tag{2.1}$$

of the internal wave (the criticality) (LeBlond and Mysak 1981), where ω is the internal wave frequency, f is the local inertial frequency and N^2 is the buoyancy frequency. To estimate criticality, we use the time-mean buoyancy frequency estimated from shipboard CTD casts collected within and around the canyon during the 5 weeks of the BLT Recipes experiment. The canyon thalweg, with an average slope of 4°, has a similar slope to the internal semi-diurnal (M2) tides ($\frac{\alpha}{s} \approx 1$), implying local generation and critical reflection of the internal tide within the canyon. The canyon side walls are supercritical ($\frac{\alpha}{s} > 1$; blue shading in Figure 2.1), which tends to lead to reflection and scattering of incident waves.

The time-mean flow, at timescales longer than the tides, is up-canyon (velocity profiles in Figure 2.4 and time-series in Figure B.3). Low-pass filtered isotherm displacements (Figure B.4) correspond to adiabatic velocities smaller than the vertical component of the up-canyon flow (Figure B.3), suggesting that the dominant balance within the canyon is between the upwelling flow and flow across isopycnals (see Methods). In this

regard the system resembles a miniature version of the Brazil Basin system described in St. Laurent et al. (2001) and Drake et al. (2022). We measured the diapycnal flow directly for the first time with the dye release described below.

2.2 Diapycnal upwelling measured by dye

In the BLT experiment, fluorescein dye was released near the seafloor in the centre of the canyon to measure the diapycnal transformation of water parcels. This experiment is distinct from previous dye releases due to the depth and deep-ocean environment (Houghton and Ho 2001; Ledwell et al. 2004; Wain and Rehmann 2010; Clark et al. 2014). Previously, deep water mass transformation has been observed using long-term chemical tracer experiments, such as those performed by Ledwell et al. (2000) and Ledwell et al. (2011) where the tracer was released at least 500 m from the sea floor. Measuring chemical tracers requires water samples, the collection of which is an inherently slow process with low spatial resolution. A fluorescent dye, however, can be measured continuously with a fluorometer, allowing for higher spatial and temporal resolution and facilitating direct observations of the effect of turbulent mixing over short timescales. Dye becomes undetectable much faster than a chemical tracer owing to the dye's much higher detection threshold ($\sim 10^{-3}$ versus $\sim 10^{-9}$ parts per billion), such that the duration of the experiment is on the order of days rather than months. Chemical tracers average together the impacts of turbulence over much longer time scales and greater distances from the bottom than a dye. The rapid changing of the shape and size of the dye patch makes estimating the diapycnal diffusivity experienced by the dye more difficult than for a long-term tracer. Instead, we can observe the diapycnal transformation of the dye close to the topography, averaged over the duration of the experiment which may include upwelling and downwelling components depending on its extent.

The dye was released in 1870 m of water, approximately 10 m above the canyon floor and at a conservative temperature of 3.53 °C. The rapid profiling "Fast CTD" (FCTD; details in Methods) carried a fluorometer, enabling high spatial and temporal resolution profiles of dye down to 2200 m depth. Also onboard the FCTD was a micro-conductivity probe that measured the dissipation rate of temperature variance (χ), a measure of turbulent mixing. We focus on the transformation of the dye within the first 3 days after release.

To quantify the rate of flow across isopycnals we track the evolution of the dye in density space using the dye weighted average (see Methods). We use the density variable of potential density anomaly, $\sigma_\theta = \rho_\theta - 1000$ kg m^{-3}, referenced to a pressure of 1500 db. While seawater density depends on both temperature and salinity, density is approximately linear in temperature in this region (H.v.H., G.V., M.H.A., Bieto Fernández-Castro, A.C.N.G, B.L.W.C., H.M., M.-J.M. (submitted)), permitting us to use temperature and density interchangeably to characterise upwelling. By focusing on the diapycnal transformation we avoid having to account for how the dye moves up and down due to the tides in physical space.

The first moment of potential density anomaly, $\overline{\sigma_\theta}$, estimated using the tracer-weighted average, represents the centre of mass of the dye in density space. By estimating how the density of dyed waters decreased with time we can infer an upwelling rate across isopycnals (Figure B.7). The first observation of the dye was made two hours after release (Figure 2.3a). The dye cloud was still very concentrated at this time. The centre of mass was at a potential density anomaly of $\sigma_\theta = 34.660$ kg m^{-3}. Little mixing with lighter waters occurred since the dye release at $\sigma_\theta = 34.661$ kg m^{-3} (Figure 2.3d). The isotherms were stretched vertically, indicative of a large overturning event due to internal wave breaking on the slope (as seen in the moored time series (Figure B.1)). Vigorous turbulent mixing was seen along the upper edge of the bore, over 100 m above the seafloor (blue contour; Figure 2.3a). The dye likely mixed strongly across

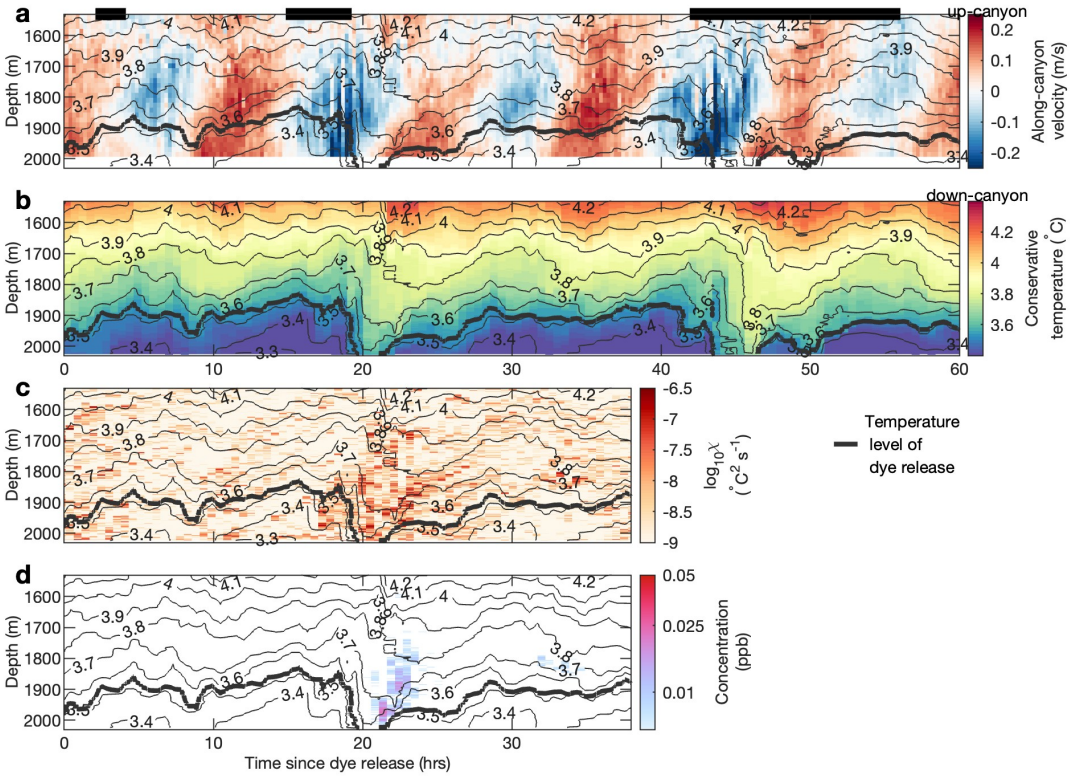

Figure 2.2. (a) Along-canyon velocity (up-canyon is positive), (b) conservative temperature, (c) dissipation rate of temperature variance on a logarithmic scale and (d) dye concentration on a logarithmic scale in parts per billion from MP1. The threshold for dye concentration detection for the fluorometer onboard the MP1 is 0.006 ppb. Thin black contours show every 0.1 °C. The release isotherm of 3.53 °C in conservative temperature is shown with the thick black contour. Thick black lines along the top of panel (a) indicate times of FCTD transects shown in Figure 2.3. The battery for dissipation and fluorometer measurements stopped around 38 hours after the dye release.

this interface. Fifteen hours after release, the dye was observed as the ship travelled down the canyon (Figure 2.3b). The dye had lightened since the up-canyon transect, and the centre of mass was at $\sigma_\theta = 34.632$ kg m^{-3}. Over the subsequent observations, the dye became more diffuse and spread both vertically and horizontally, as can be seen during the FCTD time series completed at the end of the survey (Figure 2.3c). Using the rate of change of the observed dye-weighted density and the averaged vertical density gradient, the diapycnal upwelling rate of the dye (w_{dye}) was estimated using four different methods with values ranging from 51 to 325 m day^{-1} (Table 2.1 and Methods). In spite of the large spread, all the methods indicate significant upwelling of O(100 m day^{-1}) near the bottom over the 3 days of the experiment.

Velocity measurements from both the MP1 (1-week record) and MP2 (3-month record) moorings show that the record-mean along-canyon flow was up-canyon within 500 m of the seafloor and density decreased towards the head of the canyon (Figure 2.4). The momentum balance driving the up-canyon flow is currently under investigation. Candidate driving forces include i) large-scale pressure gradients set by the mesoscale and/or mean circulation fields and ii) convergent radiation stresses (Marques 2021). Regardless, as described above and in the Methods, in order to maintain this along-canyon flow down the density gradient on longer than tidal timescales (Figure B.3), there must be mixing across isopycnals or else adiabatic upwelling would cause isotherms to rise over long timescales, which is not observed (Figure B.4) (Thurnherr et al. 2020; Ruan and Callies 2020; Peterson and Callies 2022). The along-canyon velocities from the week-long MP1 record during the experiment are then equivalent to vertical upwelling velocities of $50-100$ m day^{-1}, consistent with the dye result (Figure B.3). By contrast, estimates of the vertical adiabatic flow (which if persistently upward could obviate the need for diapycnal mixing as noted above), is significantly smaller, with both positive and negative values. While these estimates were not exactly at the same time and location as the dye release, they do strongly suggest that the observed dye warming is

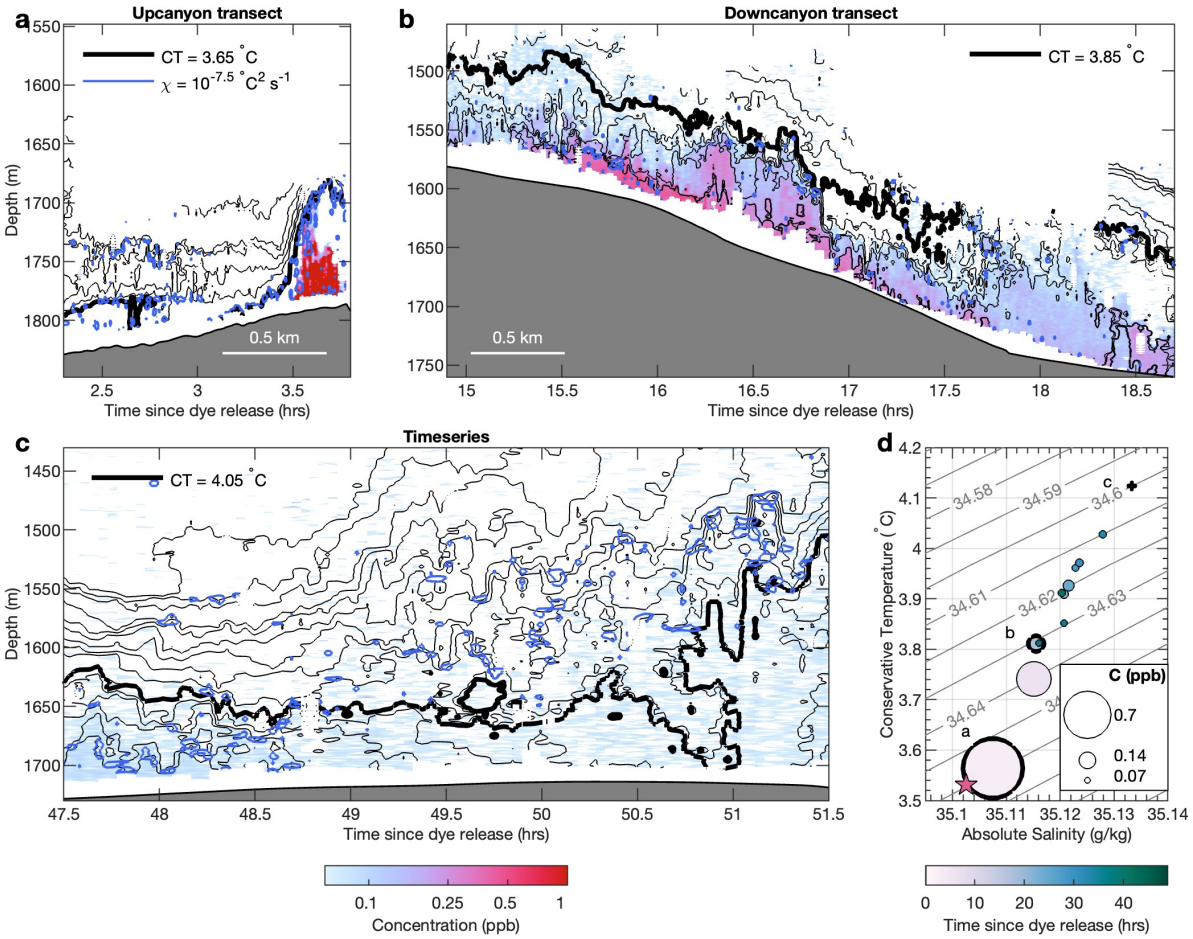

Figure 2.3. Dye concentration as measured during transects at (a) 2.5 hours, (b) 15 hours and (c) 47.5 hours after release. Dye concentration is shown on a logarithmic scale in parts per billion (ppb) in colour, isotherms whose mean depths are separated by 10 m are shown with thin black contours and the $\chi = 1 \times 10^{-7.5}$ °C^{2}s^{-1} contour is shown in blue on each panel denoting regions of enhanced turbulent mixing. Thick black contours indicate reference conservative temperatures 3.65 °C, 3.85 °C and 4.05 °C for panels (a), (b) and (c) respectively. The threshold of dye concentration detection for the fluorometer onboard the FCTD is 0.06 ppb. Scale bars in panels (a) and (b) denote an estimate of the horizontal length of the transects. Panel (d) shows a temperature-salinity diagram of the centre of mass for each transect. Scatter points are coloured by time since the dye release in hours and the size of the data point indicates the average concentration during the transect. Scatters with thick outlines are labelled a, b and c, and correspond to the examples shown in panels (a), (b) and (c). The temperature and salinity at which the dye was released are marked with the pink star. Grey contours show lines of constant potential density anomaly in kg m^{-3}. See Figure B.5 for all transects and Figure B.6 for the full temperature-salinity distribution of each transect.

in fact interpretable as a diapycnal velocity.

Assuming the turbulent buoyancy flux to be bottom enhanced above a sloping bottom boundary, Ferrari et al. (2016) predict downwelling atop a thin upwelling region, as discussed above. Our dye results reflect the time- and depth-integrated effects of advection and diffusion on the initial patch; hence, the rate of change of the dye-weighted density can be related to the net effects of all upwelling and downwelling processes occurring within the extent of the dye patch from release to sampling (Ruan and Ferrari 2021). Given the patch's location within O(100 m) from the seafloor during the short period over which we could observe it, our finding of strong net upwelling is consistent with the theoretical predictions (Drake et al. 2022; Holmes et al. 2019). It is conceivable that our estimate of increased dye-weighted density (Figure B.7) at later times could be indicative of net downwelling as the patch occupies more volume above the region of convective instability where upwelling is seen, but our error bars are too great to be sure. The dye-based estimate of the upwelling averaged over all transects is then a lower bound on the magnitude of the local near-bottom upwelling rate.

2.3 Exchange with the interior

We observed a patch of the dye extending away from the boundary into the ocean interior, consistent with past inferences(Kunze et al. 2012) and numerical modelling(Winters 2015). The observation is significant because it demonstrates rapid exchange of fluid with the interior as the mechanism for re-stratifying the near-bottom region and provides direct evidence that one-dimensional treatments of the boundary are not sufficient.

The MP1 mooring was located 3 km down-canyon of the release site during the dye experiment. The dye reached the mooring twice, once 20 hours after release and once 32 hours after release (Figure 2.2). Importantly, the dye was detached from

the seafloor, having formed a tongue of dye extending into the interior. The FCTD survey of the dye 20 hours after release (Figure 2.4) captured the up-canyon edge of the dye. Dye concentrations were much lower at the mooring than at the FCTD location, suggesting that only the edge of the patch reached the mooring location. These two sets of measurements suggest that the patch size 20 hours after release was at least 4 km in length (the fluorometer on the mooring was 10 times more sensitive than the one on the FCTD (see methods), therefore, additional weakly concentrated dye further up the canyon may have gone undetected by the FCTD). In both the FCTD and mooring record the dye was colder than the 3.85 °C isotherm. In the mooring record, the dye remained warmer than the release isotherm, suggesting that the dye had not downwelled since its initial release. This direct evidence of the export of mixed fluid from the boundary underscores the need for a four-dimensional understanding of the tidal processes responsible for the turbulence. This view differs strongly from the one-dimensional paradigm espoused by Garrett (2001) and supports previous observations (Kunze et al. 2012; van Haren and Gostiaux 2012) and subsequent numerical simulations of near-boundary flow (Winters 2015) that suggest a vigorous exchange of mixed fluid with the interior, possibly driven by a convergent near-boundary flow (Kunze et al. 2012).

2.4 Summary

This work provides direct evidence of diapycnal upwelling along a sloping canyon in the deep ocean. Upwelling velocities of $O(100\text{ m day}^{-1})$ demonstrate that processes at steeply sloping topography led to rapid upwelling of deep water to lighter density classes. Diapycnal upwelling was coupled with adiabatic advection that transported dye away from the boundary along isopycnals. While observational limitations in this study lead to uncertainty in the dye-inferred upwelling experienced by the dye, the similarity between independent estimates of dye-based upwelling and

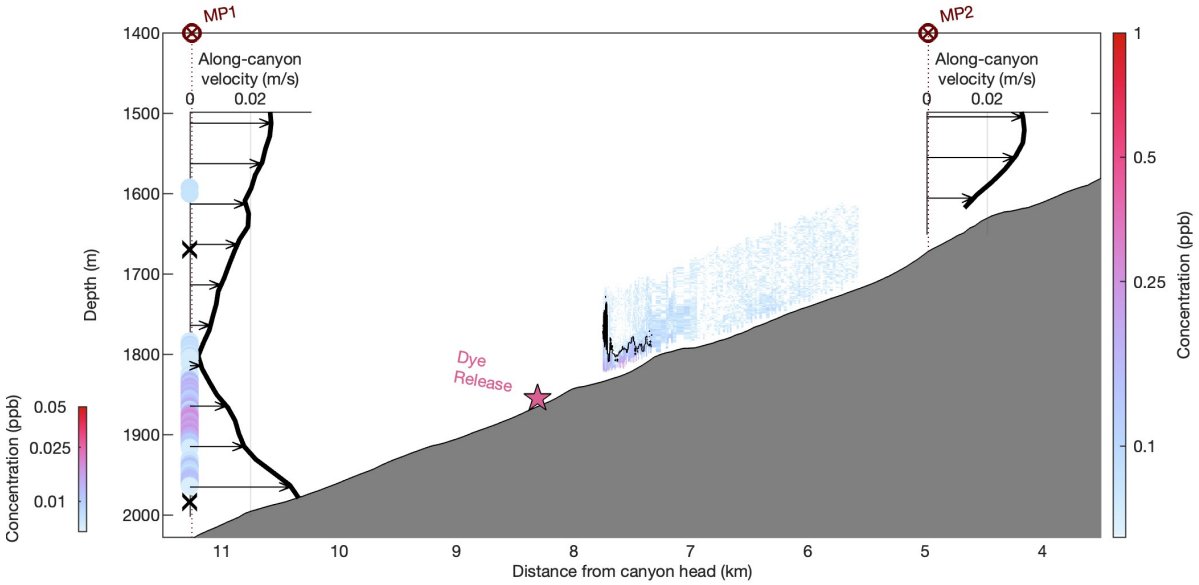

Figure 2.4. Inset axes show time mean profiles of along-canyon velocity at MP1 (located at 11.3 km along the canyon, averaged over the full 1-week record) and MP2 (located at 4.8 km along the canyon, averaged over the full 3-month record. MP2 was deployed after MP1 was taken out of the water). Dye concentration from an example transect 20 hours after the dye release along the canyon axis is shown between 5.5 and 8 km, with the highest concentrations shown with dark pink colours (see Figure B.5d for more detail). The 3.85°C isotherm is contoured in black. Coloured dots show dye concentration measured using the fluorometer on the MP1 mooring also at 20 hours after release. Colour scales for the dye transect and moored profile dye concentrations are different and the detection threshold is 0.06 ppb for the FCTD measurements and 0.006 ppb for the MP1 measurement. Depths of the 3.85 °C and 3.53 °C isotherms 20 hours after release are marked with black crosses on the MP1 profile.

diapycnal upwelling inferred from the measured along-canyon flow is encouraging.

Previous direct estimates of water mass transformation in the deep ocean have come from chemical tracer releases which focused on interior transformation and have much larger spatial and temporal averaging scales than this dye release and average over regions of near-boundary upwelling and above-boundary downwelling, as opposed to our more focused observations that more strongly weight near-boundary upwelling (Ledwell et al. 2000; Ledwell et al. 2011). These chemical tracer releases measured net downwelling, although Ledwell et al. (2000) noted that some of the tracer may have moved upwards along the seafloor.

Previous estimates of upwelling near the bottom were smaller in magnitude but were observed over much larger spatial and temporal scales than our experiment. Munk (1966) used the formation rate of Antarctic Bottom Water to estimate the average upwelling value required to maintain the global deep-ocean density stratification, obtaining a value of 1×10^{-2} m day^{-1}. In a fracture-zone canyon of the Mid-Atlantic Ridge, using multi-year observations on scales up to ~1000 km(Thurnherr et al. 2020), the mean upwelling velocity inferred from along-canyon velocity was 1.7 m day^{-1}. The magnitude of the up-canyon velocity was similar to that seen here; however, the much shallower bathymetric slope in the mid-Atlantic ridge case led to a relatively smaller upwelling velocity. Diapycnal upwelling in the Mid-Atlantic Ridge canyon has been determined to be controlled by the shape of the topography (hypsometry) (Thurnherr et al. 2020; Polzin and McDougall 2022). That is, the decrease in volume with depth as the canyon narrows leads to a decrease in the area available for mixing. The area integrated buoyancy flux decreases with depth, producing an upwards diapycnal velocity (Drake et al. 2022). In Monterrey Canyon, estimates of the net upwelling within the canyon using microstructure turbulence observations were also up to 3 orders of magnitude smaller than our observations and ranged from 0.2 to 1 m day^{-1} near the bottom due to the hypsometry Kunze et al. 2012. Our observations provide the

first direct estimate of the upwelling occurring at a bottom boundary. However, more observational experiments in various physical environments are necessary to reach an accurate estimate of the near-boundary's contribution to net global upwelling.

Our results provide support for previous theoretical studies which propose that near-boundary mixing is important for deep-ocean upwelling (Ferrari et al. 2016; De Lavergne, Madec, Le Sommer, Nurser, and Naveira Garabato 2016; McDougall and Ferrari 2017; Drake et al. 2020). Specifically, our results provide direct evidence in support of these studies' key prediction: to overcome the substantial interior ocean downwelling implied by bottom-enhanced mixing, the net global upwelling of ~30 Sv requires the existence of much more rapid upwelling near the sloping seafloor. An important limitation of these previous studies is that they focused on large-scale water mass transformations due to parameterised mixing, primarily due to tides; by contrast, here we directly observe these tidally modulated water mass transformation processes.

Complementary observations from the FCTD and long-term moorings during our experiment found that periods of intense mixing and upwelling were associated with convective breaking of the internal tide within the canyon (A.C.N.G. et al. (in prep.), H.v.H. et al. (submitted.)). Similar convective mixing has been observed on sloping boundaries elsewhere, within canyons (van Haren et al. 2022), on continental shelves and slopes (Nash et al. 2007; Alford et al. 2011; Moum et al. 2004; Aucan et al. 2006), and in lakes (Lorke et al. 2005), suggesting that this process may be of broad importance.

Our work suggests that acknowledgement of the time-variable, three-dimensional nature of near-boundary mixing processes may be essential to the adequate representation and understanding of near-bottom upwelling physics. Based on our observations and the widespread distribution of submarine canyons across the globe (Harris and Whiteway 2011), previous global scalings based on weaker upwelling velocities may be under-estimates (Kunze et al. 2012; Thurnherr et al. 2020; Cimoli et al. 2023). Upwelling within these canyons may play an even more significant role in the overturning of deep

water than previously thought.

2.5 Methods

2.5.1 BLT Recipes Experiment

The data presented here were collected during expedition DY132 of *RRS Discovery* (Naveira Garabato 2021) between June 19, 2021 and July 29, 2021, supported by the NERC and NSF-funded Boundary Layer Turbulence and Abyssal Recipes project. The experiment consisted of a dye release together with surveys and moorings measuring hydrographic data, velocity, and shear and temperature microstructure.

Dye release

A fluorescent dye (fluorescein $C_{20}H_{10}O_5Na_2$) was used for this experiment. The mixture used for the release consisted of 64 L of isopropyl, 6 L of seawater and 149 L of 40% fluorescein liquid. The mixture was chosen to be denser than the local water at the desired depth to ensure that it was released properly and did not rise without mixing. The dye release system (InkBot; University of Exeter) comprises a 219 L drum equipped with a Seabird SBE 911plus CTD, an AQUAtracka III fluorometer (Chelsea Technologies Group), an altimeter, and an OCEANO 2500S Universal acoustic release. For deployment, the InkBot was attached to the CTD sea cable and lowered to 10 m above the bottom using the ship winch. Once in position, the drum was emptied by simultaneously flipping the drum and opening the drum lid using the acoustic release. The drum was upside down for 15 minutes, while readings from the onboard CTD enabled the winch operator to ensure that the InkBot remained at the release temperature. The dye release began at 03:01 am on July 1, 2021. The BLT dye release is novel in its depth and deep-ocean environment, where common dye sampling techniques like aerial multi-spectral imagery could not be used. Instead, we performed rapid-repeat fluorometer measurements using the Fast CTD and operated the ship in a pattern that

dynamically followed the dye.

Fast CTD

The Fast CTD (FCTD) system (Klymak et al. 2008) is a tethered profiler with a Seabird SBE49 CTD, a dual needle micro-conductivity probe (built in-house at Scripps Institution of Oceanography by the Multiscale Ocean Dynamics group) and, for this experiment, a Turner C-FLUOR fluorometer and an altimeter. The instrument was raised and lowered with a direct drive electric winch at vertical speeds of approximately $3\,\mathrm{m\,s^{-1}}$ while the ship was steaming at a speed of 0.5–1 knot. Data from both up and down-casts were used. The goal of the FCTD survey was to sample the dye release as many times as possible before dye concentrations became too low to be detected. Transects were focused along the canyon axis to transit from one end of the dye patch to the other before turning around and repeating. Additionally, two cross-canyon transects and a 12-hour time-series station were completed to better understand the full extent of the dye patch. During a transect, the FCTD profiled over ~100 m vertical range and to within < 10 m of the seafloor. Data from the FCTD were monitored and used interactively to guide the survey.

The micro-conductivity probe was used to estimate the dissipation rate of temperature variance (χ). Conductivity gradients can be used since temperature dominates the conductivity variance (Alford and Pinkel 2000b).

MP1 and MP2 Moorings

The MP1 mooring was deployed on the canyon axis at 2028-m water depth at 54° 14.312′ N, 11° 56.923′ W. The mooring was 600 m tall and consisted of a downward looking RDI Longranger 75 kHz Acoustic Doppler Current Profiler (ADCP) mounted in the top float and a McLane Moored Profiler outfitted with a Seabird SBE52 CTD, a Falmouth Scientific Inc acoustic current meter, and an Epsilometer turbulence package

(Multiscale Ocean Dynamics group, Scripps Institution of Oceanography) (Le Boyer et al. 2021) to measure χ from temperature gradients, and a Turner C-FLUOR fluorometer. The profiler was deployed on June 28, 2021, and profiled continuously for 7 days, collecting one profile every 30 minutes. The mooring was redeployed (as MP2) on July 7, 2021, without the fluorometer and Epsilometer at 54° 10.938′ N, 11° 50.572′ W at a depth of 1676 m. This deployment lasted until October 6, 2021.

MAVS1, TCHAIN and MAVS2 Moorings

The MAVS1 and MAVS2 moorings were deployed for 3 months from July 6, 2021 - October 7, 2021. The MAVS moorings were each 300 m tall and consisted of 8 Modular Acoustic Velocity Sensors (MAVS; Woods Hole Oceanographic Institute), 80 RBR Solo or Seabird SBE56 thermistors, a Seabird SBE37 CTD and an RDI Longranger 75 kHz ADCP mounted on the top float. MAVS1 was deployed at 54° 11.849′ N, 11° 51.719′ W at 1612 m depth and MAVS2 was deployed at 54° 10.938′ N, 11° 50.572′ W at 1466 m depth. The TCHAIN mooring (Hans van Haren, Royal Netherlands Institute for Sea Research), deployed at 54° 11.413′ N, 11° 51.137′ W at 1529 m, consisted of a 150 m thermistor chain with 102 pre-attached thermistors and a 75 kHz RDI ADCP mounted on the top float. The TCHAIN was deployed from July 6, 2021 - August 11, 2022. Detailed analysis of the long-term moorings will be discussed elsewhere.

Fluorometer calibration

The Turner C-FLUOR fluorometer calibration uses the linear relationship $C = (V - a)b$ where C is the concentration in parts per billion, V the measured voltage, a an offset and b the calibration coefficient. The offset voltage was lower than the factory-provided value for both fluorometers used. For MP1, we used profiles before the dye release, and for the FCTD we used the upper 500 m of down-casts from the surface to measure the mean background voltage when zero dye was present. We

used the factory calibration coefficient for both fluorometers. This gave calibrations of $C_{FCTD} = (V_{FCTD} - 0.0140) * 31.1831$ and $C_{MP} = (V_{MP} - 0.0139) * 31.3309$. The minimum detectable level of the fluorometers was determined as three standard deviations above the mean background level. This gave minimum detectable concentrations of 0.06 ppb for the fluorometer on the FCTD and 0.006 ppb for the fluorometer on MP1. The factor of 10 difference between detection limits is likely due to individual sensor differences and an electrically noisier channel on the FCTD. Observed dye concentrations at MP1 were up to three times the detection limit. At the end of the FCTD survey, the levels were down to twice the detection limit.

Sampling uncertainty

Due to high flow speeds – up to 0.4 m s^{-1} along the canyon – the dye was advected rapidly along the canyon, requiring the dye survey to focus on two-dimensional transects through the patch. A source of uncertainty in our results comes from the resulting under-sampling of the dye patch. The two cross-canyon transects completed during the survey (Figure B.5h, i) show that lateral distribution of the dye varied in time or along the length of the patch. During the first cross-canyon transect, the dye was spread fairly uniformly across the canyon width; however, in the second transect, the dye was banked on the northeast side of the canyon. Thus, along-canyon transects, which focused on the canyon axis, may at times have sampled through only the edge of the patch.

With only the velocity measurements from MP1 (down-canyon of the dye for most of the experiment), it is difficult to estimate where in the cross-canyon direction the dye patch might have been. Along-canyon transects may have only sampled the front or back edge or a small section of the patch at times, particularly during later transects when the dye patch was large. Based on dye measurements from MP1 (Figure 2.2) we know the entire patch was ~4 km long at 20 hours after the release. Later along-canyon transects were all shorter than this (Figure B.8). It is possible that MP1, located in the

centre of the canyon, may have missed a large concentrated patch of tracer if it were banked against one wall.

To investigate the effect of under-sampling on estimates of the centre of mass we sub-sampled the cross-canyon transects (Figure B.5h, i), the longest along-canyon transects (Figure B.5b, c) and the time series (Figure B.5l). For each of these, subsets of 10 vertical profiles were taken in sequence across the transect to estimate the variability in the centre of mass and to simulate sampling just a fraction of the dye patch. Results are shown in Figure B.9. The effect of sub-sampling varies depending on the transect. The size of these standard deviations across different samples (Figure B.9) vary from transect to transect in a similar way to the standard deviations of the dye weighted density of each transects (bars in Figure B.7). This is likely to be because the length and temperature range of the transects impact the overall standard deviation as well. Since we cannot get an accurate estimate of the error due to sampling from all of the transects, we will use the standard deviation of the dye-weighted average as an estimate of the error.

However, this method may be insufficient when it comes to the shorter transects. If we look at transects e, f and g (Figure 2.3e, f, g), the temperatures measured are all warmer than 3.85°C (green temperature contour) and, particularly in transects f and g, dye concentrations were relatively weak. However, during transect h, which was in the cross-canyon direction, there is more concentrated dye colder than 3.85°C. This indicates that there was a concentrated, colder part of the dye patch not measured in the three previous transects and the true centres of mass may be colder than was measured. There is no way for us to accurately account for this error.

Another artefact of our sampling was due to the phase of the tide. For example, during the second transect (Figure B.5b) we sampled the dye in a down-canyon direction as the dye itself was moving down-canyon, causing the patch to appear spread over a larger extent than it was. This may be another source of error in our estimates.

Typically, long-term chemical tracer release surveys are designed to provide information on the three-dimensional spread of the tracer. Observations are often objectively mapped to higher resolution grids Ledwell et al. 1998. These maps provide an estimate of the fraction of tracer found. Doing such an inventory is difficult given the two-dimensional nature of our sampling pattern. However, since the focus of this study is the first rather than the second moment of the tracer, the results are less impacted by outliers.

2.5.2 Calculations

Estimating adiabatic versus diapycnal upwelling

Consider the situation in our canyon, which is equivalent to that in many past buoyancy and mass budget calculations (Hogg et al. 1982; St. Laurent et al. 2001): a volume bounded below by a sloping seafloor, on the sides by the canyon walls at, and on the top by a neutral surface γ_o which is a mean distance H above the bottom and has an area A_z out to the location of the inflow. A lateral flow $u_{in}(t)$ is incident beneath γ_o through a cross-sectional area of the canyon A_x. Volume conservation for an incompressible fluid requires one of two things to happen: γ_o can rise at a rate w_{adia}, which requires no mixing, or fluid can exit the volume via a divergent turbulent buoyancy flux, J_b, which produces a turbulent diapycnal velocity $w^* = \frac{1}{N^2}\frac{\partial J_b}{\partial z}$. Hence, at all times, the following balance must hold:

$$\int_{A_x} u_{in}(t) dA_x = \int_{A_z} w_{adia} dA_z + \int_{A_z} w^* dA_z. \tag{2.2}$$

Assuming u_{in}, w_{adia} and w^* are constant in space and the canyon width is constant, Equation 2.2 can be simplified to

$$A_x u_{in} = A_z (w_{adia} + w^*) \tag{2.3}$$

where the ratio $\frac{A_x}{A_z}$ is approximately equal to $\tan\alpha$ where α is the slope of the bathymetry. On very long timescales, the observed constancy of the ocean's stratification requires $w_{adia} = 0$, giving a balance between u_{in} and w^*. However, Figures B.2 and B.4 show that both u_{in} and w_{adia} vary in time, calling into question a steady state balance.

PDFs of estimated inflow below the 3.7°C isotherm ($u_{in}\tan\alpha$) from MP1 and $w_{adia} = \frac{d\eta_{3.7}}{dt}$, where $\eta_{3.7}$ is the isotherm displacement, demonstrate that generally w_{adia} (blue; Figure B.3) is significantly smaller than both $u_{in}\tan\alpha$ (red) and our estimates of w^* from dye (w_{dye}; grey shaded region). Velocities and temperatures were low-pass filtered at a period of 48 hours with a fourth-order Butterworth filter to remove the diurnal and semi-diurnal tides. The 3.7°C isotherm was chosen as it was on average ~ 100 m above the bottom and therefore within the region where near-boundary mixing occurs.

The MP1 mooring was deployed downstream of the dye release location and provides a estimate of the volume budget during the experiment. MP2, while not deployed at the same time as the dye experiment, also shows values of $u_{in}\tan\alpha$ (estimated for the 4.2°C isotherm with mean height ~ 100 m above bottom) that are in good agreement with the dye estimate of w^* and greater than w_{adia}, suggesting a longer-term balance between inflow and turbulent diapycnal velocity. While we cannot completely rule out the importance of time variability at the exact time and location of our dye release, our best estimates of the size of each term suggests that the dominant balance is between u_{in} and w^*, bolstering our comparisons with long-term estimates and our conclusions regarding the general circulation.

Centre of mass

For a dye or tracer of concentration C, the tracer-weighted average operator is defined as

$$\bar{(\cdot)} = \frac{\int\int\int (\cdot) C dx dy dz}{\int\int\int C dx dy dz}. \tag{2.4}$$

Here, we use the first moment of the tracer weighted average of the potential density anomaly ($\overline{\sigma_\theta}$), which represents the centre of mass of the dye in density space, to describe the location of the dye patch (Holmes et al. 2019; Ruan and Ferrari 2021). Ideally, the integral is performed on the full extent of the three-dimensional dye patch. In practice, however, we are limited to the spatial information of the survey. The integrals were estimated as sums in the vertical and along-transect directions for each transect through the dye patch.

Upwelling rate

Given the first density moment, the dye-weighted diapycnal velocity is given by $w_{dye} = -\frac{\partial_t \overline{\sigma_\theta}}{|\overline{\nabla \sigma_\theta}|}$ (Holmes et al. 2019; Ruan and Ferrari 2021). Because mixing acts on dye gradients as well as density gradients, the dye-weighted diapycnal velocity yields twice the dye-weighted density velocity, $\partial_t \overline{\sigma_\theta} = 2\overline{\dot{\sigma_\theta}}$, where $\mathrm{D}\sigma_\theta/\mathrm{D}t = \dot{\sigma_\theta}$ is the material derivative of the potential density anomaly (Ruan and Ferrari 2021). A total of 12 transects were completed over 3 days before dye concentrations became too low to detect. Below we describe four methods for estimating the diapycnal upwelling rate, the results of which are shown in Table 2.1.

The slope of a weighted linear regression is used to estimate the evolution of the dye's centre of mass over time ($\partial_t \overline{\sigma_\theta}$; Figure B.7). Weights chosen for the regression were $\mathcal{W} = \frac{n s_i^{-2}}{\sum_{i=1}^{n} s_i^{-2}}$ where s_i are standard deviations of dye weighted density for each transect $i = 1, \ldots, n$ and $n = 12$, such that transects with large standard deviations are weighted low. Linear regression (solid blue line in Figure B.7), with $\mathbf{R}^2 = 0.852$, yields $\partial_t \overline{\sigma_\theta} = -0.0341 \pm 0.0038$ kg m^{-3} day^{-1} where the error is given by the standard error of the slope of the fit. We approximate the density gradient with its vertical component ($\overline{\partial_z \sigma_\theta}$). Here, the horizontal gradient of the density is approximately 10 times smaller than the vertical component and, therefore, has a negligible impact on the vertical velocity. We calculate the dye-averaged vertical density gradient for each transect and

then use the weighted average over all the transects. The weights are equivalent to $\mathcal{W}$ but are a function of the standard deviations of the dye-weighted density gradient. The density gradient used for the calculation of w_{dye} is then $\overline{\partial_z \sigma_\theta} = -1.4 \times 10^{-4} \pm 0.3 \times 10^{-4}$ kg m^{-4}. For comparison, using all the FCTD data, without weighting by the concentrations, the average density gradient is $-2.0 \times 10^{-4} \pm 6.4 \times 10^{-4}$ kg m^{-4}. The weighted linear regression gives an upwelling velocity of 250 ± 75 m day^{-1}, assuming that errors associated with the time rate of change of the centre of mass and the centre of mass of the vertical gradient are independent. Temporal and spatial density gradients in this location are not independent due to the strong influence of the tide on the stratification, however, quantifying this effect on the centre of mass is difficult.

The linear regression can also be done without weighting (solid red line, Figure B.7). In this case, $\partial_t \overline{\sigma_\theta} = -0.0207 \pm 0.0055$ kg m^{-3} day^{-1} and $\overline{\partial_z \sigma_\theta} = -2.0 \times 10^{-4} \pm 4.7 \times 10^{-5}$ kg m^{-4}, yielding an upwelling velocity is 101 ± 50 m day^{-1}. For this fit, $\mathbf{R}^2 = 0.587$.

An alternative method for estimating the upwelling rate is to calculate pairwise estimates between transects (Drake et al. 2022). Given 12 individual estimates of the centre of mass, there are a total of 66 estimates of the upwelling rate between pairs of transects. The time evolution of the dye-weighted density ($\partial_t \overline{\sigma_\theta}$) is estimated by finite differencing between each observation, where the observation time is chosen to be the average time for the transect. That is, $(\partial_t \overline{\sigma_\theta})_{i,j} = \frac{(\overline{\sigma_\theta})_j - (\overline{\sigma_\theta})_i}{t_j - t_i}$. The average over all pairwise estimates is $\partial_t \overline{\sigma_\theta} = -0.0164 \pm 0.0052$ kg m^{-3} day^{-1} where the error is the standard error over all pairwise estimates. The spatial density gradient ($|\nabla \overline{\sigma_\theta}|$) is taken to be the average of the pair of tracer-weighted vertical density gradient estimates. The overall average for the vertical density gradient is the same as for the unweighted linear regression case. Taking the average of all 66 estimates of the upwelling rate gives 125 ± 31 m day^{-1} where the error is the standard error on the mean.

A final, fourth estimate of the upwelling rate can be calculated from the change in depth of the centre of mass during the experiment; we consider depth changes relative

to the bottom to avoid spurious upwelling due to tidal aliasing. Using the dye weighted average of the height above bottom, the height of the centre of mass during the first transect was 28 m above the bottom. Similarly, for the final observation during the time series, the average height of the centre of mass was 151 m above the bottom. Using the same time convention as for the pairwise method, the time difference between observations was 46 hours, giving an upwelling rate of 64 m day^{-1}.The change in density between the first and last observations was -0.0312 kg m^{-3} day^{-1}.

Table 2.1. Results of the four different estimates of the diapycnal upwelling rate (w_{dye}); a linear regression of the centre of mass weighted by the standard deviation of the dye weighted average, an unweighted linear regression to the centre of mass, an average over all estimates of the diapycnal velocity between each pair of transects, and the change in depth of the centre of mass between the first and last observations of the dye.

Method	w_{dye} **(m day^{-1})**
Weighted Linear Regression	250 ± 75
Unweighted Linear Regression	101 ± 50
Average of pairwise estimates	125 ± 31
Change in height above bottom	64

All four of these methods are imperfect: the weighted linear regression uses weights which may not be representative of the true sampling error; neither the unweighted linear regression nor the pairwise methods account for the sampling error at all; and the change in depth estimate does not account for the diapycnal component. However, all these methods give a significant positive velocity of $O(100\ m)$ and together provide confidence in our assertion that we observed diapycnal upwelling.

2.6 Acknowledgements

We thank the captain and crew of *RRS Discovery*, the National Marine Facilities technicians for assistance during the experiment and the engineers of the Multiscale

Ocean Dynamics group for their assistance and design and fabrication of the instrumentation. This work was funded by the Natural Environment Research Council (grant NE/S001433/1) and the National Science Foundation (grant OCE-1756264).

Chapter 2, in full, has been submitted for publication of the material as it may appear in Nature, 2024, Wynne-Cattanach, Bethan L., Couto, Nicole, Drake, Henri F., Ferrari, Raffaele, Le Boyer, Arnaud, Mercier, Herlé, Messias, Marie-José, Ruan, Xiaozhou, Spingys, Carl P., van Haren, Hans, Voet, Gunnar, Polzin, Kurt L, Naveira Garabato, Alberto and Alford, Matthew H.. The dissertation author was the primary investigator and author of this paper.

Chapter 3

Moored observations of bottom boundary layer breaking processes and interior exchange

A near-bottom volume budget is estimated using two mooring arrays deployed for 3 and 6 months, respectively, within a continental slope canyon. Driven by along-canyon convergences and divergences, the volume transport exchanged between the boundary layer and the interior varies on timescales of days to weeks. At tidal timescales, along-canyon variability in tidal flow leads to periodic ejection and suction of fluid from and into the boundary. Transports low-passed at 18 days suggest that ejection is persistent 5km from the canyon head, but exchange with the interior oscillates between ejection and suction such that the time-mean exchange is negligible moving in-shore. Estimates of the dissipation rate of turbulent kinetic energy and Richardson number from the moorings suggest that turbulence varies in both space and time within the canyon.

3.1 Introduction

Submarine canyons are found along the continental slopes of ocean basins worldwide and connect the deep ocean to the continental shelf (Harris and Whiteway 2011; Harris et al. 2014). Owing to their often steep and complex topography, canyons are

regions of enhanced turbulent dissipation relative to the open ocean (Kunze et al. 2012; Waterhouse et al. 2017; Alberty et al. 2017; Carter and Gregg 2002). Internal tides may be generated locally as barotropic tides scatter off the steep topography (Bell Jr. 1975). Both locally and remotely generated internal wave energy may be focused within the canyon topography as internal waves are reflected off the sidewalls (Hotchkiss and Wunsch 1982). The steep termini of canyons are also prone to backwards reflection such that waves radiate back along the canyon axes. The superposition of incoming and reflecting waves can lead to regions of shear and strain associated with enhanced dissipation (Alberty et al. 2017; Nazarian and Legg 2017; Waterhouse et al. 2017; Hamann et al. 2021). Internal wave breaking at the bottom of the canyon can also lead to elevated dissipation levels (Gregg et al. 2011).

Turbulent processes at sloping topographic features have long been recognized for their potential importance in water mass transformation (Munk 1966). Recent theoretical (Ferrari et al. 2016; De Lavergne, Madec, Le Sommer, Nurser, and Garabato 2016; McDougall and Ferrari 2017) and observational work (Wynne-Cattanach et al. 2023; Naveira Garabato et al. 2024) suggest that mixing at steep boundaries may lead to upwelling of deep water, necessary to maintain the global overturning circulation. Continental slope canyons, in particular, may be conduits for deep water to upwell (Allen and Durrieu de Madron 2009; Petruncio et al. 2002; Kunze et al. 2012).

Whether turbulence at boundaries could be of basin-scale significance has historically been a topic of debate (Garrett 1979; Armi 1979). Armi 1978 observed layers of well-mixed fluid detached from the topography, advecting into the ocean's interior, and hypothesised that the boundary mixing suggested by these well-mixed layers may account for the vertical mixing required in the deep ocean. Garrett 1979 argued that turbulence at boundaries would be an inefficient process, since mixing near the boundary would quickly lead to a well-mixed layer such that further turbulence would not result in the required water-mass transformation. The intense near-boundary turbulence to

which Armi 1978 attributed the well-mixed layers has since been observed at many sites (Polzin et al. 1997; Carter and Gregg 2002; Waterhouse et al. 2014). Observations of well-stratified turbulent layers above sloping boundaries (McPhee-Shaw et al. 2004; Nash et al. 2004; Alford et al. 2024) call into question how these highly turbulent regions are restratified. Using theoretical 1-d models, it has been shown that sloping isopynals may drive a secondary circulation that stratifies the boundary (Garrett 1990; Umlauf and Burchard 2011). However, these models do not include the internal wave dynamics and 3-d effects expected to be important, particularly with canyons (Winters 2015).

Non-uniformity in topographic slope, seafloor roughness, internal wave forcing, stratification and turbulence along a canyon can lead to 2-d and 3-d convergences of up-slope turbulence driven transport (Kunze et al. 2012). This leads to exchange of fluid between the near-boundary region and the interior, as evidenced by observations of internal nephloid layers (layers of suspended sediment) and oxygen anomalies (McPhee-Shaw et al. 2004; McPhee-Shaw et al. 2021). Lateral dispersal could be important for sediment transport and other tracers such as carbon, nutrients and iron which are crucial for coastal ecosystems (Ryan et al. 2005).

This study presents moored time series from an experiment conducted within a submarine canyon with the objective of determining the processes which may lead to exchange of boundary and interior fluid. Previous results from a dye release during the same experiment show evidence of along-isopycnal transport of dye away from the boundary (Wynne-Cattanach et al. 2023). However, the dye was only observed for 3 days so was insufficient to fully explore the boundary and interior exchange. Here, we take advantage of the geometry of the mooring deployment and the length of the time series to investigate the possibility of boundary and interior exchange by calculating a volume budget for the near-boundary region to estimate along-isopycnal transport into the interior. To our knowledge, this is the first attempt at a 3-dimensional near-bottom volume budget. A secondary objective of this study was to investigate the spatial

and temporal variability in turbulence and mixing within the canyon. We compare measurements of velocity, temperature and turbulent dissipation between moorings which were placed along and across the canyon.

3.2 Background

3.2.1 Study Region

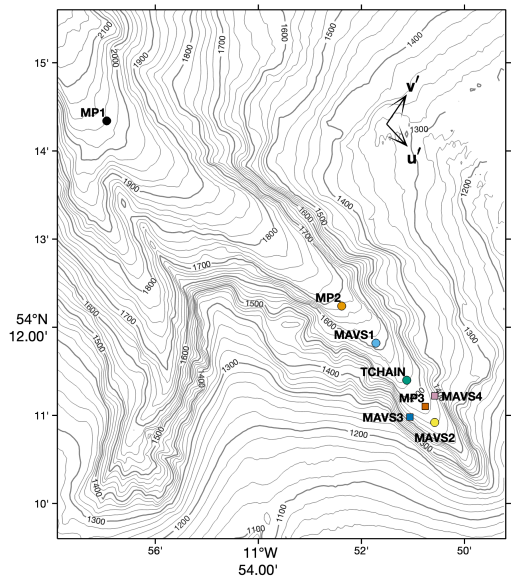

Figure 3.1. Locations of all the moorings deployed during BLT1 (circles) and BLT2 (squares).

The Boundary Layer Turbulence and Abyssal Recipes (BLT) Experiment focused on the near-bottom flow and turbulent dynamics within a canyon on the eastern side of the Rockall Trough; a deep channel located in the northeast North Atlantic. The eastern slope of the Rockall Trough rises up to the European continental shelf and is incised by canyons along its length. The particular canyon chosen for this study is 9 km wide at the mouth and 32 km long, with canyon wall heights of approximately 400 m. The canyon forks into a southward and south-eastward branch about halfway along it's length. This study focused on the south-eastward branch. The region has strong

Table 3.1. Details of each of the moorings deployed during the BLT experiment

Mooring Name	Longitude (°)	Latitude (°)	Depth (m)	Height (m)	Deployment Date	Recovery Date
MP1	-11.949	54.239	2035	600	28-Jun-21	01-Jul-21
MP2	-11.873	54.204	1676	600	07-Jul-21	06-Oct-21
MP3	-11.846	54.185	1491	600	22-Oct-21	02-Aug-22
MAVS1	-11.862	54.197	1614	300	06-Jul-21	09-Oct-21
MAVS2	-11.843	54.182	1465	300	07-Jul-21	07-Oct-21
MAVS3	-11.851	54.183	1434	300	22-Oct-21	05-Aug-22
MAVS4	-11.843	54.187	1455	300	22-Oct-21	08-Aug-22
TCHAIN	-11.852	54.19	1529	180	06-Jul-21	11-Aug-22

internal tides (Wynne-Cattanach et al. 2023; van Haren et al., submitted). The canyon's thalweg is approximately critical to the semi-diurnal internal tide for most of it's length. Near the location of the TCHAIN the slope steepens to supercritical. The walls of the canyon are supercritical.

3.2.2 Experiment and instrumentation

The experiment consisted of three cruises during which there were a dye (Wynne-Cattanach et al. 2023) and chemical tracer release, microstructure surveys (Alford et al. 2024) and mooring deployments (van Haren et al., submitted; Naveira Garabato et al. 2024). In this study, we consider the long-term mooring deployments. During the first cruise (BLT1) five moorings were deployed: one short-term moored profiler (MP1) which was placed near the fork of the canyon (not considered in this analysis), and four long-term moorings which were deployed further up the canyon for 3 months (MP2, MAVS1, MAVS2 and TCHAIN). All but the TCHAIN mooring were recovered and re-deployed during the second cruise (BLT2; MP3, MAVS3 and MAVS4) (Table 3.1; Figure 3.1). The moorings sampled for another 6 months before recovery during the third cruise (BLT3).

Moored Profilers - MP1, 2 and 3

The MP moorings were 600 m tall and had a RDI Longranger 75 kHz ADCP mounted on the top float. They were equipped with a McLane Moored Profiler, outfitted

with a Seabird SBE52 CTD and an FSI ACM travel time current meter. MP1 also had a fluorometer and an Epsilometer. The moored profiler was set to continuous profiling mode and collected about one 500 m profile every 30 minutes. MP1 was deployed at a depth of 2035 m, MP2 at 1676 m and MP3 at 1491 m.

MAVS - MAVS1, 2, 3 and 4

Each MAVS mooring was 300 m tall and consisted of 8 MAVS travel time sensors, ~80 RBR Solo or Seabird SBE56 thermistors and an RDI Longranger 75 kHz ADCP mounted on the top float and one Seabird SBE37 CTD. The instrument spacing was denser towards the bottom of the mooring. The deepest temperature sensors were placed on the acoustic releases ~ 3 m above the bottom. The sensors were ~1 m apart on the bottom 40 m of the mooring, increasing to 2 m from 40 to 60 m, then 3 m from 60 to 80 m, then 5-6 m spacing from 80 m to the top of the mooring at 300 m above the sea floor. The thermistors sampled at 2 Hz. MAVS1 was deployed at a depth of 1614 m, MAVS2 at 1465 m, MAVS3 at 1434 m and MAVS4 at 1455 m.

TCHAIN

The TCHAIN consisted of a 150 m thermistor chain with 102 pre-attached thermistors. The bottom-most thermistor was attached to the acoustic release and was 0.9 m above the bottom. The lowest two thermistors were 0.5 m apart, the following 51 were at 1 m intervals and the remaining 50 were at 2 m intervals. An RDI Longranger 75 kHz ADCP was mounted on the top float of the mooring. Observations from the TCHAIN mooring are discussed in detail in van Haren et al 2024.

3.3 Methods

3.3.1 Volume Budget

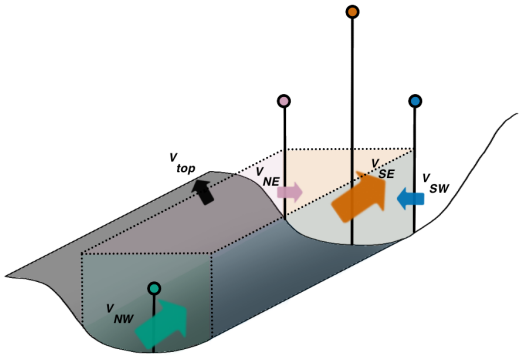

Figure 3.2. Schematic of the volume used for the budget, defined by the locations of the four moorings.

A volume budget is used to estimate the transport in and out of the near-boundary region due to non-uniformity in the flow along the canyon. Convergence of flow along the slope must be balanced by ejection of near-boundary fluid into the interior, while divergence of the along-slope flow must be balanced by suction of interior fluid into the near-boundary region (Kunze et al. 2012). We use the locations of the moorings deployed during BLT2 to define a box as shown in Figure 3.2. The box is bounded on the down-canyon (north-west) edge by the along-canyon location of the TCHAIN mooring (x_{NW}) and on the up-canyon (south-east) edge by the along-canyon location of MP3, MAVS3 and MAVS4 (which form a line in the cross-canyon direction; x_{SE}). The north-eastern side of the box is defined by the cross-canyon location of MAVS4 (y_{NE}) and the south-western side of the box is defined by the cross-canyon location of MAVS3 (y_{SW}). The box is bounded below by the bathymetry (z_{bath}), and the top of the box is defined as 200 m above the canyon thalweg (z_{200}). This depth range was chosen to encompass the region within which the turbulent mixing is observed

to occur - dissipation is enhanced near the bottom due to convective overturns with vertical scales of 100-200 m (Naveira Garabato et al. 2024). We calculate the budget in a rotated reference frame. Hereinafter, u and v refer to along- and across-canyon velocity components, respectively. Along-canyon velocity is defined as positive towards the head of the canyon and cross-canyon velocity is defined as positive to the north-east, perpendicular to the direction of the canyon axis.

The volume budget follows from the volume integral of the continuity equation. That is, given $\nabla \cdot \vec{u} = 0$, where $\vec{u}$ is the 3-d velocity vector,

$$\iiint_V \nabla \cdot \vec{u}\, dV = \oiint \vec{u} \cdot \hat{n}\, dS = 0 \tag{3.1}$$

following the divergence theorem, where V is the volume defined by the box, S denotes the surface of the box and $\hat{n}$ is the unit vector normal to S. Given no transport through the seafloor, the volume budget is then

$$\begin{aligned} &\underbrace{\int_{z_{bath}}^{z_{200}} \int_{y_{SW}}^{y_{NE}} u(x_{NW})\, dydz}_{V_{NW}} - \underbrace{\int_{z_{bath}}^{z_{200}} \int_{y_{SW}}^{y_{NE}} u(x_{SE})\, dydz}_{V_{SE}} + \underbrace{\int_{z_{bath}}^{z_{200}} \int_{x_{NW}}^{x_{SE}} v(y_{SW})\, dxdz}_{V_{SW}} \\ &- \underbrace{\int_{z_{bath}}^{z_{200}} \int_{x_{NW}}^{x_{SE}} v(y_{NE})\, dxdz}_{V_{NE}} + \underbrace{\int_{y_{SW}}^{y_{NE}} \int_{x_{NW}}^{x_{SE}} w\, dxdy}_{V_{top}} = 0. \end{aligned} \tag{3.2}$$

For each component, the velocity is taken to be the depth average along/cross-canyon velocity over the bottom 200 m from the closest mooring. At x_{NW} the velocity from TCHAIN is used to give the along-canyon transport at the down-canyon edge of the box (V_{NW}), at x_{SE} the velocity from MP3 is used to give the along-canyon transport at the up-canyon edge of the box (V_{SE}), at y_{SW} the velocity from MAVS3 is used to give the transport out of the south-west side of the box (V_{SW}) and at y_{NE} the velocity from

MAVS4 is used to give the volume transport out of the north-east side of the box (V_{NE}). The volume transport out of the top of the box (V_{top}) is taken to be the residual of the first four terms and represent the exchange between the boundary and the interior.

We will first consider the transport occurring at tidal timescales using the full time series of the volume transports. To investigate the longer-timescale variability in the transport we will use a running mean of the transports with 18-day window lengths. This window length removes the variability due to the tides, including the spring-neap cycle.

3.3.2 Phase averages

Full record phase average

Phase-averaged pictures of the velocities and other variables such as temperature and isotherm displacement were constructed to obtain a robust estimate of the variability over an M2 tidal cycle. The phase-averages for each record were computed in reference to a harmonic fit of the TPXO barotropic tide with M2 tidal frequency.

Phase lags

To investigate the progressive nature of the semi-diurnal internal tide within the canyon we compute the phase of the depth-averaged semi-diurnal isotherm displacement at each mooring by harmonic analysis over a 2.1 day sliding window (Zhao et al. 2012). This length of window was chosen to capture subtle changes in the phase of the semi-diurnal tide. The phase lag $\Delta\phi$ is then the difference in phase between pairs of moorings and the phase speed of the wave is $\Delta x \Delta\phi$ where Δx is the distance between the moorings.

3.3.3 Normal modes

The vertical structure of internal waves can be represented as the sum of n eigenmodes which are the solutions to

$$\frac{d^2\eta(z)}{dz^2} + \frac{N^2(z)}{c_i^2}\eta(z) = 0 \tag{3.3}$$

with boundary conditions $\eta(0) = \eta(H) = 0$ where η is the displacement of isopycnals, H is the water depth, N is the buoyancy frequency and c_i, $i = 1, \ldots, n$ are the eigenvalues (Alford 2003). The phase speed of the internal wave is related to the eigenspeed by the dispersion relation,

$$c_p = \frac{\omega}{\sqrt{\omega^2 - f^2}} c_i \tag{3.4}$$

where ω is the wave frequency and f is the inertial frequency (Alford and Zhao 2007).

The vertical modes are estimated using time-average stratification from 25 hours of full depth temperature and salinity profiles collected using the shipboard CTD (Figure 3.3). The CTD station was halfway between the location of MP2 and MAVS1 along the canyon.

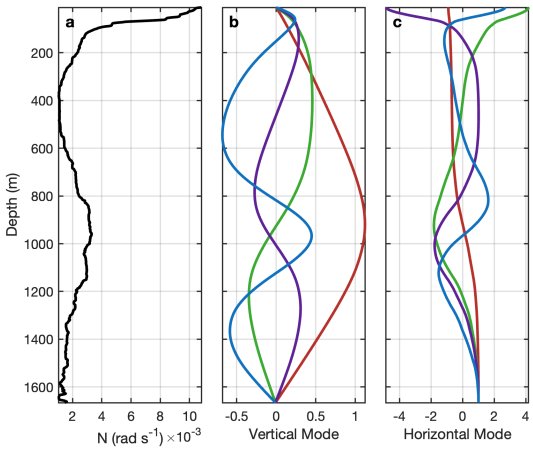

Figure 3.3. (a) Time averaged buoyancy frequency from a 25 hour CTD station between MP2 and MAVS1 (b) Vertical velocity modes (c) Horizontal velocity

3.3.4 Calculation of dissipation

Estimates of the dissipation rate of turbulent kinetic energy (ϵ) from overturns were obtained from the thermistor sensors on the MAVS moorings following methods similar to those proposed by Thorpe (1977), with details described in, for example, van Haren et al. 2022. In this region density depends linearly on temperature (van Haren et al., submitted), allowing us to use it in place of temperature when estimating overturning scales. Profiles of temperature are reordered into a stable, monotonic profile and the resulting displacements (d) are used to estimate ϵ as

$$\epsilon = 0.64 d^2 N^3 \tag{3.5}$$

where N is the local buoyancy frequency computed from the stable density profiles. In contrast to most examples of this methods, here we use individual estimates of d as the overturning scales rather than the root mean square of displacements within a single overturn (van Haren et al. 2022). The same method was applied to the MP2 mooring but less estimates were lower resolution due to the frequency of the profiles. Turbulent dissipation computed this way is consistent with that measured directly with microstructure (Alford et al. 2024).

3.3.5 Calculation of Richardson number

The Richardson number, defined as $Ri = \frac{N^2}{S^2}$ where $N^2 = -\frac{g}{\rho_0}\frac{\partial \rho}{\partial z}$ is the stratification and $S^2 = (\frac{\partial u}{\partial z})^2 + (\frac{\partial v}{\partial z})^2$ is the squared shear, describes the tendency for a Kelvin-Helmholtz instability to occur. It has been shown in an inviscid, stably stratified fluid that the flow will be unstable when $Ri < \frac{1}{4}$ (Miles 1961; Miles and Howard 1964). Stratification was estimated from the thermistors on the MAVS moorings assuming that density varies linearly as a function of temperature. Shear was estimated from the downward looking ADCPs on the moorings with a vertical resolution of 16 m.

3.3.6 Calculation of buoyancy flux due to advection

To investigate the possibility that differential advection of dense water over light water, leading to convective instabilities, is the source of mixing near the bottom of the canyon we estimate the destabilising buoyancy flux due to advection following Moum et al. 2004; Ruan et al. 2019. Assuming a linear equation of state for density where $\rho = \rho_0(1 - \alpha T)$, the buoyancy flux is given by

$$J_b = g\alpha \int_0^h u' \frac{\partial T}{\partial x'} \, dz' \tag{3.6}$$

where primes denote that the axes have been rotated to be parallel and normal to the slope, u' is then the along-slope velocity and $\frac{\partial T}{\partial x'}$ is the along-canyon density gradient. We estimate this integral as a sum

$$J_b = g\alpha \sum_{z'=0}^{h} u'(z') \frac{\partial T(z')}{\partial x'} \Delta z' \tag{3.7}$$

and perform the calculation using phase averaged quantities. Since velocities at the moorings do not reach the bottom, the profiles of u' were extended using a spline interpolation to meet the $u' = 0$ condition at the seafloor.

3.4 Results

3.4.1 Flow conditions

Figure 3.4. Along- and cross-canyon velocities for example time periods for each of the moorings. Temperature is contoured in black with isotherms every 0.25 °C. Note the different times for the three different deployments: MP1 during BLT1, MP2-MAVS2 between BLT1 and BLT2 and MAVS3-MAVS4 between BLT2 and BLT3.

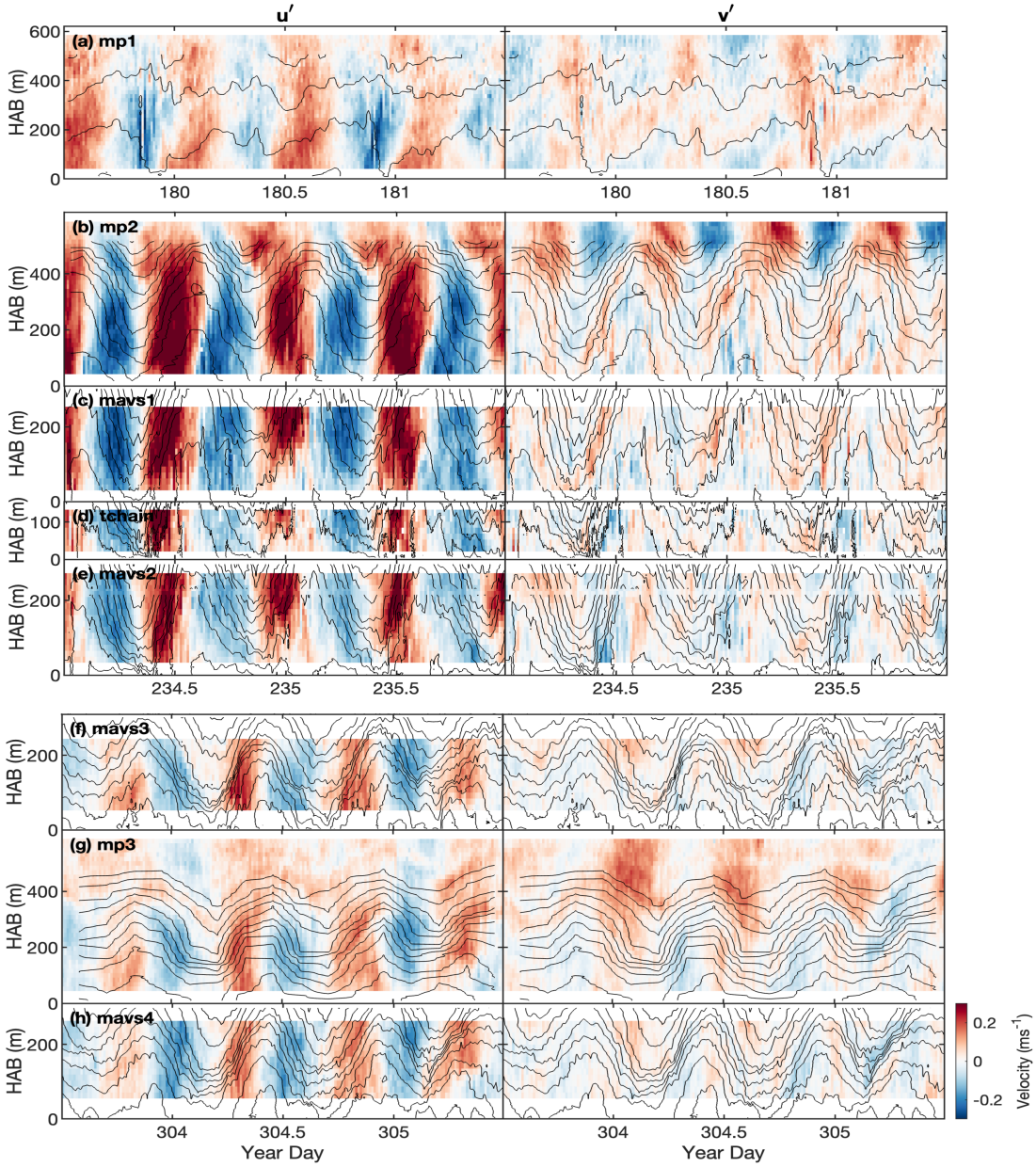
u′
v′
(a) mp1
(b) mp2
(c) mavs1
(d) tchain
(e) mavs2
(f) mavs3
(g) mp3
(h) mavs4
HAB (m)
Year Day
Velocity (ms^{-1})
0.2
0
-0.2

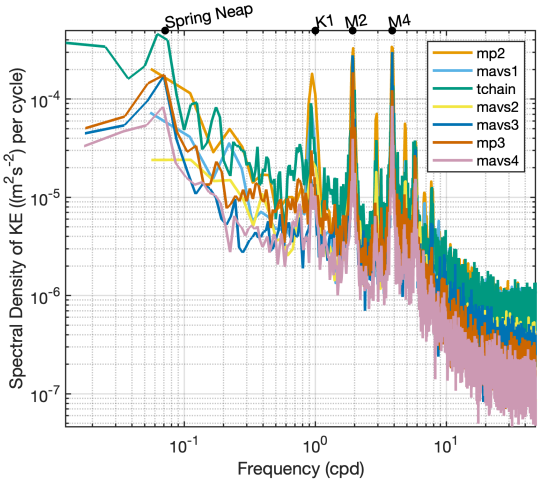

Figure 3.5. Spectrum of kinetic energy averaged over the bottom 100m for each mooring.

Moored observations within the canyon reveal a rectilinear flow along the canyon within the bottom 400 m of the water column (Figure 3.4.1). Kinetic energy within the canyon was dominated by the semi-diurnal and diurnal tides and their harmonics (Figure 3.5). The spring-neap cycle in the kinetic energy was in phase with the barotropic tide (Wynne-Cattanach et al. 2023), indicative of local internal tide generation due to the interaction between the barotropic tide and the topography.

The low frequency flow in the canyon was weaker than the tide and showed predominantly up-canyon flow (Figure 3.6). The moorings on the side-walls, particularly MAVS4, saw more variability in the flow direction. The time mean along-canyon flow was up-canyon at all mooring locations. Velocities were strongest further down the canyon, decreasing in magnitude from MP2 to MAVS2. All of the moorings deployed near the canyon head showed peak velocities aloft (between 100 and 200 m above the bottom). In contrast, velocities at MP1 (which was deployed near the fork of the canyon) increased all the way to the lowest measurement (~ 25 m above the bottom) such that the sign of the velocity shear near the bottom is opposite between the two regions of the canyon. A negative vertical shear will drive differential advection of cold water above warm water, leading to convective breaking of the internal tide within the canyon.

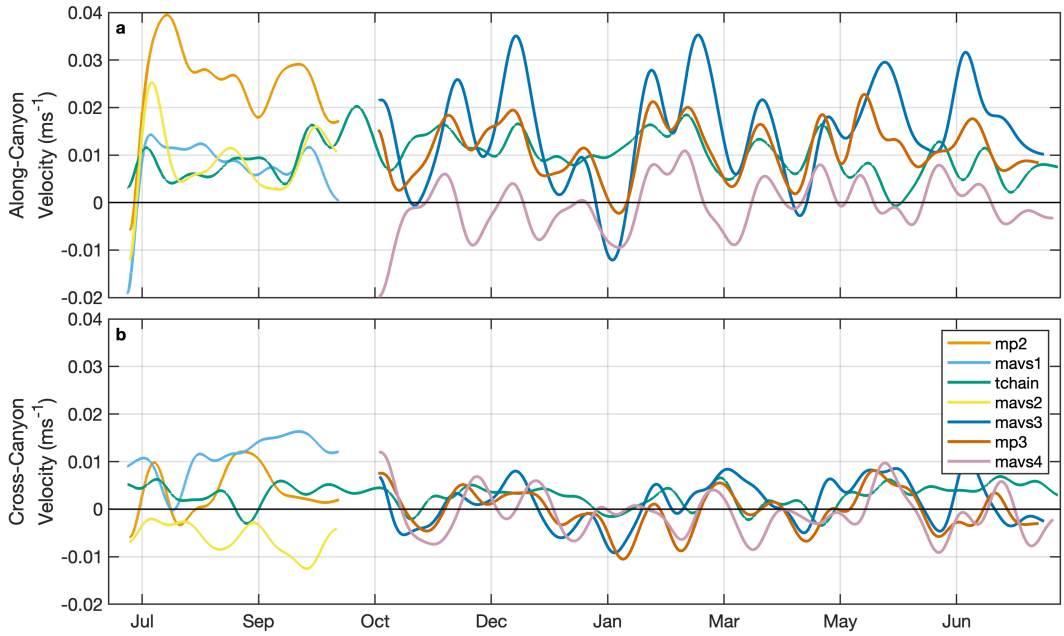

Figure 3.6. Depth-averages of low-pass filtered (a) along-canyon and (b) cross-canyon velocities within the bottom 200 m from each of the moorings. The low-pass filter was applied at a period of 18 days.

This occurs during up-canyon flow at the moorings near the canyon head, but during down-canyon flow at MP1.

3.4.2 Tidal phase averages

Along-canyon M2 tide phase averages of temperature and velocity, calculated over the full 3 month record of the BLT1 mooring deployment, show that during up-canyon flow the internal tide brings cold water up the canyon (Figure 3.7). During down-canyon flow isopycnals flatten as cold water flows back down the canyon. Vertical and horizontal gradients in the velocity cause cold water to be advected over warm water, leading to convective instabilities. Phase averages show again that the along-canyon velocities are much stronger than the cross-canyon. During the up-canyon phase of the tide, vertical velocities are positive.

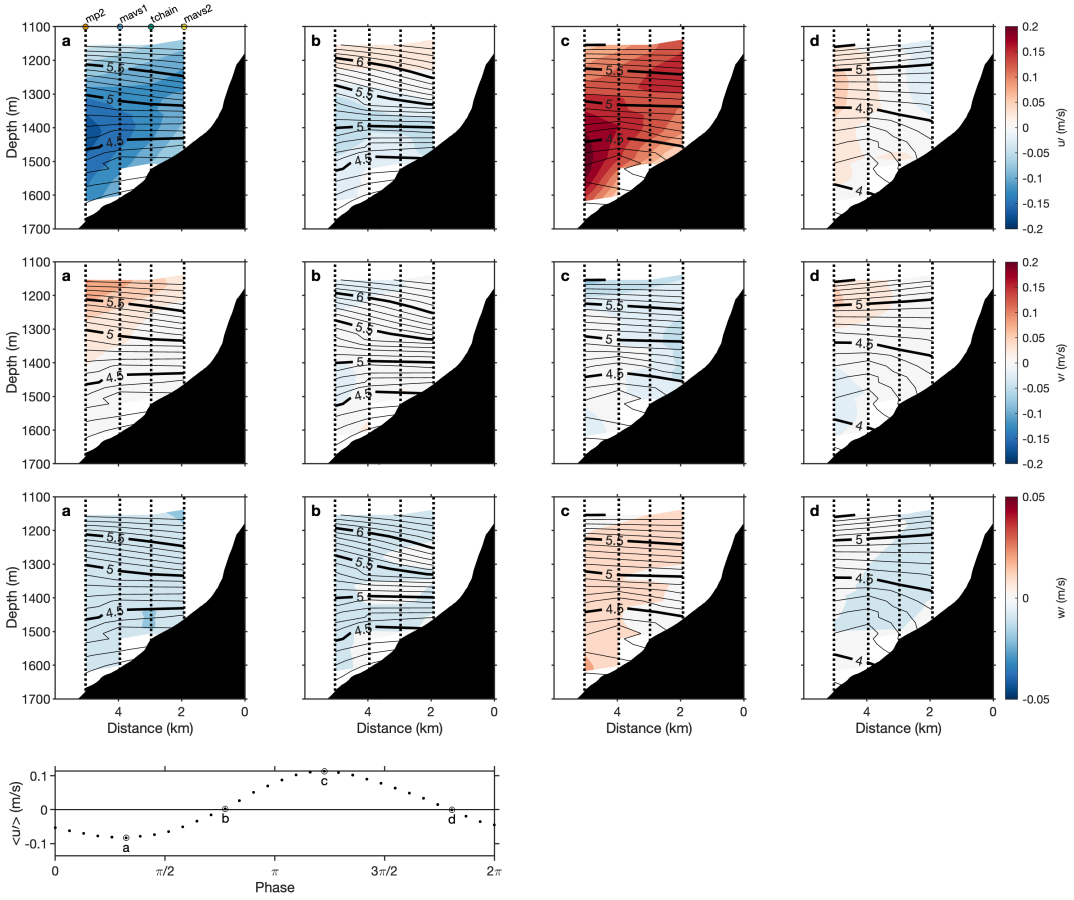

Figure 3.7. Phase-averages of along-canyon velocity (top row), cross-canyon velocity (middle row) and vertical velocity (vertical row) at four phases of the M2 internal tide, shown in each column: (a) Peak down-canyon flow, (b) first slack tide, (c) Peak up-canyon flow and (d) second slack tide. In each panel isotherms are contoured in black with thin contours every 0.1°C and thick contours every 0.5°C. Vertical dashed lines show the locations of each mooring between which velocity and temperature are interpolated. Note that the temperature data from TCHAIN is not included in the interpolation due to calibration issues. The bottom panel shows the depth-averaged along-canyon velocity at TCHAIN as reference.

We use the moorings deployed during the 6-month BLT2 deployment to look at the cross-canyon M2 tide phase averages (Figure 3.8). Velocities from downward looking ADCPs from MP3, MAVS3 and MAVS4 are used, but the motor on the moored profiler on MP3 broke 17 days into the deployments so temperature data comes from the thermistors on MAVS3 and MAVS4 only. Velocities were not uniform across the

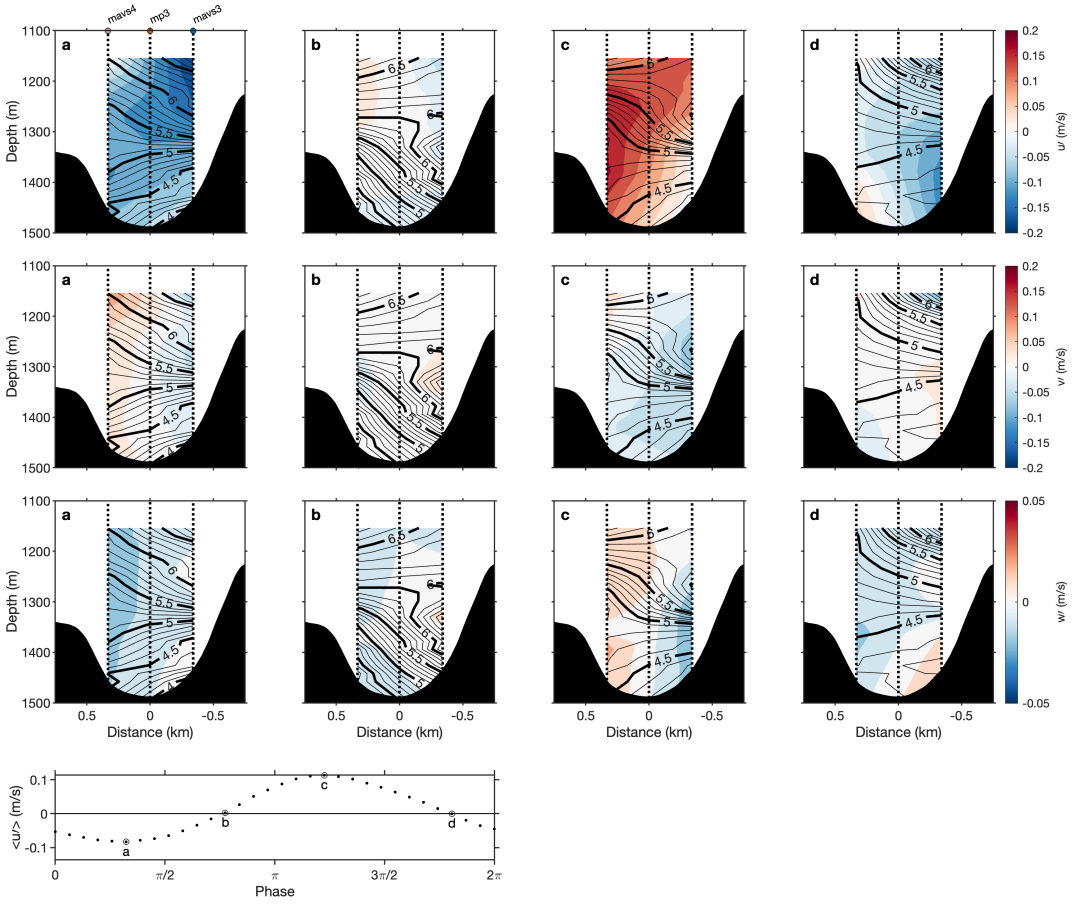

Figure 3.8. Phase-averages of along-canyon velocity (top row), cross-canyon velocity (middle row) and vertical velocity (vertical row) at four phases of the M2 internal tide, shown in each column: (a) Peak down-canyon flow, (b) first slack tide, (c) Peak up-canyon flow and (d) second slack tide. In each panel isotherms are contoured in black with thin contours every 0.1°C and thick contours every 0.5°C. Vertical dashed lines show the locations of each mooring between which velocity and temperature are interpolated. Note that the temperature data from MP3 is not included in the interpolation due to calibration issues. The bottom panel shows the depth-averaged along-canyon velocity at TCHAIN as reference.

canyon; the down-canyon velocities were strongest above the bottom on the south-west side of the canyon (right side of panels in Figure 3.8). Cross-canyon velocities were divergent away from the centre of the canyon during peak down-canyon flow but convergent towards the centre following down-canyon flow. Isopycnals transitioned from banking on the south-west side of the canyon to the north-east side of the canyon

and stratification was increased. During up-canyon flow, isopycnals returned to being banked on the south-west side and warm water was brought up to the mooring locations and stratification was weaker. Velocities were strongest on the north-east side of the canyon (left side of panels), coincident with the strongest upwelling velocities. Cross-canyon flow was towards the south-west.

3.4.3 Phase lags

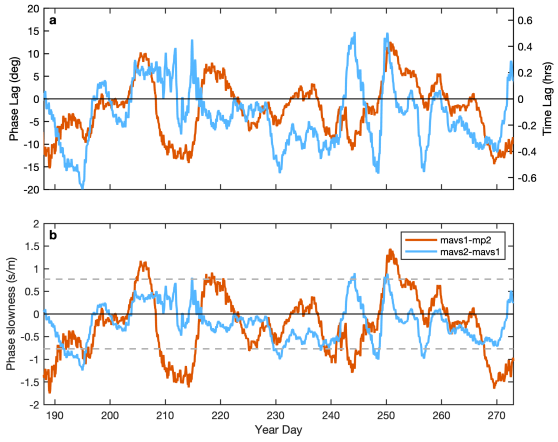

Figure 3.9. (a) Phase lag estimated using harmonic fits to two-day windows between MAVS1 and MP2 (orange) and MAVS2 and MAVS1 (blue) (b) Phase slowness (1/phase speed) corresponding to the phase lags in (a). Dashed red lines show the phase slowness of the theoretical mode 1 M2 internal tide for up- and down-canyon propagating wave.

The series of moorings along the canyon axis allows us to investigate the propagation of features along the canyon. Time lags in velocities between along-canyon locations will lead to convergence and divergences along the canyon. Here, we use the isopycnal displacement, as described in Methods, to estimate the phase propagation between MP2 and MAVS1 and MAVS1 and MAVS2. We find phase lags that vary from between $-15°$ to $15°$ or, equivalently, lags of approximately -0.5 to 0.5 hours where a positive lag means that the down-canyon mooring leads the up-canyon mooring (Figure 3.9). The phase lags are small and oscillate around zero, possibly indicative of a partially standing wave as has been seen in other canyons (Eel Canyon; Waterhouse et al. 2017 and Monterrey Canyon; Zhao et al. 2012). We then estimate the phase slowness (i.e. the reciprocal of phase speed such that as phase speed tends to infinity phase slowness tends to zero) and compare to the theoretical phase speed of the internal tide. Given the time average stratification from the full depth CTD station, the phase speed of the theoretical mode 1 internal tide is 1.27 ms^{-1}. There are times where there is propagation

that agrees with a propagating mode 1 wave. However, at other times, the slowness tends to zero, suggesting that there is a standing wave within the canyon. The phase lags between MAVS1 and MAVS2 are more variable than between MP2 and MAVS1 suggesting that the flow may de-cohere and become more complicated as it travels up the canyon.

Note that the wavelength of the mode 1 internal tide given the theoretical phase speed is 35 km, much longer than the separation of the moorings, therefore phase differences are small and prone to errors due to noise in the signal.

3.4.4 Volume Budget

Tidal

Convergence of volume within the box must be balanced by transport out of the box while divergence will lead to transport into the box. We interpret these slope-normal transports as ejection of boundary layer fluid into the interior and suction of interior fluid into the boundary layer, respectively (Kunze et al. 2012). At tidal time scales, the volume transports estimated at each side of the box show that the magnitude of the along-canyon transports greatly exceed that of the cross-canyon transport (Figure 3.10). This is expected due to the rectilinear nature of the flow within the canyon and has been seen in other canyons (Kunze et al. 2012). The peak magnitudes in the along-canyon transports (V_{NW} and V_{SE}) are up to four times larger than the cross-canyon transport (V_{SW} and V_{NE}) such that the variability in the along-canyon direction dominates the transport into and out of the boundary region (Figure 3.10). Periodic ejection from and suction into the boundary region occurs with the semi-diurnal tide, as seen by Wynne-Cattanach et al. 2023. The oscillations in V_{top} demonstrate an asymmetric, saw-tooth pattern. Transport decays to zero until the peak down-canyon transport. Suction occurs during the transition from up-canyon to down-canyon transport. The shift from suction to ejection coincides with when the transport into the box at the down-canyon end

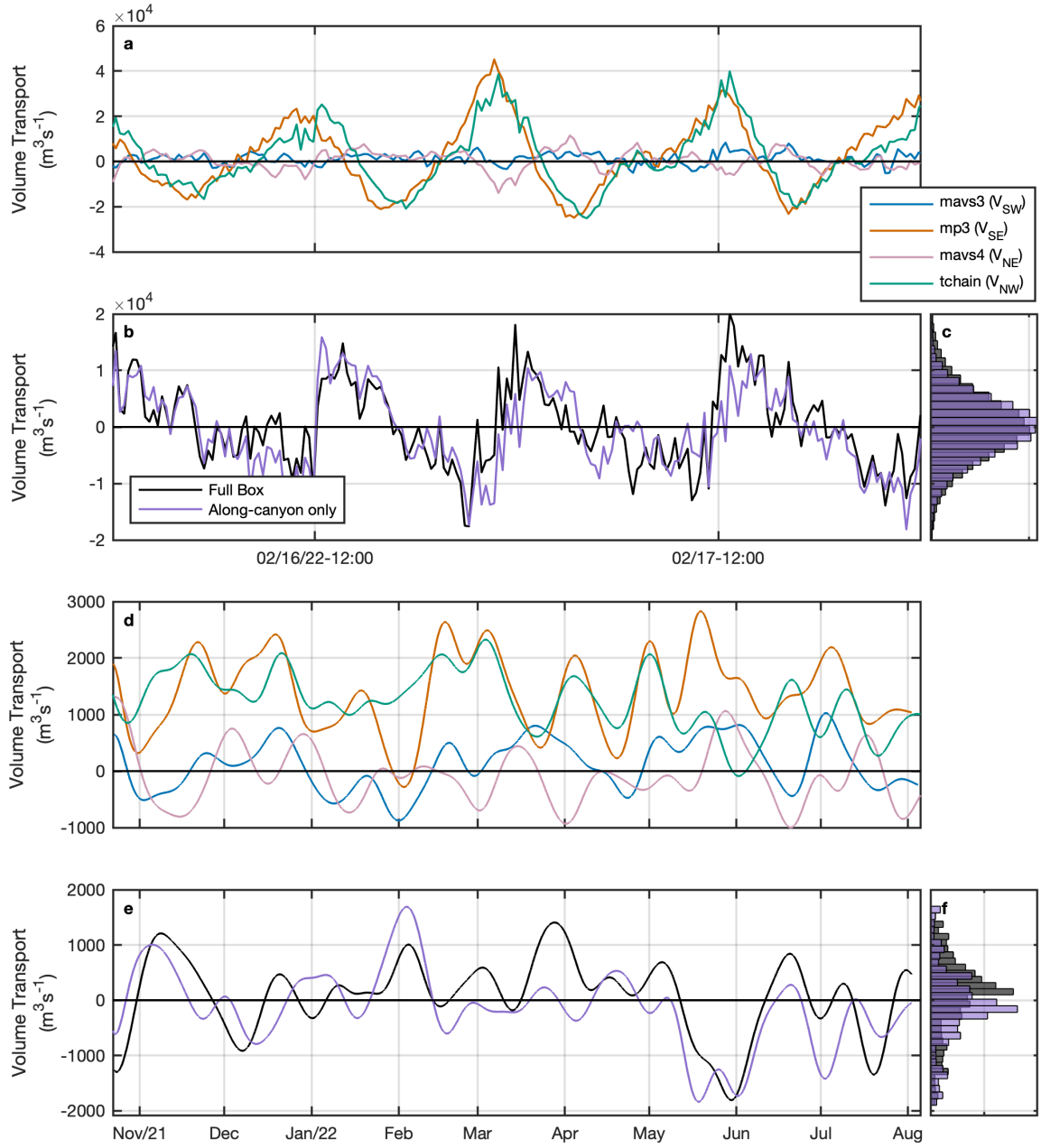

Figure 3.10. (a) 2 day time-period of the volume transport V_{NW}, V_{SE}, V_{SW} and V_{NE}. (b) The resulting volume transport out the top of the box (V_{top}) considering all four transports (black) and just the along-canyon transport (purple). (c) PDF of the total transport out of the box from all four moorings (black) and just the along-canyon moorings (purple). (d), (e) and (f) are the same as (a), (b) and (c) but for the full record low pass filtered at a period of 18 days.

exceeds the transport out of the box at the up-canyon end ($V_{NW} > V_{SE}$). During the period shown here, the velocity at MP3 leads that at TCHAIN (i.e. phase propagation is down-canyon). At other times, not shown here, when velocity at the TCHAIN leads the velocity at MP3, the saw tooth is the opposite direction and the step change is from ejection to suction when the transport out of the box exceeds the transport into the box. There are also periods where the phase difference between the moorings is smaller and less of a tidal cycle is seen in the suction and ejection.

Sub-tidal

At longer timescales (low-pass filtered at a period of 18 days), flow is predominantly up-canyon and is ~2.5 times larger than the cross-canyon flow (Figure 3.10). Again, the flow is not uniform along the canyon, leading to convergence or divergence and hence transport out of and into the boundary layer. Convergence events (ejection) are more frequent than divergence events (Figure 3.10c). The average transport out of the box is 17% of the average volume incoming at the down-canyon end of the box over the 6-month deployment. Comparing the results of the full volume budget to just the transport due to the along-canyon variability (black versus purple lines in Figure 3.10), shows that most of the large convergence/divergence events are due to along-canyon variability except for one large event in April and smaller events in March, May and June which are due to differences in the cross-canyon components since at these times the along-canyon transports are comparable in magnitude. At sub-tidal timescales, along-canyon transport is always up-canyon and therefore convergence or divergence is due to differences in the magnitude of the up-canyon transport and never due to a difference in the sign of the transport.

3.4.5 Along-canyon only volume budget

Tidal

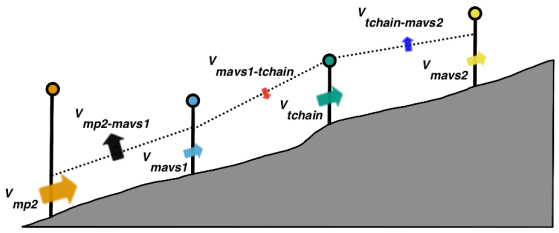

Figure 3.11. Schematic of the along-canyon volume budget.

Given the dominance of the along-canyon transport in the volume budget above, we can repeat the analysis with the along-canyon mooring array to investigate the variability in the transport along the canyon. Since there are four moorings, we can define volumes between each pair, providing estimates of the volume transport into or out of the boundary at three locations along the canyon's length (Figure 3.11). The pairs are MP2 and MAVS1, furthest down the canyon, then MAVS1 and TCHAIN, and finally TCHAIN and MAVS2 closest to the head of the canyon. For comparison, the MP3 and MAVS3/4 moorings used for the previous volume budget were located between TCHAIN and MAVS2. We now assume that the volume transport out of the sides of the box (V_{SW} and V_{NE}) are zero such that the volume budget for the boxes defined by each pair of moorings (moor1 and moor2) is then

$$\underbrace{\int_{z_{bath}}^{z_{200}}\int_{y_{SW}}^{y_{NE}} u(x_{moor1})\,dydz}_{V_{moor1}} - \underbrace{\int_{z_{bath}}^{z_{200}}\int_{y_{SW}}^{y_{NE}} u(x_{moor2})\,dydz}_{V_{moor2}} + \underbrace{\int_{y_{SW}}^{y_{NE}}\int_{x_{moor1}}^{x_{moor2}} w\,dxdy}_{V_{moor1-moor2}} = 0. \tag{3.8}$$

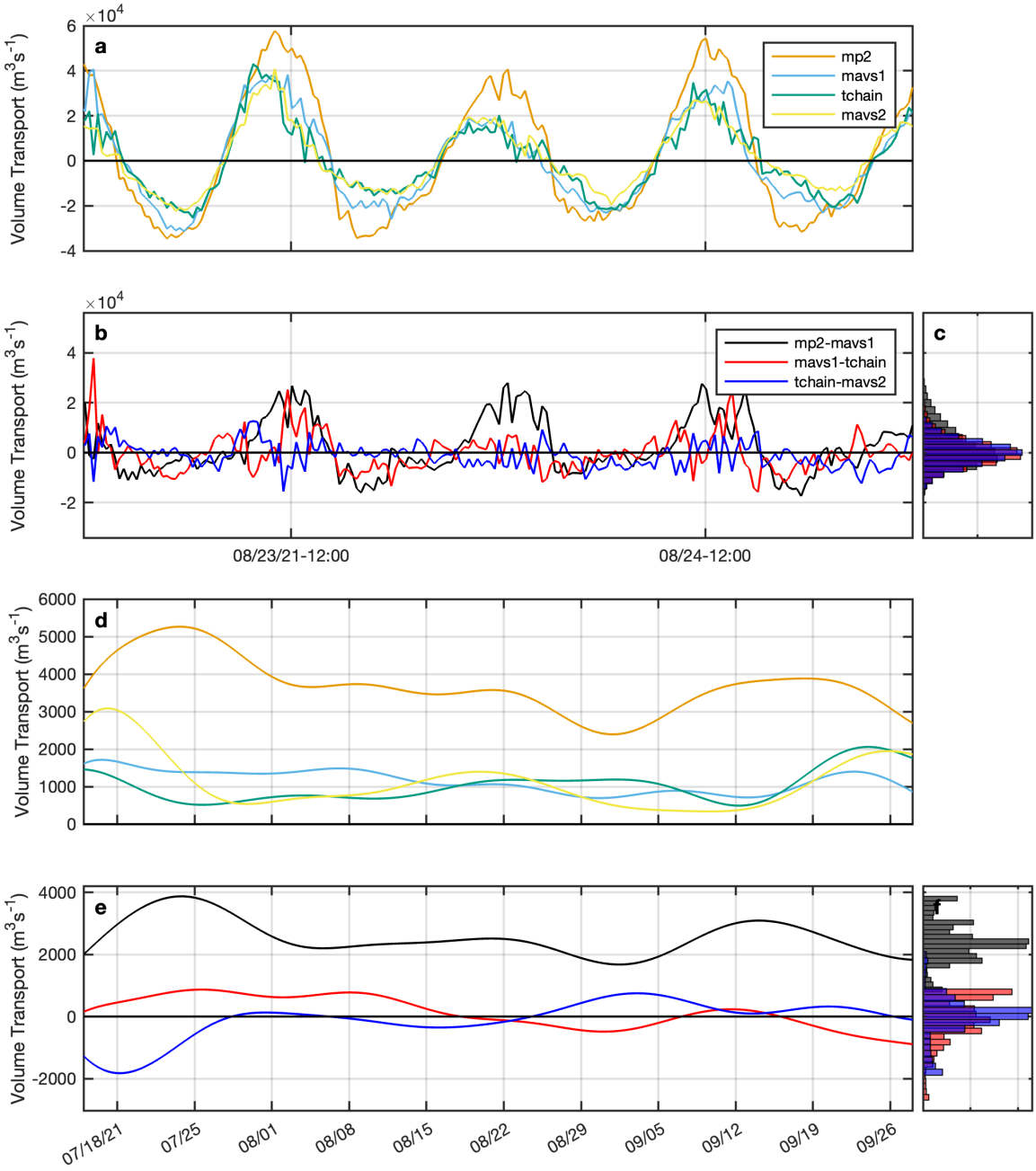

Figure 3.12. (a) 2 day period of the volume transport V_{mp2}, V_{mavs1}, V_{tchain} and V_{mavs2}. (b) The resulting volume transport out the top of the boxes ($V_{mp2-mavs1}$, $V_{mavs1-tchain}$ and $V_{tchain-mavs2}$). (c) PDF of the transport out of the boxes from the three pairs of moorings. (d,) (e) and (f) are the same as (a), (b) and (c) but for the full record low pass filtered at a period 18 days.

We again use the depth average along-canyon velocity over the bottom 200 m for the velocity at each mooring.

Similarly to the first volume analysis, a semi-diurnal tidal signal is seen in the volume transport perpendicular to the boundary (Figure 3.12). This signal is most obvious in $V_{MP2-MAVS1}$. The along-canyon transport at MP2 is approximately a factor of two larger than the transport at MAVS1 during up-canyon flow, leading to a large convergence and thus large ejection away from the boundary. The maximum negative volume transports are 2-3 times smaller than the maximum positive volume transports. The tidal cycle between MP2 and MAVS1 elicits a more symmetrical pattern than was seen previously, this is due to the magnitude of the volume transport at MP2 being larger than the transport at MAVS1 during the whole up-canyon phase of the tide. The tidal cycle in the transport perpendicular to the boundary becomes less clear as you move towards the head of the canyon. Note that although the peak transports away from the boundary region are a factor of two smaller between TCHAIN and MAVS2 than between MP2 and MAVS1, the peak transports into the boundary region are similar in magnitude all the way along the canyon.

Sub-tidal

When looking at the longer timescales, the strength of the flow at MP2 relative to the other mooring locations is clear and the volume transport is approximately 3 times larger. This means that there is always convergence between the MP2 mooring location and any other of the mooring locations. This can be seen in Figure 3.12(d), where the volume transport between MP2 and MAVS1 (black line) is always positive. Note that this transport is a factor of 2-4 times larger than was seen during the volume budget using the moorings from BLT2. Further up the canyon, low-passed transports into the interior were more similar to those seen in the 3D budget, with periods of both suction and ejection ($V_{MAVS1-TCHAIN}$ and $V_{TCHAIN-MAVS2}$; red and blue in Figure 3.12e). Over

the 3 month record, the mean of $V_{MAVS1-TCHAIN}$ is -15 m^{3}s^{-1}, and $V_{TCHAIN-MAVS2}$ is -89 m^{3}s^{-1}, in comparison to the mean of $V_{MP2-MAVS1}$ is 2.4×10^3 m^{3}s^{-1}. Therefore, in the net there is almost no suction or ejection occurring moving up the canyon relative to the most down-canyon box.

The slope of the canyon axis was approximately critical to the M2 internal tide for the duration of the record at MAVS1, while further up the canyon, the bathymetric slope increases such that at MAVS2 it was supercritical (Figure 3.13). We find that the largest transports into the interior are found where the slope is critical, consistent with previous observations that ejection is associated with critical reflection of the internal tide (McPhee-Shaw and Kunze 2002).

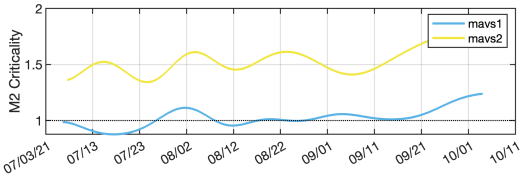

Figure 3.13. Criticality of the bathymetric slope at MAVS1 (blue) and MAVS2 (yellow) over the 3 month deployment using depth averaged stratification from the bottom 100 m of the moorings.

3.4.6 Turbulence

Using high-resolution temperature records from the thermisors on MAVS1 and MAVS2 we are able to estimate the turbulent dissipation. At both moorings, large overturning events occur periodically with the M2 internal tide (Figure 3.14). In the period shown, the stratification is unstable for approximately 4 hours during the transition from up-canyon to down-canyon flow (note that the velocities plotted in Figure 3.4.1 correspond to the time periods in Figure 3.14). Dissipation (ϵ) is enhanced up to 4 orders of magnitude above the down-canyon levels during the same time. The large scale shear induces convective instability (Naveira Garabato et al. 2024). We also see good correspondence between the Richardson number, estimated from the small

scale velocity shear and stratification, and the dissipation, suggesting that secondary instabilities within the overturn also give rise to some of the observed turbulence.

Given the strong relationship between Ri and ϵ, to investigate the time and spatial variability of the turbulence we compute the percentage of time that Richardson number is sub-critical ($Ri < 0.25$) at MAVS1 and MAVS2 over two day windows (Figure 3.15). We find that at both locations, the spring-neap variability is clear in Richardson number. At MAVS2, around day 183, the peak percentage time $Ri < 0.25$ is at a depth of ~1325 m, but this transitions to a double-peaked distribution around day 203. The peaks above the bottom are associated with layers of enhanced shear (not shown). By day 211, the peak is higher in the water column, at 1250 m. After day 213, the spring neap cycle (also seen in the velocities) dominates, with periods of less critical Ri and periods where Ri is more critical and is lowest near the bottom. Unlike at MAVS2, MAVS1 sees no peak in low Ri above the bottom. The spring neap cycle is less pronounced during the first couple of weeks but percentage of time $Ri < \frac{1}{4}$ increases towards the bottom. Note however that percentage times are higher at MAVS1 than MAVS2.

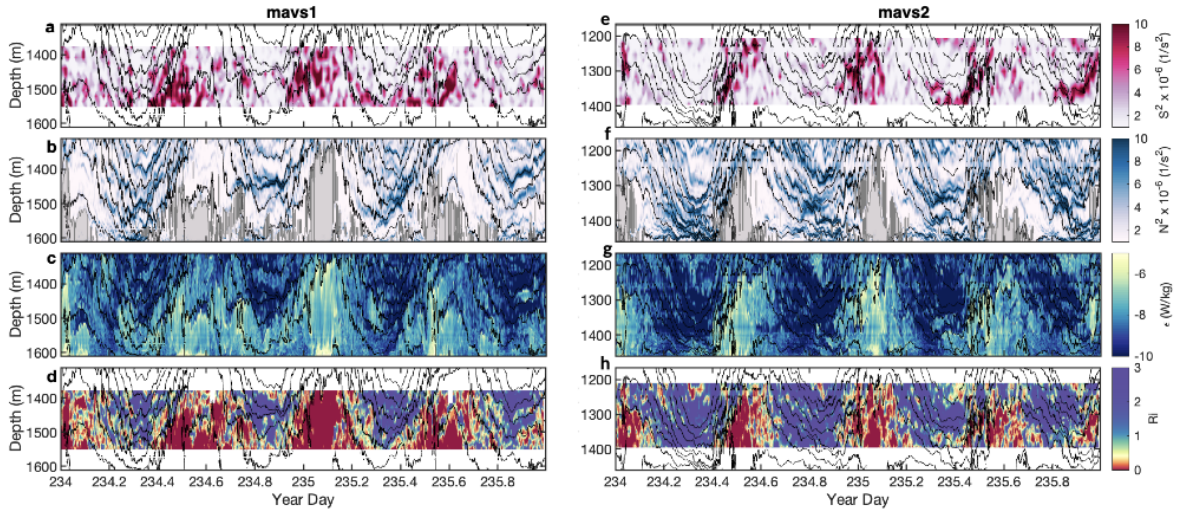

Figure 3.14. Observations from MAVS1 (left) and MAVS2 (right) over 2 days during a spring tide. (a/e) squared vertical shear (b/f) dissipation rate of turbulent kinetic energy from overturns, (c/g) stratification (shaded region indicate negative stratification) and (d/h) Richardson number.

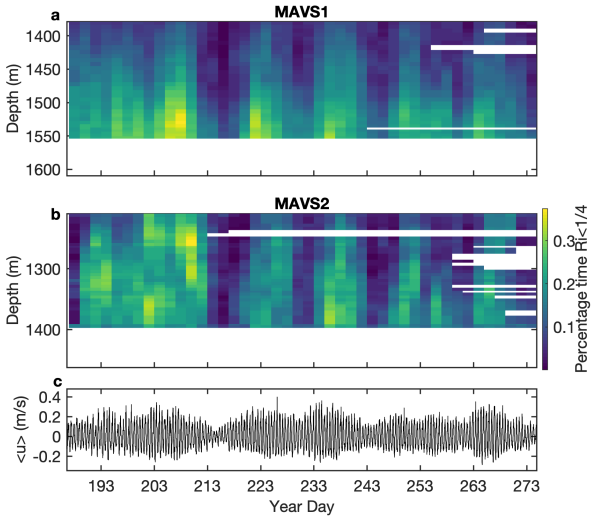

Figure 3.15. Percentage of time that Richardson number is below the critical value of 0.25, binned in periods of 2 days for (a) MAVS1 and (b) MAVS2. (c) Depth averaged along canyon velocity at MAVS1.

3.4.7 Buoyancy flux due to advection

The along canyon temperature gradient was estimated between the pairs of moorings. At each height above bottom, temperature increases along the canyon (Figure 3.16). Applying the observed temperature gradient and along-canyon velocity to Equation 3.7, we estimate the buoyancy flux due to advection at MAVS1 and MAVS2 (Figure 3.17). For turbulence generated by convective instability, the dissipation rate of turbulent kinetic energy will be equal to the buoyancy flux. This follows from $J_b = \Gamma\epsilon$ (Osborn 1980) where Γ is the mixing coefficient and is equal to 1 for purely convective instabilities.

At MAVS1, the buoyancy flux estimated within the bottom 100 m was positive during upcanyon flow and was similar in magnitude to the average turbulent dissipation rate in that depth range, suggestive of convective. The buoyancy flux and dissipation peak during the period of unstable stratification (Figure 3.17), however maximum dissipation lags the maximum buoyancy flux by approximately $\frac{\pi}{3}$, which is equivalent

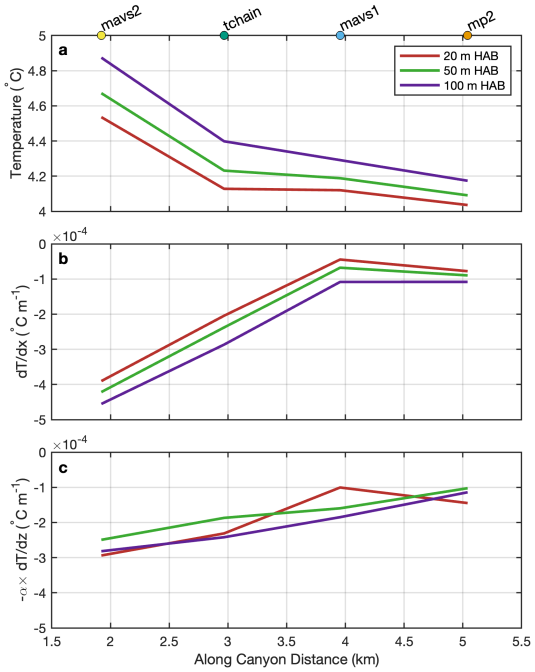

Figure 3.16. (a) Temperature 20, 50 and 100 m above bottom at the four along-canyon moorings (b) Horizontal temperature gradient between each pair of moorings (c) Vertical temperature gradient rotated to the horizontal using the bathymetric slope (α) between each pair of moorings.

to a time lag of 2 hours. This corresponds to the buoyancy period at this phase of the tide, consistent with convection. The buoyancy flux measured here is 3 orders of magnitude larger than that measured by Lorke et al. 2005 in a lake and almost orders of magnitude larger than measured by Moum et al. 2004 on the continental shelf. The buoyancy flux within a lake is expected to be smaller due to the thermal expansion of seawater. The advective velocities observed here are 8 times larger than observed by Moum et al. 2004, leading to the increased buoyancy flux. At MAVS2, the buoyancy flux estimated is a factor of 6 larger than the observed dissipation, while the reason for this is currently unclear it may be because the mixing is occurring further up the canyon.

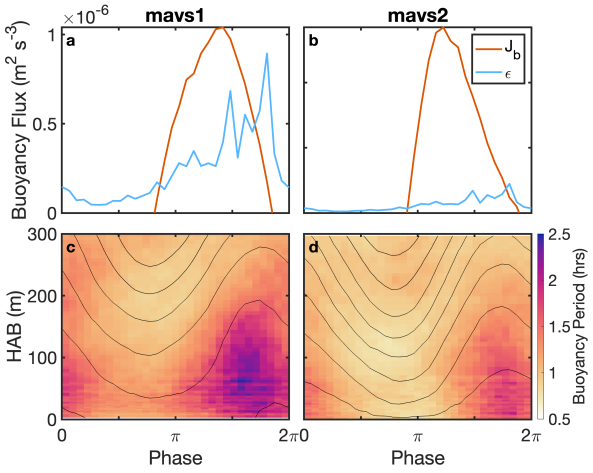

Figure 3.17. Buoyancy flux estimated from the differential advection of temperature at MAVS1 (a) and MAVS2(b) (orange) within 100 m of the bottom compared to the dissipation rate of turbulent kinetic energy averaged in the bottom 100 m (blue). (c) and (d) show the phase averaged buoyancy period at MAVS1 and MAVS2.

3.5 Summary and conclusions

In this study, observations of velocity and temperature from seven moorings in a near-critical submarine canyon were used to investigate boundary layer exchange and turbulent processes. A 3-dimensional volume budget was constructed using four of the moorings, two deployed along the axis of the canyon and two on side walls of the canyon. We found that exchange of boundary and interior fluid occurred periodically with the semi-diurnal internal tide, allowing for the boundary to be re-stratified each tidal cycle. The convergence and divergence necessary to produce the transport in and out of the interior primarily came from phase differences in the along-canyon direction that may be consistent with propagating mode 1 internal tide. A low-pass filter at a period of 18 days was applied to the transports to investigate the variability at frequencies lower than the tides and spring-neap cycle. We find that conditions at the location of the cross-canyon mooring array vary from periods of net ejection to periods of net suction. However, over the entire 6 month record we find net ejection into the interior. Given the dominance of the along-canyon transport in the volume

budget, we extended the analysis to the along-canyon mooring array which spanned a 3km section of the canyon and allowed us to investigate along-canyon variability in the transport in and out of the near-boundary region. The transport at the deepest mooring exceeded that of the shallower moorings by a factor of 2-4 and led net ejection into the interior at all times. The transport out of the boundary region estimated from the shallower volumes varied from ejection to suction as was seen at in the 3D budget and net transport over the record was near-zero. This may be consistent with locations of critical reflection of the internal tides leading to ejection, while at the super-critical locations little to no ejection was seen on average.

Turbulent dissipation within the canyon was associated with large overturning events characterised by low or negative stratification and enhanced shear. While the mechanism for inducing the large-scale overturn is hypothesised to be the advection of dense water over light by the large-scale shearing of the internal tide, the good agreement between Richardson number and dissipation rate suggests that small-scale shear within the overturn may contribute to the observed dissipation. At the critical location, we observed enhanced mixing which was consistent with convective breaking of the internal tide. At the supercritical location, we also observed periods where dissipation was elevated above the bottom associated with critical Richardson numbers. This may be indicative of shear induced by the back-reflection of the incident internal tide at the super-critical slopes.

Our observations provide additional evidence of the three-dimensional nature of the near-boundary processes within this canyon (Wynne-Cattanach et al. 2023). Together with other studies within canyons which observed similar processes, this work highlights the need to extend models of near-bottom processes to three-dimensions. Understanding and correctly parametrising the physics of processes leading to mixing and exchange with the interior is important for our modelling the impact of topographic mixing on the large-scale circulation of heat and tracers such as nutrients and carbon

dioxide.

3.6 Acknowledgements

Chapter 3, in part, is currently being prepared for submission for publication of the material. Wynne-Cattanach, Bethan L., Alford, Matthew H., Voet, Gunnar, Le Boyer, Arnaud, Couto, Nicole, Naveira Garabato, Alberto, Spingys, Carl P., Polzin, Kurt L. and van Haren, Hans. The dissertation author was the primary investigator and author of this material.

Appendix A

Supplemental figures for Chapter 1

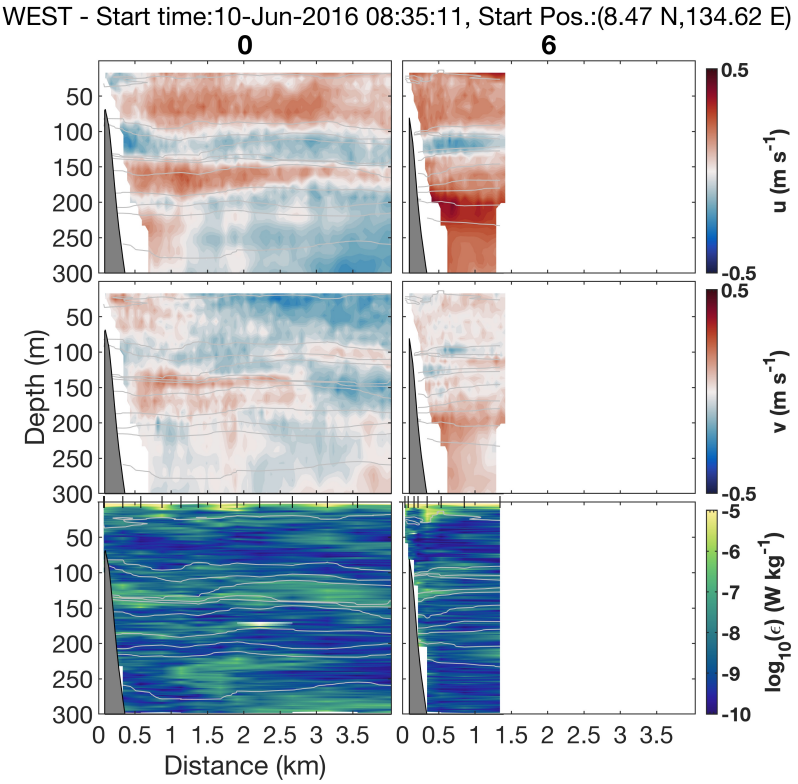

Figure A.1. Time series of (from top to bottom) meridional velocity, zonal velocity, turbulent dissipation rate for all transects of the western line. Isopycnals are shown in grey, and are spaced by 0.5 kgm^{-3}. The times of the MMP casts are indicated by the notches along the top axis of the panels along the third and sixth rows. Bathymetry is shown by the dark grey patches. The number above each column indicates the hours since the beginning of the respective sampling period (West: 10 June 2016 08:35:11) and the x- axis gives the along-track distance from the starting point (West: 8.4706°N 134.6181°E). The axis width is scaled by distance

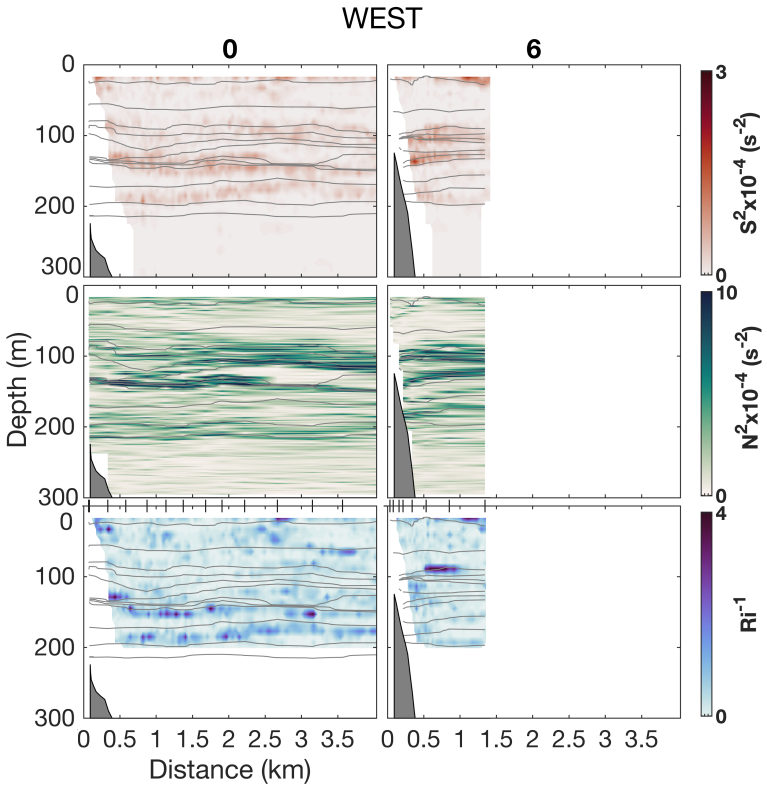

Figure A.2. Time series of (from top to bottom) squared shear, stratification and inverse Richardson number for all transects of the western line. Isopycnals are shown in grey, and are spaced by 0.5 kgm^{-3}. The times of the MMP casts are indicated by the notches along the top axis of the panels along the third and sixth rows. Bathymetry is shown by the dark grey patches. The number above each column indicates the hours since the beginning of the respective sampling period (West: 10 June 2016 08:35:11) and the x-axis gives the along-track distance from the starting point (West: 8.4706°N 134.6181°E). The axis width is scaled by distance

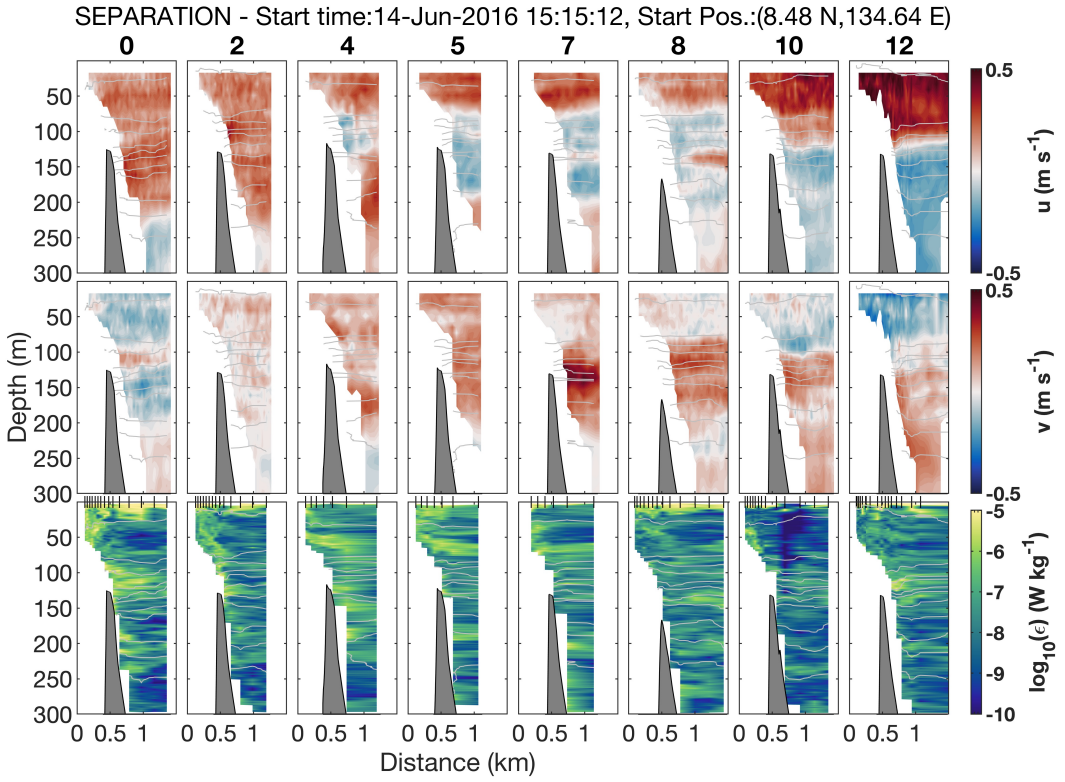

Figure A.3. Time series of (from top to bottom) meridional velocity, zonal velocity, turbulent dissipation rate for all transects of the separation line. Isopycnals are shown in grey, and are spaced by 0.5 kgm^{-3}. The times of the MMP casts are indicated by the notches along the top axis of the panels along the third and sixth rows. Bathymetry is shown by the dark grey patches. The number above each column indicates the hours since the beginning of the respective sampling period (Separation: 14 June 2016 15:15:12) and the x- axis gives the along-track distance from the starting point (Separation: 8.4749°N 134.6386°E). The axis width is scaled by distance

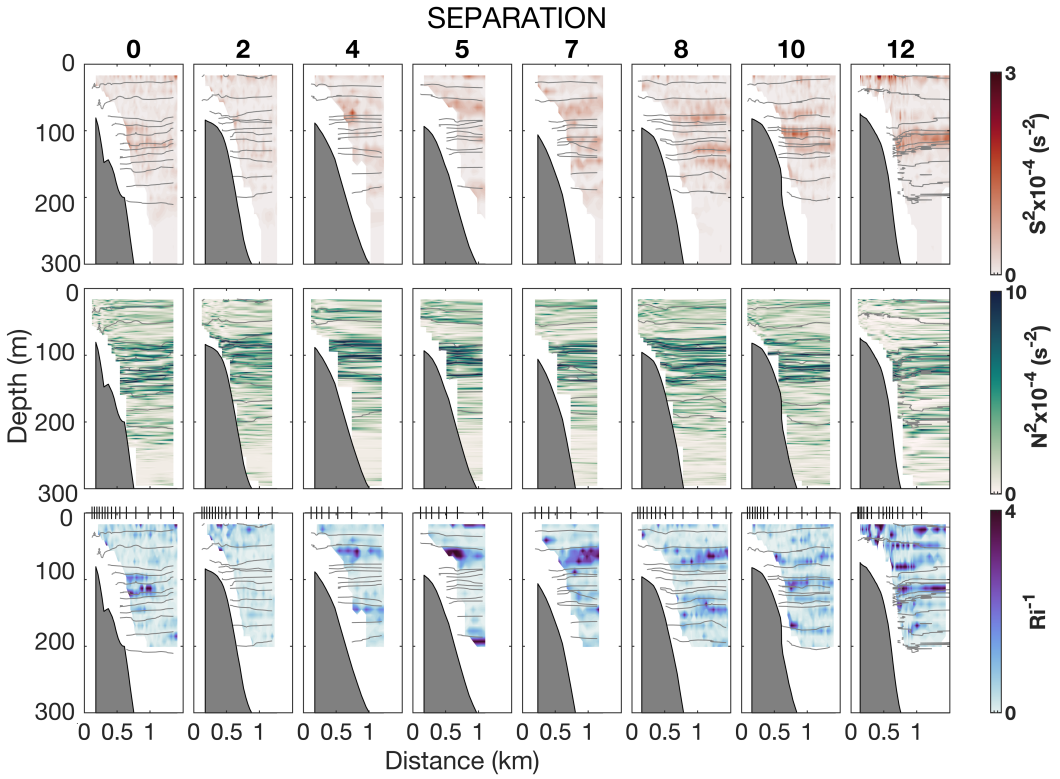

Figure A.4. Time series of (from top to bottom) squared shear, stratification and inverse Richardson number for all transects of the separation line. Isopycnals are shown in grey, and are spaced by 0.5 kgm^{-3}. The times of the MMP casts are indicated by the notches along the top axis of the panels along the third and sixth rows. Bathymetry is shown by the dark grey patches. The number above each column indicates the hours since the beginning of the respective sampling period (Separation: 14 June 2016 15:15:11) and the x- axis gives the along-track distance from the starting point (Separation: 8.4749°N 134.6386°E). The axis width is scaled by distance

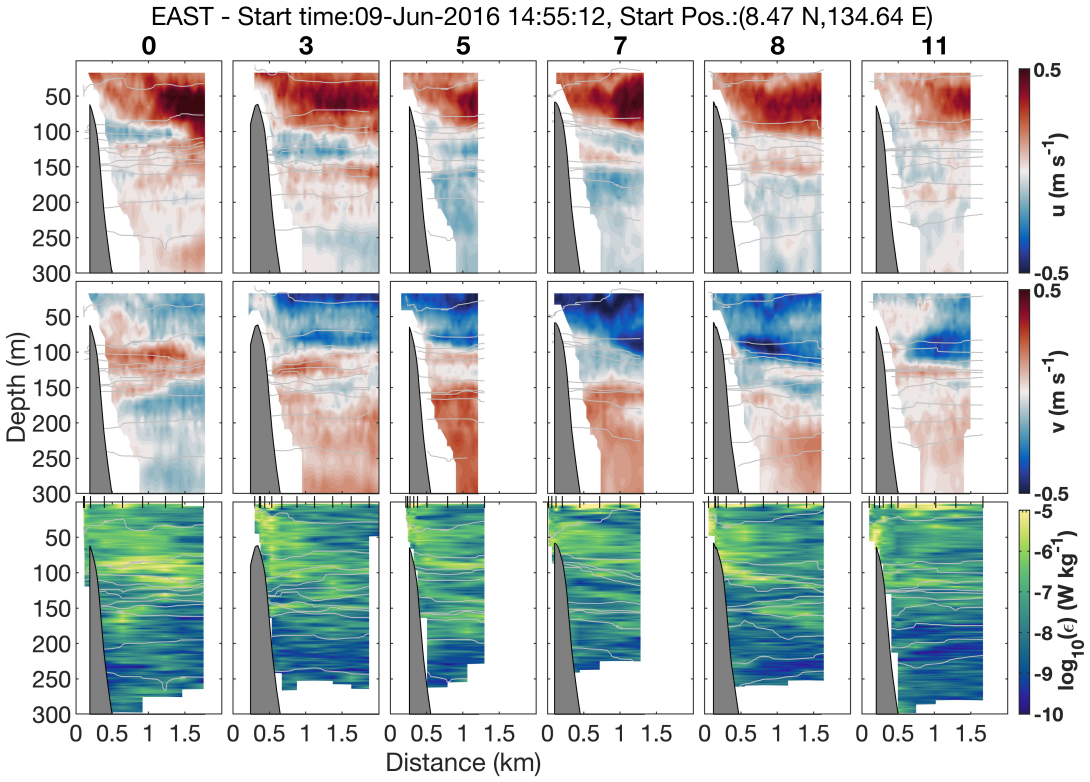

Figure A.5. Time series of (from top to bottom) meridional velocity, zonal velocity, turbulent dissipation rate for all transects of the eastern line. Isopycnals are shown in grey, and are spaced by 0.5 kgm^{-3}. The times of the MMP casts are indicated by the notches along the top axis of the panels along the third and sixth rows. Bathymetry is shown by the dark grey patches. The number above each column indicates the hours since the beginning of the respective sampling period(East: 9 June 2016 14:55:12) and the x- axis gives the along-track distance from the starting point (East: 8.47°N 134.64°E). The axis width is scaled by distance

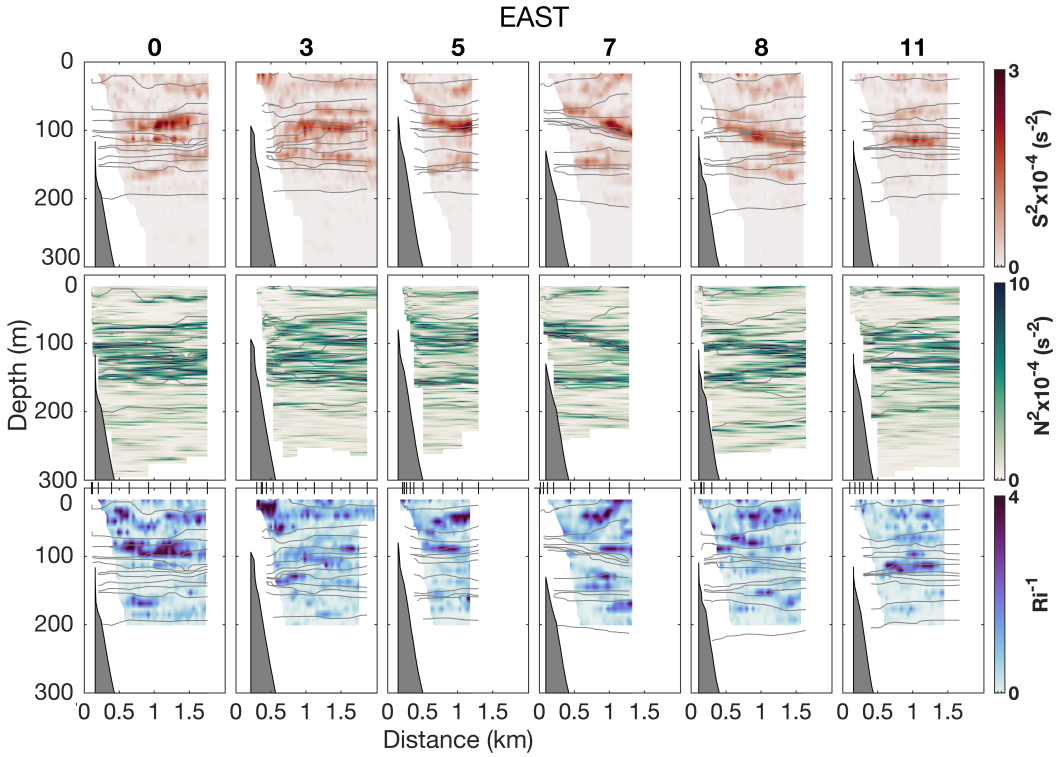

Figure A.6. Time series of (from top to bottom) squared shear, stratification and inverse Richardson number for all transects of the eastern line. Isopycnals are shown in grey, and are spaced by 0.5 kgm^{-3}. The times of the MMP casts are indicated by the notches along the top axis of the panels along the third and sixth rows. Bathymetry is shown by the dark grey patches. The number above each column indicates the hours since the beginning of the respective sampling period (East: 9 June 2016 14:55:12) and the x- axis gives the along-track distance from the starting point (East: 8.4660°N 134.6418°E). The axis width is scaled by distance

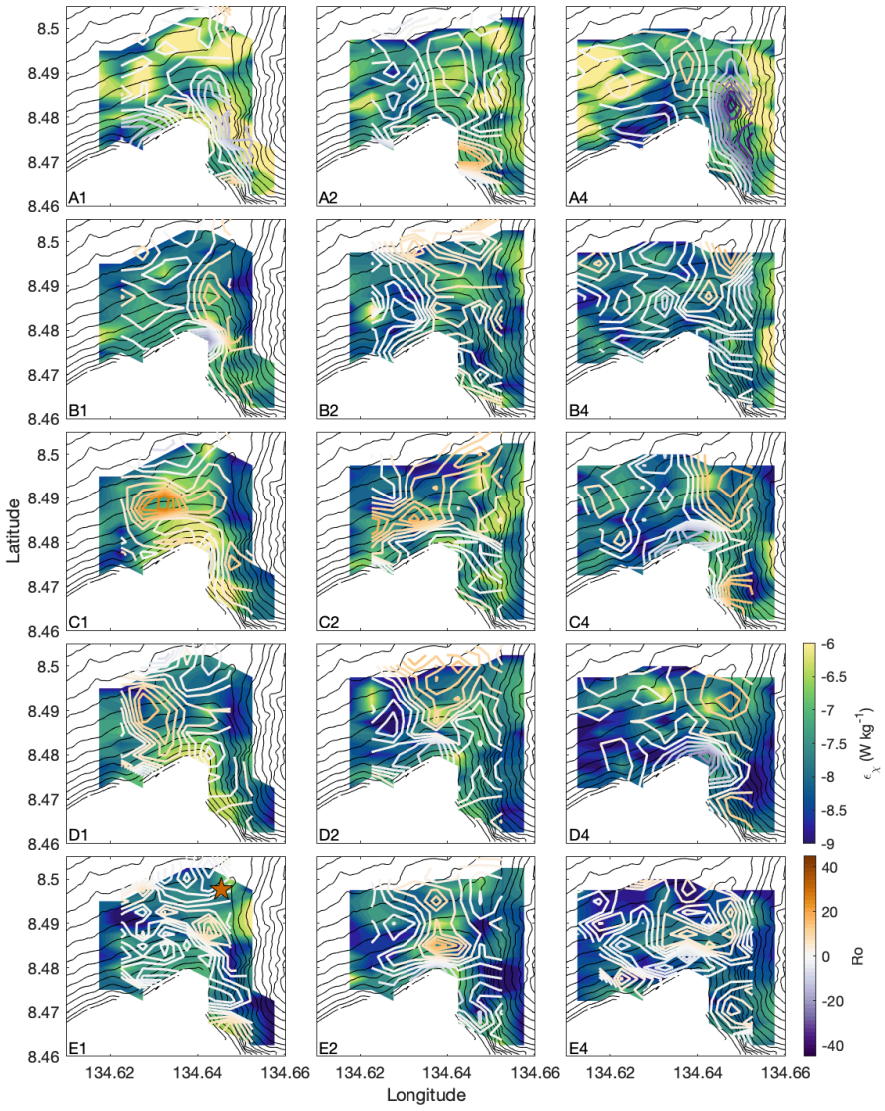

Figure A.7. FCTD surveys for passes (columns) 1, 2 and 4 conducted from east to west. Depth averages over the ranges 50-100 m (A), 100-150 m (B), 150-200 m (C), 200- 250 m (D) and 250-300 m (E) are shown in each row. In each panel the turbulent dissipation rate is shown as filled contours. The Rossby number is shown by coloured contour lines. The location of the F4 mooring is marked in panel D3 with the orange star.

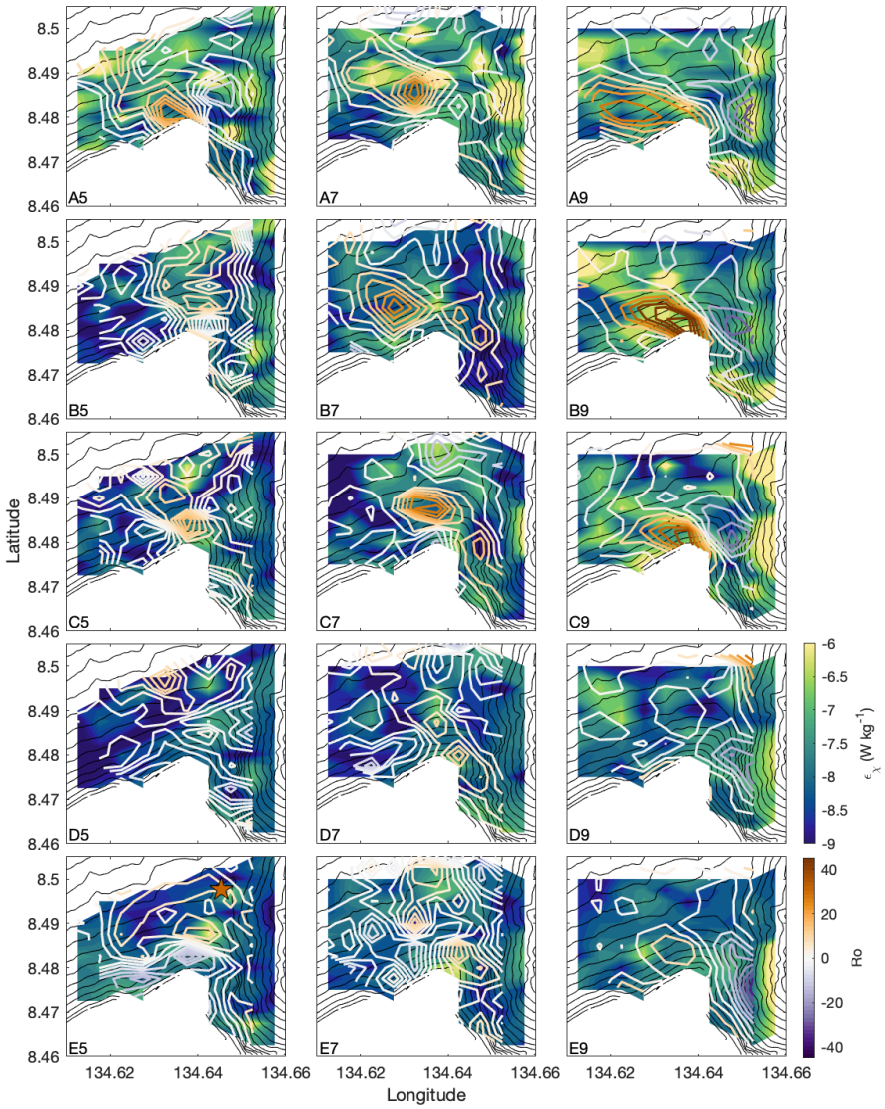

Figure A.8. FCTD surveys for passes (columns) 5, 7 and 9 conducted from east to west. Depth averages over the ranges 50-100 m (A), 100-150 m (B), 150-200 m (C), 200- 250 m (D) and 250-300 m (E) are shown in each row. In each panel the turbulent dissipation rate is shown as filled contours. The Rossby number is shown by coloured contour lines. The location of the F4 mooring is marked in panel D3 with the orange star.

Appendix B

Supplemental figures for Chapter 2

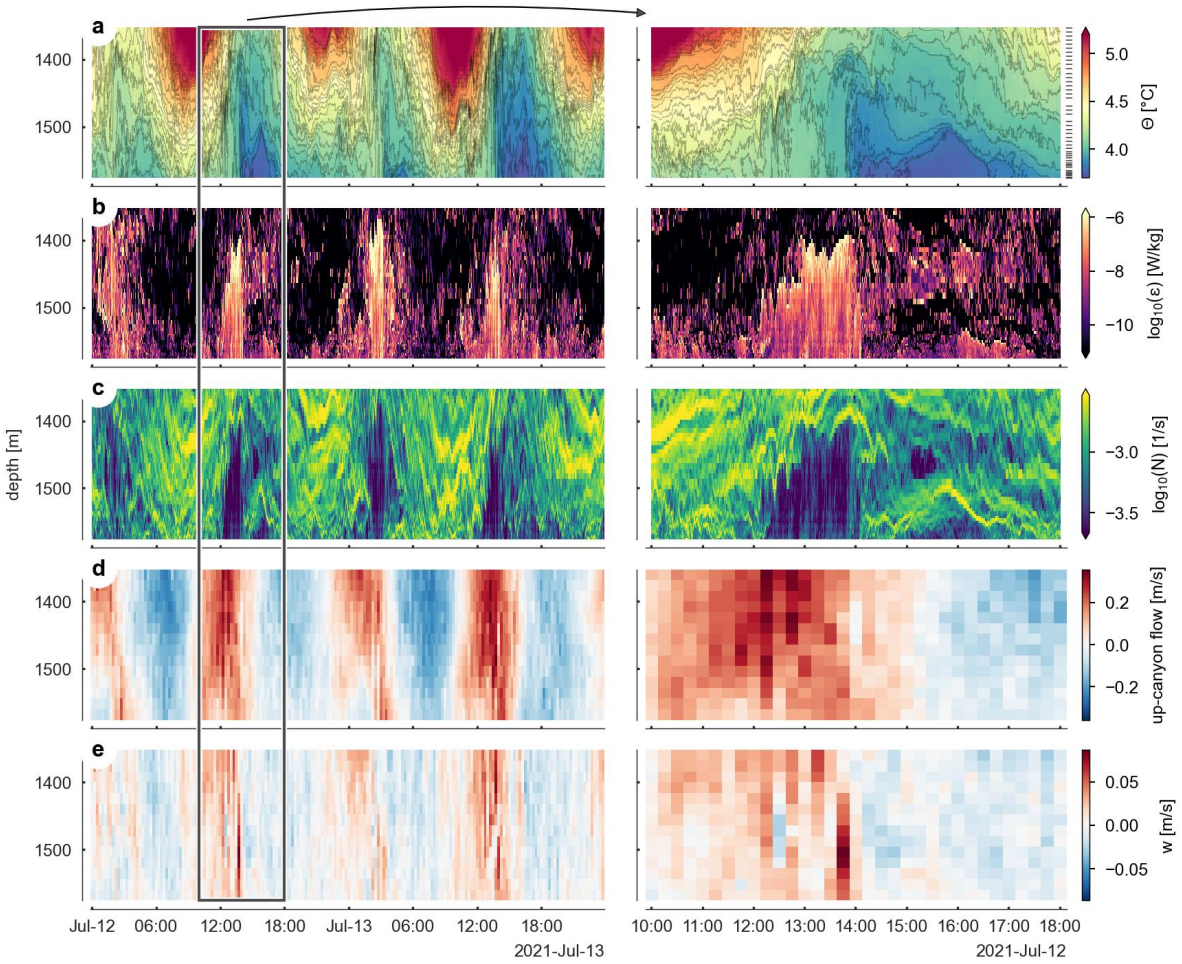

Figure B.1. (a) Temperature, (b) turbulent dissipation rate of kinetic energy (ϵ) estimated from the sorting distance when sorting profiles into stable state, (c) buoyancy frequency N calculated from the stable profile, (d) up-canyon velocity and (e) vertical velocity at the MAVS1 mooring.

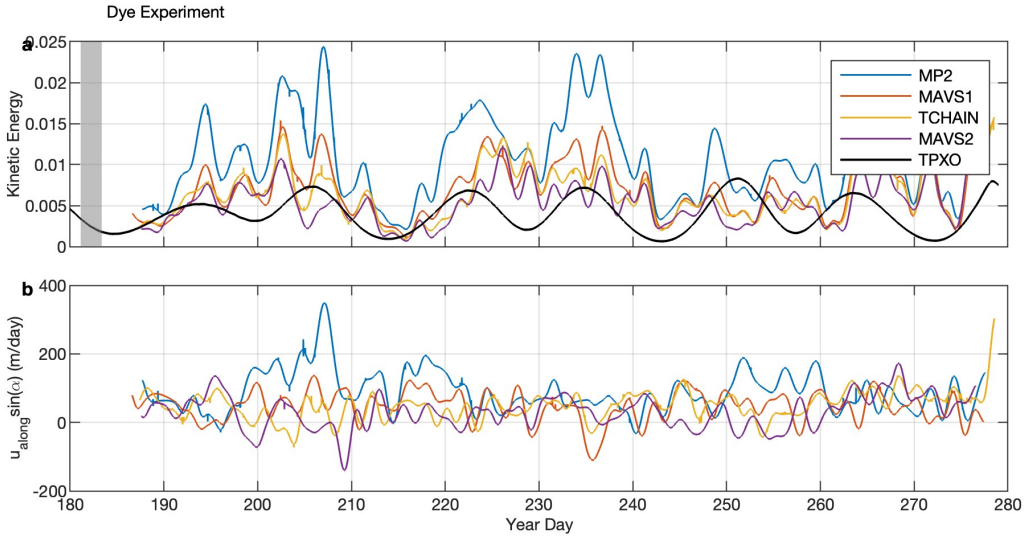

Figure B.2. (a) Kinetic energy ($\frac{1}{2}(u^2+v^2)$), low-pass filtered at a period of 48 hours, averaged over the bottom 100 m from the MP2, MAVS1, TCHAIN and MAVS2 moorings (coloured lines) and the barotropic tides estimated using TPXO. The grey shaded region shows the period covered by the dye experiment. (b) Depth average of the upwelling velocity ($u_{along}\sin\alpha$) over the bottom 100 m from the four moorings, also low-pass filtered at a period of 48 hours.

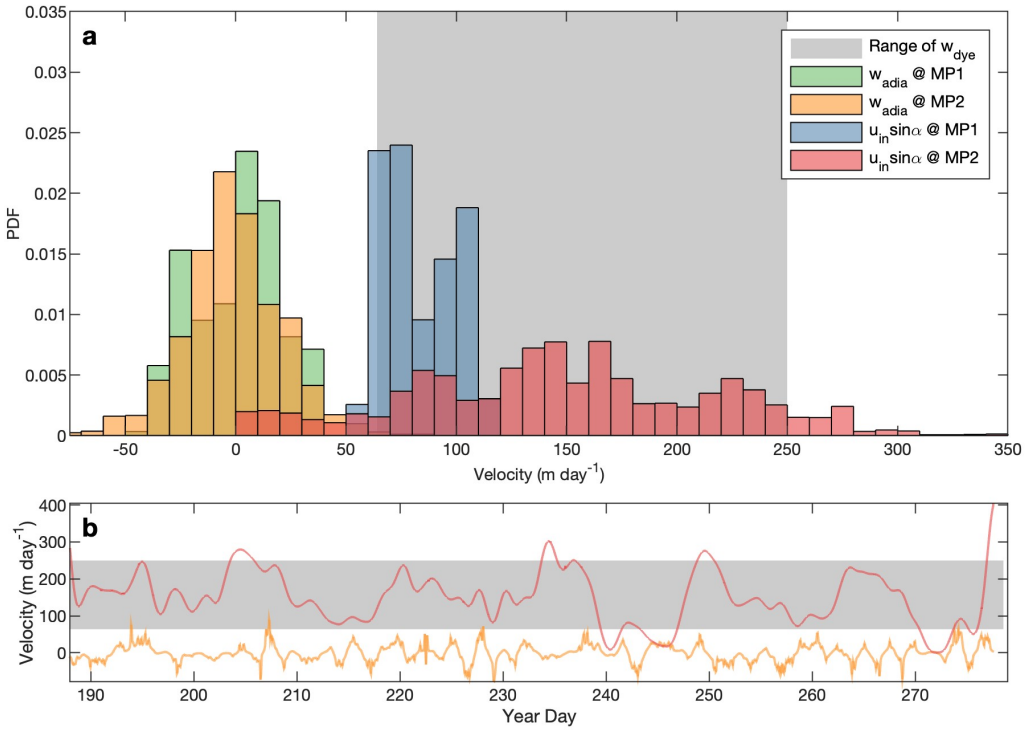

Figure B.3. (a) PDFs of the depth-averaged in-flow ($u_{in}\tan\alpha$) estimated from along-canyon velocities below 3.7°C at MP1 (blue) and below 4.2°C at MP2 (red) and the depth-averaged adiabatic vertical velocity ($w_{adia} = \frac{d\eta}{dt}$, where η is the isotherm displacement) at MP1 (green) and MP2 (orange). The range of values of w_{dye} are shown by the grey shaded region. (b) Time series of $u_{in}\tan\alpha$ (red) and w_{adia} (orange) from MP2. The range of values of w_{dye} are shown by the grey shaded region.

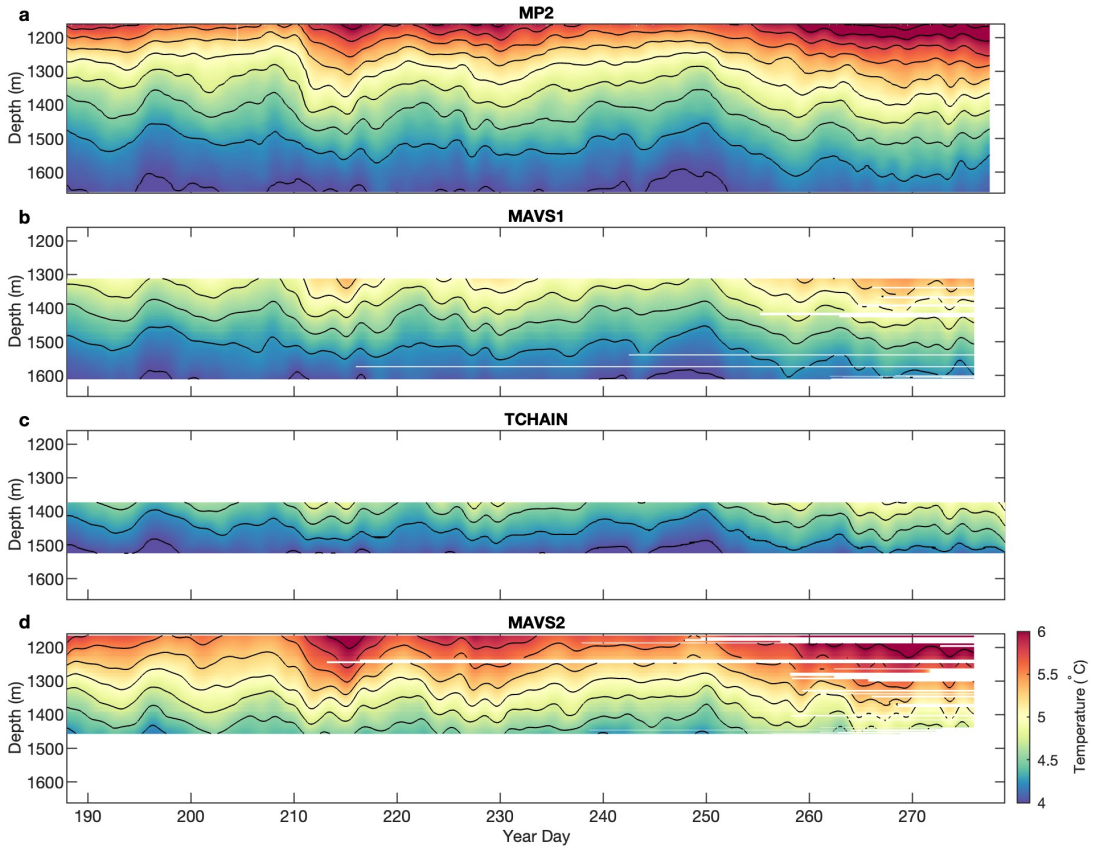

Figure B.4. Temperatures from (a) MP2, (b) MAVS1, (c) TCHAIN and (d) MAVS2 low-pass filtered at a period of 48 hours. Black contours denote isotherms are every 0.25 °C.

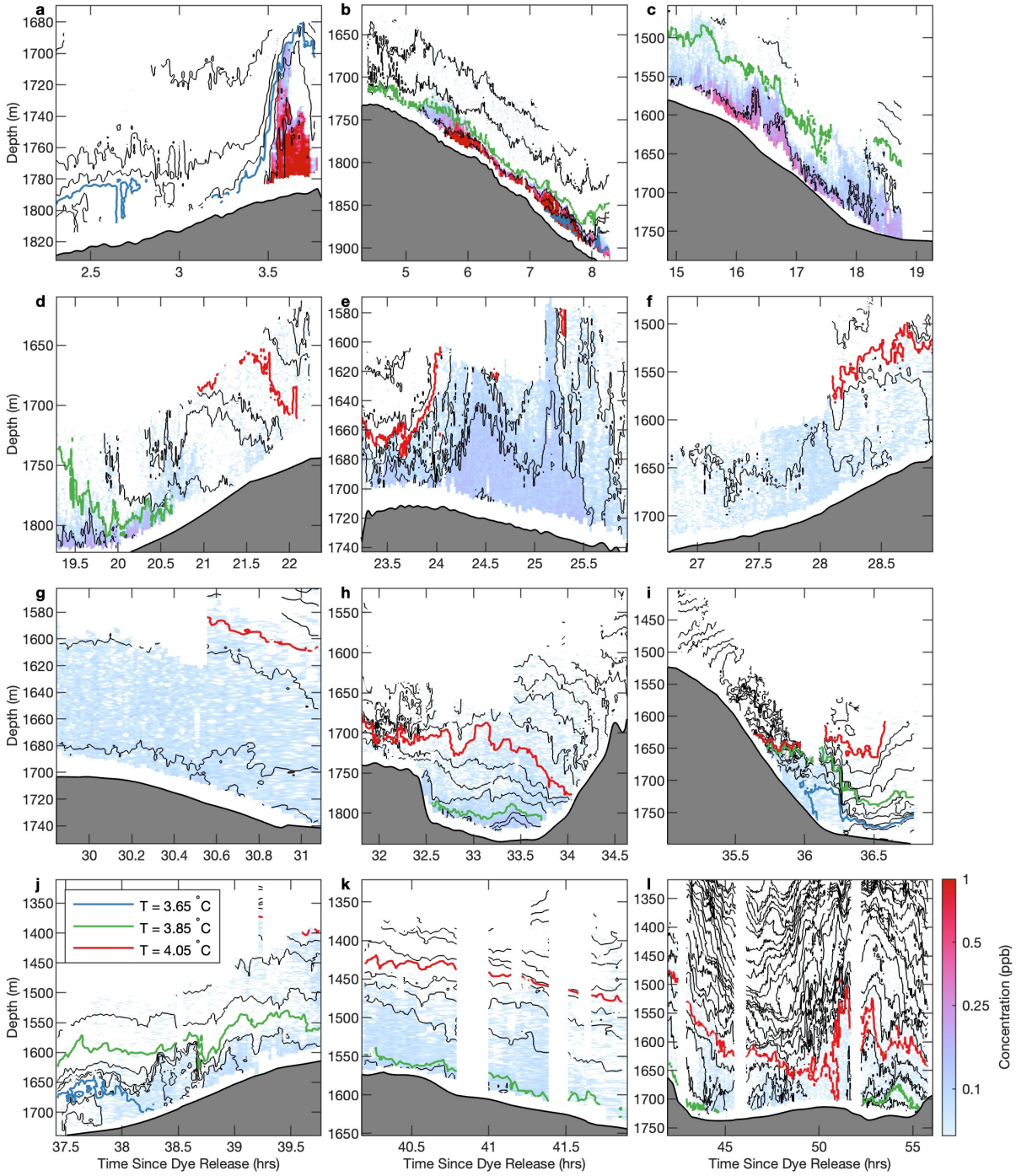

Figure B.5. (a)-(l) Dye concentration is shown on a logarithmic scale in parts per billion (ppb) in colour, isotherms every 0.05°C are shown with black contours, and 3.65°C, 3.85°C and 4.05°C isotherms are contoured in blue, green and red respectively. Note the different aspect ratios in each panel. Bathymetry is shown in grey.

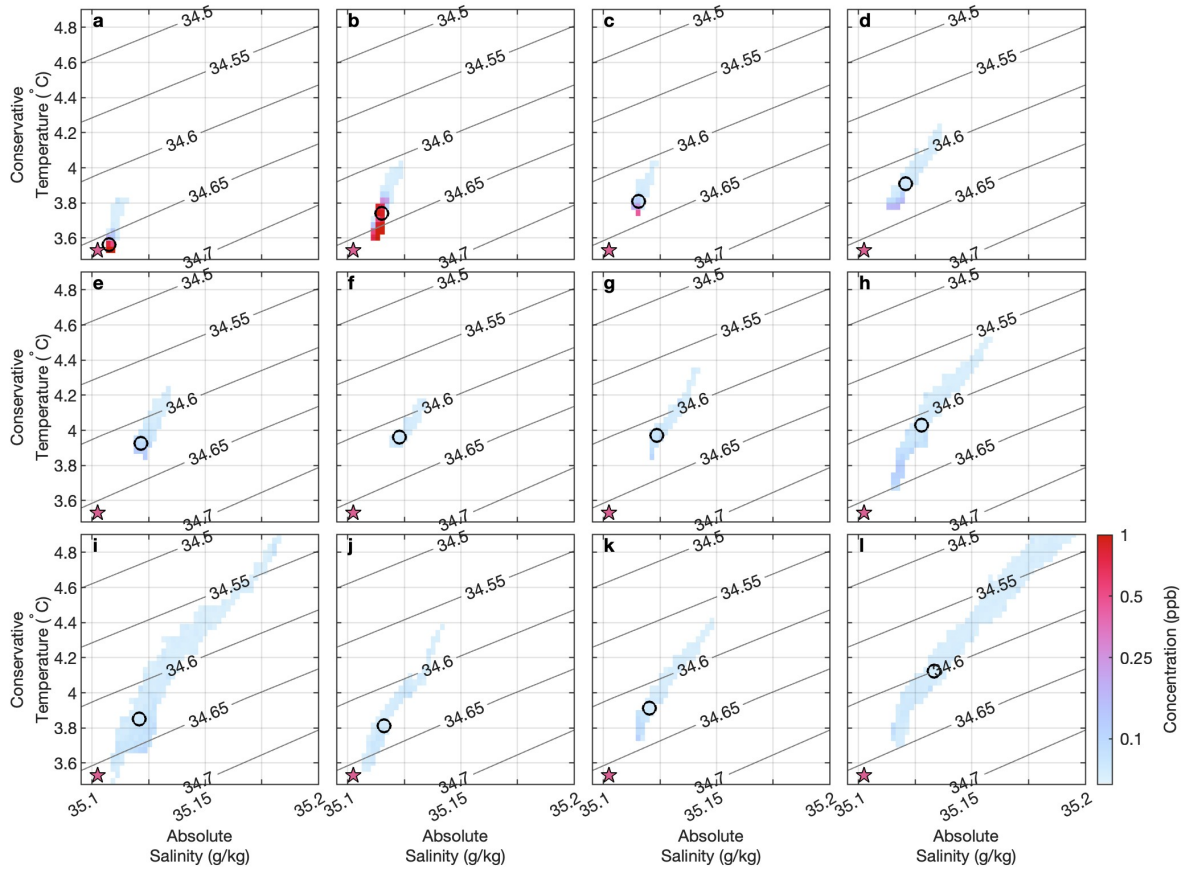

Figure B.6. For each transect ((a)-(l)), all observations are binned in conservative temperature-absolute salinity space, coloured by dye concentration. Contours of potential density anomaly are marked every 0.05 kg m^{-3}. The first tracer-weighted density moment is marked with the circle. The potential density anomaly of the dye at the time of release is marked with a pink star.

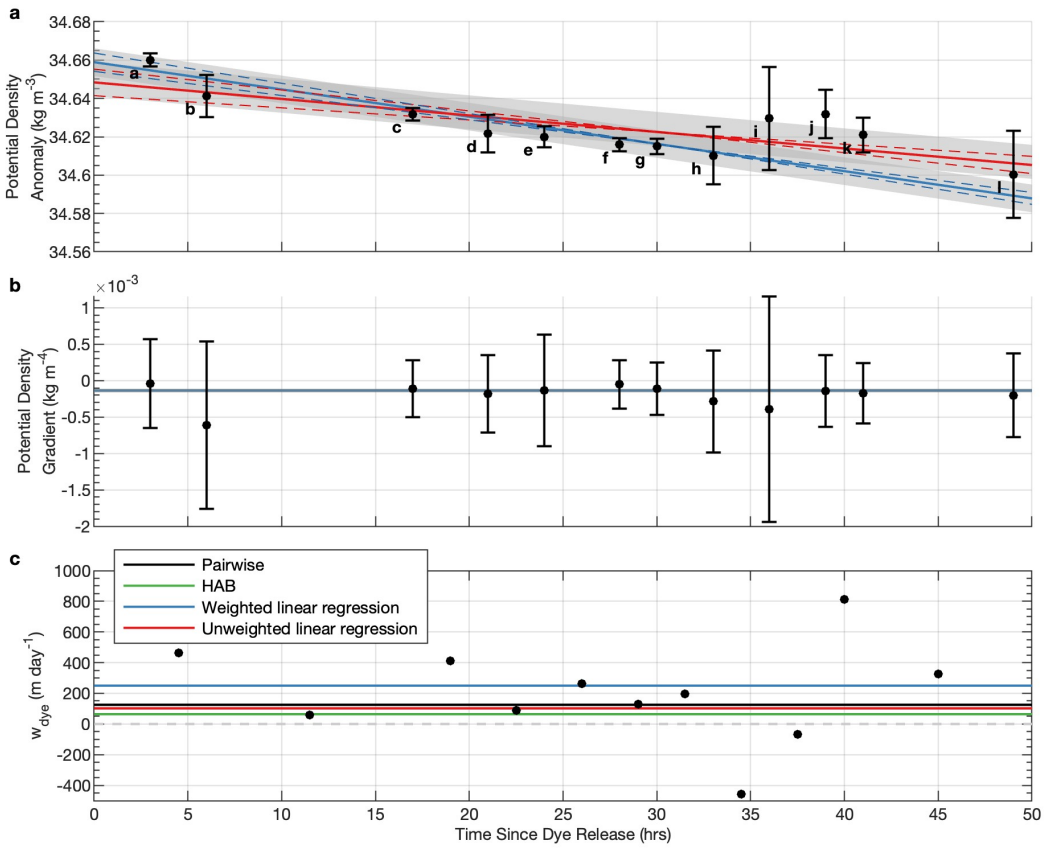

Figure B.7. (a) Weighed linear regression (solid blue line) and unweighted linear regression (solid red line) of the centres of mass in potential density anomaly space (black circles). Error bars show standard deviations of dye-weighted density for each transect. The residual standard error of the fit is denoted by the shaded region. Dashed lines show the fits given the standard error on the slope and intercept. The coefficient of determination $\mathbf{R}^2$ for the weighted fit is 0.852 and for the unweighted fit is 0.587. (b) Centres of mass in potential density anomaly gradient space (black circles) and standard deviation for each transect (error bars). The solid blue line shows the weighted average of the centres of mass. The standard error of the average is 2.5×10^{-5} kg m^{-4} and is smaller than the line width. (c) Estimates of upwelling velocity between subsequent pairs of centres of mass (black circles). Lines denote the upwelling values estimates using different methods: the weighted linear regression (blue), the unweighted linear regression (red), the difference between average height above bottom between the first and last transect (orange), the pairwise estimates in the difference between average height above bottom (green) and the average over all pairwise estimates of the upwelling velocity (black).

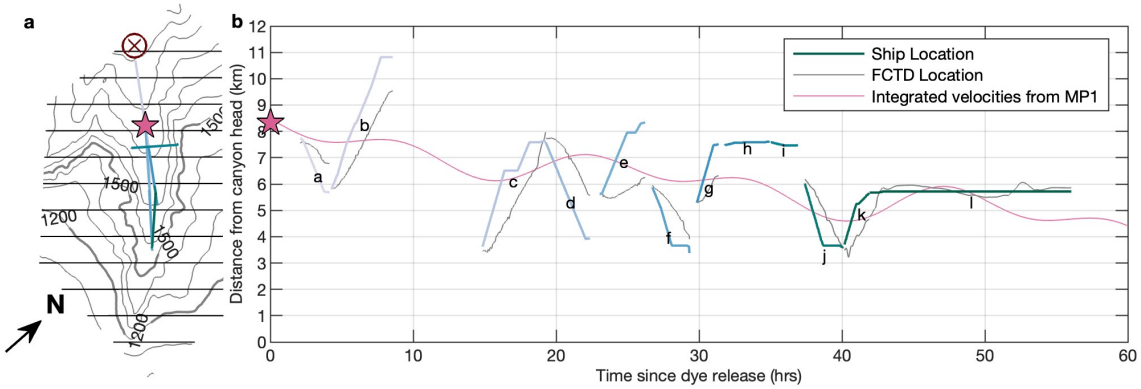

Figure B.8. (a) Map of the canyon with bathymetry contoured in grey. Horizontal lines mark the distance along the canyon in kilometres. Coloured lines correspond to the ship's location for each transect. MP1 location is marked by the red cross and the location of the dye release is marked by the pink star. Arrow indicates the direction of north. (b) Distance along the canyon of each transect over time is shown with coloured lines, which correspond to those in panel (a) and letter labels correspond to panels in Figure B.5. Thin grey lines show the approximate location of the FCTD at that time based on measured bottom depth. The pink line shows integrated velocity from the MP1 mooring, with a starting position at the dye release location (pink star) as an estimate of the along-canyon position of the dye patch.

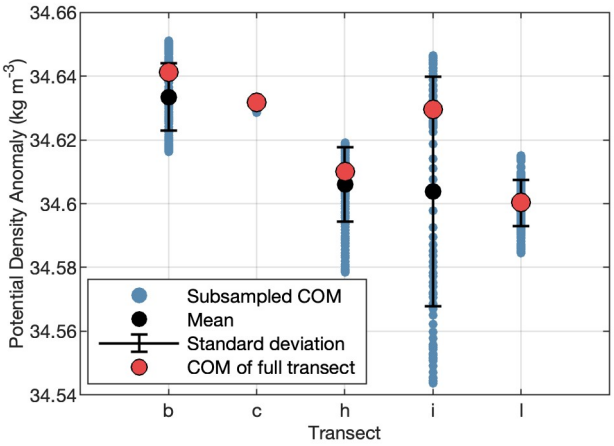

Figure B.9. Centre of mass as calculated for subsets of 10 profiles from transects b, c, h, i and l (corresponding to panels in Figure B.5). Blue dots indicate the centre of mass (COM) for each subsection, the mean of these is marked by black dots and the standard deviation around this mean is indicated by error bars. COM of the entire transect is shown in red.

Bibliography

Alberty, M. S., S. Billheimer, M. M. Hamann, C. Y. Ou, V. Tamsitt, A. J. Lucas, and M. H. Alford. 2017. "A reflecting, steepening, and breaking internal tide in a submarine canyon." *Journal of Geophysical Research: Oceans* 122:6872–6882. https://doi.org/10.1002/2016JC012583.

Alford, M. H., and Michael C. Gregg. 2001. "Near-Inertial Mixing: Modulation of Shear, Strain and Microstructure at Low Latitude." *Journal of Geophysical Research: Oceans* 106 (C8): 16947–16968. https://doi.org/10.1029/2000JC000370.

Alford, M. H., Jennifer A. MacKinnon, Jonathan D. Nash, Harper L. Simmons, Andrew Pickering, Jody M. Klymak, Robert Pinkel, Oliver Sun, Luc Rainville, Ruth Musgrave, Tamara Beitzel, Ke-Hsien Fu, and Chung-Wei Lu. 2011. "Energy Flux and Dissipation in Luzon Strait: Two Tales of Two Ridges." *Journal of Physical Oceanography* 41 (11): 2211–2222. https://doi.org/10.1175/JPO-D-11-073.1.

Alford, M. H., Thomas Peacock, Jennifer A. MacKinnon, Jonathan D. Nash, Maarten C. Buijsman, Luca R. Centurioni, Shenn-Yu Chao, Ming-Huei Chang, David M. Farmer, Oliver B. Fringer, Ke-Hsien Fu, Patrick C. Gallacher, Hans C. Graber, Karl R. Helfrich, Steven M. Jachec, Christopher R. Jackson, Jody M. Klymak, Dong S. Ko, Sen Jan, T. M. Shaun Johnston, Sonya Legg, I-Huan Lee, Ren-Chieh Lien, Matthieu J. Mercier, James N. Moum, Ruth Musgrave, Jae-Hun Park, Andrew I. Pickering, Robert Pinkel, Luc Rainville, Steven R. Ramp, Daniel L. Rudnick, Sutanu Sarkar, Alberto Scotti,

Harper L. Simmons, Louis C. St Laurent, Subhas K. Venayagamoorthy, Yu-Huai Wang, Joe Wang, Yiing J. Yang, Theresa Paluszkiewicz, and Tswen-Yung (David) Tang. 2015. "The formation and fate of internal waves in the South China Sea." *Nature* 521 (7550): 65–69. https://doi.org/10.1038/nature14399.

Alford, M. H., and Robert Pinkel. 2000a. "Observations of overturning in the thermocline: The context of ocean mixing." *Journal of Physical Oceanography* 30 (5): 805–832. https://doi.org/10.1175/1520-0485(2000)030<0805:OOOITT>2.0.CO;2.

Alford, Matthew, and Robert Pinkel. 2000b. "Patterns of Turbulent and Double-Diffusive Phenomena: Observations from a Rapid-Profiling Microconductivity Probe." *Journal of Physical Oceanography* 30 (5): 833–854. https://doi.org/10.1175/1520-0485(2000)030<0833:POTADD>2.0.CO;2.

Alford, Matthew H, and Parker MacCready. 2014. "Flow and mixing in Juan de Fuca Canyon, Washington." *Geophys. Res. Lett.* 41:1–8. https://doi.org/10.1002/2013GL058967.

Alford, Matthew H. 2003. "Redistribution of Energy Available for Ocean Mixing by Long-Range Propagation of Internal Waves." *Nature* 423 (6936): 159–162. https://doi.org/10.1038/nature01628.

Alford, Matthew H., Bethan. L. Wynne-Cattanach, Arnaud Le Boyer, Nicole Couto, Gunnar Voet, Carl P. Spingys, Bieto Fernandez Castro, Alexander Forryan, and Alberto Naveira Garabato. 2024. "Buoyancy Flux and Mixing Efficiency from Direct, near-Bottom Turbulence Measurements in a Submarine Canyon." *Journal of Physical Oceanography* Submitted.

Alford, Matthew H., and Zhongxiang Zhao. 2007. "Global Patterns of Low-Mode Internal-Wave Propagation. Part II: Group Velocity." *Journal of Physical Oceanography* 37 (7): 1849–1858. https://doi.org/10.1175/JPO3086.1.

Allen, S. E., and X. Durrieu de Madron. 2009. "A Review of the Role of Submarine Canyons in Deep-Ocean Exchange with the Shelf." *Ocean Science* 5 (4): 607–620. https://doi.org/10.5194/os-5-607-2009.

Armi, L. 1978. "Some evidence for boundary mixing in the deep ocean." *Journal of Geophysical Research* 83 (C4): 1971–1979. https://doi.org/10.1029/JC083iC04p01971.

Armi, Laurence. 1979. "Reply to Comments by C. Garrett." *Journal of Geophysical Research* 84 (C8): 5097–5098. https://doi.org/10.1029/JC084iC08p05097.

Aucan, Jerome, Mark A. Merrifield, Douglas S. Luther, and Pierre Flament. 2006. "Tidal Mixing Events on the Deep Flanks of Kaena Ridge, Hawaii." *Journal of Physical Oceanography* 36 (6): 1202–1219. https://doi.org/10.1175/JPO2888.1.

Bell Jr., T. H. 1975. "Topographically Generated Internal Waves in the Open Ocean." *Journal of Geophysical Research (1896-1977)* 80 (3): 320–327. https://doi.org/10.1029/JC080i003p00320.

Boulanger, Nicolas, Patrice Meunir, and Stéphane le Dizès. 2007. "Structure of a stratified tilted vortex." *Journal of Fluid Mechanics* 583:443–458. https://doi.org/10.1017/S0022112007006416.

Brink, K. H. 2016. "Cross-Shelf Exchange." *Annual Review of Marine Science* 8 (1): 59–78. https://doi.org/10.1146/annurev-marine-010814-015717.

Canals, Miguel, Geno Pawlak, and Parker MacCready. 2009. "Tilted Baroclinic Tidal Vortices." *Journal of Physical Oceanography* 39 (2): 333–350. https://doi.org/10.1175/2008JPO3954.1.

Carter, G S, M. C. Gregg, and M. A. Merrifield. 2006. "Flow and Mixing around a Small Seamount on Kaena Ridge, Hawaii." *Journal of Physical Oceanography* 36 (6): 1036–1052. https://doi.org/10.1175/JPO2924.1.

Carter, Glenn S., and Michael C. Gregg. 2002. "Intense, Variable Mixing near the Head of Monterey Submarine Canyon." *Journal of Physical Oceanography* 32 (11): 3145–3165. https://doi.org/10.1175/1520-0485(2002)032<3145:IVMNTH>2.0.CO;2.

Chalamalla, Vamsi K., and Sutanu Sarkar. 2015. "Mixing, Dissipation Rate, and Their Overturn-Based Estimates in a Near-Bottom Turbulent Flow Driven by Internal Tides." *Journal of Physical Oceanography* 45 (8): 1969–1987.

Chang, Ming-Huei, Tswen Yung Tang, Chung-Ru Ho, and Shenn-Yu Chao. 2013. "Kuroshio-induced wake in the lee of Green Island off Taiwan." *Journal of Geophysical Research: Oceans* 118 (3): 1508–1519. https://doi.org/10.1002/jgrc.20151.

Cimoli, Laura, Colm-cille P. Caulfield, Helen L. Johnson, David P. Marshall, Ali Mashayek, Alberto C. Naveira Garabato, and Clément Vic. 2019. "Sensitivity of Deep Ocean Mixing to Local Internal Tide Breaking and Mixing Efficiency." *Geophysical Research Letters* 46 (24): 14622–14633. https://doi.org/10.1029/2019GL085056.

Cimoli, Laura, Ali Mashayek, Helen L Johnson, David P Marshall, Alberto C Naveira Garabato, Caitlin B Whalen, Clément Vic, Casimir de Lavergne, Matthew H Alford, Jennifer A MacKinnon, et al. 2023. "Significance of Diapycnal Mixing within the Atlantic Meridional Overturning Circulation." *AGU Advances* 4 (2): e2022AV000800. https://doi.org/10.1029/2022AV000800.

Clark, David B., Luc Lenain, Falk Feddersen, Emmanuel Boss, and R. T. Guza. 2014. "Aerial Imaging of Fluorescent Dye in the Near Shore." *Journal of Atmospheric and Oceanic Technology* 31 (6): 1410–1421. https://doi.org/10.1175/JTECH-D-13-00230.1.

Couchman, Miles M. P., Bethan Wynne-Cattanach, Matthew H. Alford, Colm-cille P. Caulfield, Rich R. Kerswell, Jennifer A. MacKinnon, and Gunnar Voet. 2021. "Data-Driven Identification of Turbulent Oceanic Mixing From Observational Microstructure Data." *Geophysical Research Letters* 48 (23). https://doi.org/10.1029/2021GL094978.

De Lavergne, Casimir, Gurvan Madec, Julien Le Sommer, AJ George Nurser, and Alberto C Naveira Garabato. 2016. "The Impact of a Variable Mixing Efficiency on the Abyssal Overturning." *Journal of Physical Oceanography* 46 (2): 663–681. https://doi.org/10.1175/JPO-D-14-0259.1.

De Lavergne, Casimir, Gurvan Madec, Julien Le Sommer, AJ George Nurser, and Alberto C Naveira Garabato. 2016. "On the consumption of Antarctic Bottom Water in the abyssal ocean." *Journal of Physical Oceanography* 46 (2): 635–661. https://doi.org/10.1175/JPO-D-14-0201.1.

Deleersnijder, Eric, Alain Norro, and Eric Wolanski. 1992. "A Three-Dimensional Model of the Water Circulation around an Island in Shallow Water." *Continental Shelf Research* 12 (7-8): 891–906. https://doi.org/10.1016/0278-4343(92)90050-T.

Drake, Henri F., Raffaele Ferrari, and Jörn Callies. 2020. "Abyssal Circulation Driven by Near-Boundary Mixing: Water Mass Transformations and Interior Stratification." *Journal of Physical Oceanography* 50 (8): 2203–2226. https://doi.org/10.1175/JPO-D-19-0313.1.

Drake, Henri F., Xiaozhou Ruan, and Raffaele Ferrari. 2022. "Diapycnal motion, diffusion, and stretching of purposefully released tracers above rough topography." *Journal of Physical Oceanography*, no. 52, 3221–3240. https://doi.org/10.1175/JPO-D-22-0010.1.

Edwards, Kathleen A., Parker MacCready, James N. Moum, Geno Pawlak, Jody M. Klymak, and Alexander Perlin. 2004. "Form Drag and Mixing Due to Tidal Flow Past a Sharp Point." *Journal of Physical Oceanography* 34 (6): 1297–1312. https://doi.org/10.1175/1520-0485(2004)034%3C1297:FDAMDT%3E2.0.CO;2.

Egbert, Gary D, and Richard D Ray. 2000. "Significant Dissipation of Tidal Energy in the Deep Ocean Inferred from Satellite Altimeter Data." *Nature* 405 (6788): 775–778. https://doi.org/10.1038/35015531.

Farmer, D., R. Pawlowicz, and R. Jiang. 2002. "Tilting separation flows: a mechanism for intense vertical mixing in the coastal ocean." Ocean Fronts, *Dynamics of Atmospheres and Oceans* 36 (1): 43–58. https://doi.org/10.1016/S0377-0265(02)00024-6.

Ferrari, Raffaele, Ali Mashayek, Trevor J. McDougall, Maxim Nikurashin, and Jean Michael Campin. 2016. "Turning ocean mixing upside down." Publisher: American Meteorological Society, *Journal of Physical Oceanography* 46 (7): 2239–2261. https://doi.org/10.1175/JPO-D-15-0244.1.

Garrett, C. 1979. "Comment on 'Some Evidence for Boundary Mixing in the Deep Ocean'." *Journal of Geophysical Research* 84:5095. https://doi.org/10.1029/JC084iC08p05095.

Garrett, Chris. 1990. "The Role of Secondary Circulation in Boundary Mixing." *Journal of Geophysical Research: Oceans* 95 (C3): 3181–3188. https://doi.org/10.1029/JC095iC03p03181.

Garrett, Chris. 2001. "An Isopycnal View of Near-Boundary Mixing and Associated Flows." *Journal of Physical Oceanography* 31 (1): 138–142. https://doi.org/10.1175/1520-0485(2001)031<0138:AIVONB>2.0.CO;2.

Geyer, W Rockwell, and Richard Signell. 1990. "Measurements of tidal flow around a headland with a shipboard acoustic Doppler current profiler." *Journal of Geophysical Research: Oceans* 95 (C3): 3189–3197. https://doi.org/10.1029/JC095iC03p03189.

Geyer, W. R., A. C. Lavery, M. E. Scully, and J. H. Trowbridge. 2010. "Mixing by Shear Instability at High Reynolds Number." *Geophysical Research Letters* 37 (22): n/a–n/a. https://doi.org/10.1029/2010GL045272.

Gove, Jamison M., Margaret A. McManus, Anna B. Neuheimer, Jeffrey J. Polovina, Jeffrey C. Drazen, Craig R. Smith, Mark A. Merrifield, Alan M. Friedlander, Julia S. Ehses, Charles W. Young, Amanda K. Dillon, and Gareth J. Williams. 2016. "Near-island biological hotspots in barren ocean basins." *Nature Communications* 7 (1). https://doi.org/10.1038/ncomms10581.

Gregg, M C, R. A. Hall, G. S. Carter, Matthew H. Alford, R.-C. Lien, D. P. Winkel, and D. J. Wain. 2011. "Flow and Mixing in Ascension, a Steep, Narrow Canyon." *Journal of Geophysical Research* 116 (C07016). https://doi.org/10.1029/2010JC006610.

Gregg, M. C. 1998. "Estimation and Geography of Diapycnal Mixing in the Stratified Ocean." Chap. 23 in *Physical Processes in Lakes and Oceans,* edited by J Imberger, 305–338. American Geophysical Union. https://doi.org/10.1029/CE054p0305.

Gregg, Michael C. 1989. "Scaling Turbulent Dissipation in the Thermocline." *Journal of Geophysical Research: Oceans* 94 (C7): 9686–9698. https://doi.org/10.1029/JC094iC07p09686.

Gregg, Michael C, Eric A D'Asaro, James J Riley, and Eric Kunze. 2018. "Mixing efficiency in the ocean." *Annual review of marine science* 10:443–473. https://doi.org/10.1146/annurev-marine-121916-063643.

Haine, Thomas W. N., and John Marshall. 1998. "Gravitational, Symmetric, and Baroclinic Instability of the Ocean Mixed Layer." *Journal of Physical Oceanography* 28 (4): 634–658. https://doi.org/10.1175/1520-0485(1998)028<0634:GSABIO>2.0.CO;2.

Hamann, Madeleine M., Matthew H. Alford, Andrew J. Lucas, and Amy F. Waterhouse. 2019. "Reflected internal tides in a shelf-incising submarine canyon: dynamics, turbulence, and context." https://doi.org/10.1175/JPO-D-20-0123.1.

Hamann, Madeleine M., Matthew H. Alford, Andrew J. Lucas, Amy F. Waterhouse, and Gunnar Voet. 2021. "Turbulence Driven by Reflected Internal Tides in a Supercritical Submarine Canyon." *Journal of Physical Oceanography* 51 (2): 591–609. https://doi.org/10.1175/JPO-D-20-0123.1.

Hamann, Madeleine M., Matthew H. Alford, and John B. Mickett. 2018. "Generation and Propagation of Nonlinear Internal Waves in Sheared Currents Over the Washington Continental Shelf." *Journal of Geophysical Research: Oceans* 123 (4): 2381–2400. https://doi.org/10.1002/2017JC013388.

Harris, P. T., M. Macmillan-Lawler, J. Rupp, and E. K. Baker. 2014. "Geomorphology of the Oceans." *Marine Geology* 352:4–24. https://doi.org/10.1016/j.margeo.2014.01.011.

Harris, Peter T., and Tanya Whiteway. 2011. "Global distribution of large submarine canyons: Geomorphic differences between active and passive continental margins." *Marine Geology* 285 (1): 69–86. https://doi.org/10.1016/j.margeo.2011.05.008.

Hasegawa, D, H Yamazaki, RG Lueck, and L Seuront. 2004. "How islands stir and fertilize the upper ocean." *Geophysical Research Letters* 31 (16). https://doi.org/10.1029/2004GL020143.

Heywood, Karen J., Eric D. Barton, and John H. Simpson. 1990. "The effects of flow disturbance by an oceanic island." *Journal of Marine Research* 48 (1): 55–73. https://doi.org/10.1357/002224090784984623.

Heywood, Karen J., David P. Stevens, and Grant R. Bigg. 1996. "Eddy formation behind the tropical island of Aldabra." *Deep Sea Research Part I: Oceanographic Research Papers* 43 (4): 555–578. https://doi.org/10.1016/0967-0637(96)00097-0.

Hogg, Nelson, Pierre Biscaye, Wilford Gardner, and William Schmitz. 1982. "On the transport and modification of Antarctic Bottom Water in the Vema Channel." *Journal of Marine Research* 40 (S).

Holmes, R. M., and Trevor J. McDougall. 2020. "Diapycnal Transport near a Sloping Bottom Boundary." *Journal of Physical Oceanography* 50 (11): 3253–3266. https://doi.org/10.1175/JPO-D-20-0066.1.

Holmes, Ryan M, Casimir de Lavergne, and Trevor J McDougall. 2019. "Tracer Transport within Abyssal Mixing Layers." *Journal of Physical Oceanography* 49 (10): 2669–2695. https://doi.org/10.1175/JPO-D-19-0006.1.

Hotchkiss, Frances S., and Carl Wunsch. 1982. "Internal Waves in Hudson Canyon with Possible Geological Implications." *Deep Sea Research Part A. Oceanographic Research Papers* 29 (4): 415–442. https://doi.org/10.1016/0198-0149(82)90068-1.

Houghton, Robert W., and Cheng Ho. 2001. "Diapycnal Flow through the Georges Bank Tidal Front: A Dye Tracer Study." *Geophysical Research Letters* 28 (1): 33–36. https://doi.org/10.1029/2000GL012298.

Ivey, Gregory N., Cynthia E. Bluteau, Bishakhdatta Gayen, Nicole L. Jones, and Taimoor Sohail. 2021. "Roles of Shear and Convection in Driving Mixing in the Ocean." *Geophysical Research Letters* 48 (3). https://doi.org/10.1029/2020GL089455.

Johnston, DW, and AJ Read. 2007. "Flow-field observations of a tidally driven island wake used by marine mammals in the Bay of Fundy, Canada." *Fisheries Oceanography* 16 (5): 422–435. https://doi.org/10.1111/j.1365-2419.2007.00444.x.

Johnston, Shaun, Jennifer MacKinnon, Patrick Colin, Patrick Haley, Pierre Lermusiaux, Andrew Lucas, Mark Merrifield, Sophia Merrifield, Chris Mirabito, Jonathan, Celia Ou, Mika Siegelman, Eric Terrill, and Amy Waterhouse. 2019. "Energy and Momentum Lost to Wake Eddies and Lee Waves Generated by the North Equatorial Current and Tidal Flows at Peleliu, Palau." *Oceanography* 32 (4): 110–125. https://doi.org/10.5670/oceanog.2019.417.

Klymak, Jody M., M. H. Alford, R Pinkel, R C Lien, and Y J Yang. 2011. "The breaking and scattering of the internal tide on a continental slope." *Journal of Physical Oceanography* 41 (5): 926–945. https://doi.org/doi.org/10.1175/2010JPO4500.1.

Klymak, Jody M., and Michael C. Gregg. 2004. "Tidally generated turbulence over the Knight Inlet sill." *Journal of Physical Oceanography* 34:1135–1152. https://doi.org/10.1175/1520-0485(2004)034<1135:TGTOTK>2.0.CO;2.

Klymak, Jody M., Sonya Legg, Matthew H Alford, Maarten Buijsman, Robert Pinkel, and Jonathan D Nash. 2012. "The direct breaking of internal waves at steep topography." *Oceanography* 25 (2): 150–159. https://doi.org/10.5670/oceanog.2012.50.

Klymak, Jody M., Sonya Legg, and Robert Pinkel. 2010. "High-Mode Stationary Waves in Stratified Flow over Large Obstacles." *Journal of Fluid Mechanics* 644:321–336. https://doi.org/10.1017/S0022112009992503.

Klymak, Jody M., Robert Pinkel, and Luc Rainville. 2008. "Direct Breaking of the Internal Tide near Topography: Kaena Ridge, Hawaii." *Journal of Physical Oceanography* 38:380–399. https://doi.org/10.1175/2007JPO3728.1.

Kunze, Eric, Chris MacKay, Erika E. McPhee-Shaw, Katie Morrice, James B. Girton, and Samantha R. Terker. 2012. "Turbulent Mixing and Exchange with Interior Waters on Sloping Boundaries." *Journal of Physical Oceanography* 42 (6): 910–927. https://doi.org/10.1175/JPO-D-11-075.1.

Kunze, Eric, and Thomas B. Sanford. 1996. "Abyssal Mixing: Where It Is Not." *Journal of Physical Oceanography* 26 (10): 2286–2296. https://doi.org/10.1175/1520-0485(1996)026<2286:AMWIIN>2.0.CO;2.

Le Boyer, Arnaud, Matthew H. Alford, Nicole Couto, Michael Goldin, Sean Lastuka, Sara Goheen, San Nguyen, Andrew J. Lucas, and Tyler D. Hennon. 2021. "Modular, Flexible, Low-Cost Microstructure Measurements: The Epsilometer." *Journal of Atmospheric and Oceanic Technology* 38 (3): 657–668. https://doi.org/10.1175/JTECH-D-20-0116.1.

LeBlond, Paul H, and Lawrence A Mysak. 1981. *Waves in the Ocean.* Elsevier.

Ledwell, J. R., E. T. Montgomery, K. L. Polzin, L. C. St Laurent, R. W. Schmitt, and J. M. Toole. 2000. "Evidence for Enhanced Mixing over Rough Topography in the Abyssal Ocean." *Nature* 403:179–182. https://doi.org/10.1038/35003164.

Ledwell, J. R., L. C. St. Laurent, J. B. Girton, and J. M. Toole. 2011. "Diapycnal Mixing in the Antarctic Circumpolar Current." *Journal of Physical Oceanography* 41 (1): 241–246. https://doi.org/10.1175/2010JPO4557.1.

Ledwell, J. R., A. J. Watson, and C. S. Law. 1998. "Mixing of a Tracer in the Pycnocline." *Journal of Geophysical Research* 103:21499–21529. https://doi.org/10.1029/98JC01738.

Ledwell, James R., Timothy F. Duda, Miles A. Sundermeyer, and Harvey E. Seim. 2004. "Mixing in a Coastal Environment: 1. A View from Dye Dispersion." *Journal of Geophysical Research: Oceans* 109 (C10). https://doi.org/10.1029/2003JC002194.

Ledwell, James R., Andrew J. Watson, and Clifford S. Law. 1993. "Evidence for Slow Mixing across the Pycnocline from an Open-Ocean Tracer-Release Experiment." *Nature* 364 (6439): 701–703. https://doi.org/10.1038/364701a0.

Lee, I.-H., R.-C. Lien, J. T. Liu, and W. Chuang. 2009. "Turbulent mixing and internal tides in Gaoping (Kaoping) Submarine Canyon, Taiwan." *Journal of Marine Systems* 76:383–396. https://doi.org/10.1016/j.jmarsys.2007.08.005.

Lien, R C, and M C Gregg. 2000. "Observations of turbulence in a tidal beam and across a coastal ridge." *Journal of Geophysical Research: Oceans* 106 (C3): 4575–4591. https://doi.org/10.1029/2000JC000351.

Lin, Jung-Tai, and Yih-Ho Pao. 1979. "Wakes in stratified fluids." *Annual Review of Fluid Mechanics* 11 (1): 317–338. https://doi.org/10.1146/annurev.fl.11.010179.001533.

Llewellyn Smith, Stefan G, and WR Young. 2003. "Tidal conversion at a very steep ridge." *Journal of Fluid Mechanics* 495:175–191. https://doi.org/10.1017/S0022112003006098.

Lorke, Andreas, Frank Peeters, and Alfred Wüest. 2005. "Shear-Induced Convective Mixing in Bottom Boundary Layers on Slopes." *Limnology and Oceanography* 50 (5): 1612–1619. https://doi.org/10.4319/lo.2005.50.5.1612.

Lueck, Rolf G, and Todd D Mudge. 1997. "Topographically Induced Mixing around a Shallow Seamount." *Science* 276 (5320): 1831–1833. https://doi.org/10.1126/science.276.5320.1831.

Lumpkin, Rick, and Kevin Speer. 2007. "Global Ocean Meridional Overturning." *Journal of Physical Oceanography* 37:2550–2562. https://doi.org/10.1175/JPO3130.1.

Mackinnon, Jennifer A, Matthew H Alford, Gunnar Voet, Kristin L Zeiden, T M Shaun Johnston, Mika Siegelman, Sophia Merrifield, and Mark Merrifield. 2019. "Eddy Wake Generation From Broadband Currents Near Palau." *Journal of Geophysical Research: Oceans,* https://doi.org/10.1029/2019JC014945.

Marques, Olavo B. 2021. "From Large-Scale Internal Tides to Small-Scale Turbulence: Observations on the Continental Slope off Tasmania." PhD diss., UC San Diego.

Mashayek, A., R. Ferrari, S. Merrifield, J. R. Ledwell, L. St Laurent, and A. Naveira Garabato. 2017. "Topographic enhancement of vertical turbulent mixing in the Southern Ocean." *Nature Communications* 8 (1): 14197. https://doi.org/10.1038/ncomms14197.

Mashayek, A., R. Ferrari, G. Vettoretti, and W. R. Peltier. 2013. "The Role of the Geothermal Heat Flux in Driving the Abyssal Ocean Circulation." *Geophysical Research Letters* 40 (12): 3144–3149. https://doi.org/10.1002/grl.50640.

McDougall, Trevor J., and Raffaele Ferrari. 2017. "Abyssal Upwelling and Downwelling Driven by Near-Boundary Mixing." *Journal of Physical Oceanography* 47 (2): 261–283. https://doi.org/10.1175/JPO-D-16-0082.1.

McPhee-Shaw, E. E., R. W. Sternberg, B. Mullenbach, and A. S. Ogston. 2004. "Observations of Intermediate Nepheloid Layers on the Northern California Continental Margin." *Continental Shelf Research* 24 (6): 693–720. https://doi.org/10.1016/j.csr.2004.01.004.

McPhee-Shaw, Erika E., and Eric Kunze. 2002. "Boundary Layer Intrusions from a Sloping Bottom: A Mechanism for Generating Intermediate Nepheloid Layers." *Journal of Geophysical Research: Oceans* 107 (C6): 3-1-3–16. https://doi.org/10.1029/2001JC000801.

McPhee-Shaw, Erika E., Eric Kunze, and James B. Girton. 2021. "Submarine Canyon Oxygen Anomaly Caused by Mixing and Boundary-Interior Exchange." *Geophysical Research Letters* 48 (10). https://doi.org/10.1029/2021GL092995.

Melet, Angelique, Robert Hallberg, Sonya Legg, and Kurt L. Polzin. 2013. "Sensitivity of the Ocean State to the Vertical Distribution of Internal-Tide-Driven Mixing." *Journal of Physical Oceanography* 43 (3): 602–615. https://doi.org/10.1175/JPO-D-12-055.1.

Merrifield, Sophia, Patrick Colin, Thomas Cook, Carlos Garcia-Moreno, Jennifer MacKinnon, Mark Otero, Travis Schramek, Mika Siegelman, Harper Simmons, and Eric Terrill. 2019. "Island Wakes Observed from High-Frequency Current Mapping Radar." *Oceanography* 32 (4): 92–101. https://doi.org/10.5670/oceanog.2019.415.

Meunier, Patrice, Nicolas Boulanger, Xavier Riedinger, and Stéphane Le Dizès. 2010. "Instabilities of a columnar vortex in a stratified fluid." In *IUTAM Symposium on Turbulence in the Atmosphere and Oceans*, 207–215. Springer. https://doi.org/10.1007/978-94-007-0360-5_17.

Miles, John W. 1961. "On the stability of heterogeneous shear flows." *Journal of Fluid Mechanics* 10 (4): 496–508. https://doi.org/10.1017/S0022112061000305.

Miles, John W., and Louis N. Howard. 1964. "Note on a heterogeneous shear flow." *Journal of Fluid Mechanics* 20 (2): 331–336. https://doi.org/10.1017/S0022112064001252.

Molemaker, M. Jeroen, James C. McWilliams, and William K. Dewar. 2015. "Submesoscale Instability and Generation of Mesoscale Anticyclones near a Separation of the California Undercurrent." Publisher: American Meteorological Society, *Journal of Physical Oceanography* 45 (3): 613–629. https://doi.org/10.1175/jpo-d-13-0225.1.

Moum, J. N., and T. R. Osborn. 1986. "Mixing in the Main Thermocline." *Journal of Physical Oceanography* 16 (7): 1250–1259. https://doi.org/10.1175/1520-0485(1986)016<1250:MITMT>2.0.CO;2.

Moum, J. N., A. Perlin, J. M. Klymak, M. D. Levine, T. Boyd, and P. M. Kosro. 2004. "Convectively Driven Mixing in the Bottom Boundary Layer." *Journal of Physical Oceanography* 34 (10): 2189–2202. https://doi.org/10.1175/1520-0485(2004)034<2189:CDMITB>2.0.CO;2.

Moum, JN, and JD Nash. 2009. "Mixing measurements on an equatorial ocean mooring." *Journal of Atmospheric and Oceanic Technology* 26:317–336. https://doi.org/10.1175/2008JTECHO617.1.

Munk, W. H., and C. Wunsch. 1998. "Abyssal Recipes II: Energetics of Tidal and Wind Mixing." *Deep Sea Research Part I: Oceanographic Research Papers* 45:1977–2010. https://doi.org/10.1016/S0967-0637(98)00070-3.

Munk, Walter H. 1966. "Abyssal Recipes." *Deep Sea Research and Oceanographic Abstracts* 13 (4): 707–730. https://doi.org/10.1016/0011-7471(66)90602-4.

Musgrave, R. C., J. A. MacKinnon, R. Pinkel, A. F. Waterhouse, and J. Nash. 2016. "Tidally Driven Processes Leading to Near-Field Turbulence in a Channel at the Crest of the Mendocino Escarpment." *Journal of Physical Oceanography* 46 (4): 1137–1155. https://doi.org/10.1175/JPO-D-15-0021.1.

Nagai, Taira, and Toshiyuki Hibiya. 2015. "Internal tides and associated vertical mixing in the Indonesian Archipelago." *Journal of Geophysical Research: Oceans* 120 (5): 3373–3390.

Nash, J. D., M. H. Alford, E. Kunze, K. Martini, and S. Kelly. 2007. "Hotspots of Deep Ocean Mixing on the Oregon Continental Slope." *Geophysical Research Letters* 34 (1): L01605. https://doi.org/10.1029/2006GL028170.

Nash, Jonathan D., E Kunze, C M Lee, and T B Sanford. 2006. "Structure of the Baroclinic Tide Generated at Kaena Ridge, Hawaii." *Journal of Physical Oceanography* 36 (6): 1123–1135. https://doi.org/10.1175/JPO2883.1.

Nash, Jonathan D., E. Kunze, K. Polzin, J. Toole, and R. Schmitt. 2004. "Internal Tide Reflection and Turbulent Mixing on the Continental Slope." *Journal of Physical Oceanography* 34:1117–1134. https://doi.org/10.1175/1520-0485(2004)034<1117:ITRATM>2.0.CO;2.

Naveira Garabato, Alberto, Carl P Spingys, Matthew H. Alford, Bethan L. Wynne-Cattanach, Kurt L. Polzin, Arnaud Le Boyer, Gunnar Voet, Nicole Couto, Raffaele Ferrari, Henri F. Drake, Xiaozhou Ruan, Herlé Mercier, Marie-José Messias, Hans Van Haren, Bieto Fernandez Castro, and Alexander Forryan. 2024. "Convective Turbulent Mixing Drives Rapid Upwelling along the Ocean's Bottom Boundary." in prep.

Naveira Garabato, Alberto C. 2021. "2021 RRS Discovery Cruise DY132, 19 June 2021 - 29 July 2021, Bottom Boundary Layer Turbulence and Abyssal Recipes (BLT)." *National Oceanography Centre Cruise Report*.

Naveira Garabato, Alberto C, Eleanor E Frajka-Williams, Carl P Spingys, Sonya Legg, Kurt L Polzin, Alexander Forryan, E Povl Abrahamsen, Christian E Buckingham, Stephen M Griffies, Stephen D McPhail, Keith W. Nicholls, Leif N. Thomas, and Michael P. Meredith. 2019. "Rapid Mixing and Exchange of Deep-Ocean Waters in an Abyssal Boundary Current." *Proceedings of the National Academy of Sciences* 116 (27): 13233–13238. https://doi.org/10.1073/pnas.1904087116.

Nazarian, Robert H., and Sonya Legg. 2017. "Internal Wave Scattering in Continental Slope Canyons, Part 1: Theory and Development of a Ray Tracing Algorithm." *Ocean Modelling* 118:1–15. https://doi.org/10.1016/j.ocemod.2017.07.002.

Nikurashin, Maxim, and Sonya Legg. 2011. "A mechanism for local dissipation of internal tides generated at rough topography." *Journal of Physical Oceanography* 41:378–395. https://doi.org/10.1175/2010JPO4522.1.

Osborn, T. R. 1980. "Estimates of the Local Rate of Vertical Diffusion from Dissipation Measurements" [in EN]. Publisher: American Meteorological Society Section: Journal of Physical Oceanography, *Journal of Physical Oceanography* 10 (1): 83–89. https://doi.org/10.1175/1520-0485(1980)010<0083:EOTLRO>2.0.CO;2.

Osborn, Thomas R., and Charles S. Cox. 1972. "Oceanic Fine Structure." *Geophysical Fluid Dynamics* 3 (4): 321–345. https://doi.org/10.1080/03091927208236085.

Pattiaratchi, Charitha, Alec James, and Michael Collins. 1987. "Island wakes and headland eddies: A comparison between remotely sensed data and laboratory experiments." *Journal of Geophysical Research* 92 (C1): 783. https://doi.org/10.1029/JC092iC01p00783.

Pawlak, G., P. MacCready, K. A. Edwards, and R. McCabe. 2003. "Observations on the evolution of tidal vorticity at a stratified deep water headland." *Geophysical Research Letters* 30 (24): 2234–2237. https://doi.org/10.1029/2003GL018092.

Pawlowicz, Rich, Bob Beardsley, and Steve Lentz. 2002. "Classical Tidal Harmonic Analysis Including Error Estimates in MATLAB Using T_TIDE." *Computers & Geosciences* 28 (8): 929–937. https://doi.org/10.1016/S0098-3004(02)00013-4.

Peltier, W. R., and C. P. Caulfield. 2003. "Mixing Efficiency in Stratified Shear Flows." *Annual Review of Fluid Mechanics* 35 (1): 135–167. https://doi.org/10.1146/annurev.fluid.35.101101.161144.

Perfect, B., N. Kumar, and J. J. Riley. 2018. "Vortex Structures in the Wake of an Idealized Seamount in Rotating, Stratified Flow." *Geophysical Research Letters* 45 (17): 9098–9105.

Peterson, Henry G, and Jörn Callies. 2022. "Rapid Spinup and Spindown of Flow along Slopes." *Journal of Physical Oceanography* 52 (4): 579–596. https://doi.org/10.1175/JPO-D-21-0173.1.

Petruncio, Emil T, Jeffrey D Paduan, and Leslie K Rosenfeld. 2002. "Numerical Simulations of the Internal Tide in a Submarine Canyon." *Ocean Modelling* 4 (3): 221–248. https://doi.org/10.1016/S1463-5003(02)00002-1.

Polzin, K. 2004. "Idealized Solutions for the Energy Balance of the Finescale Internal Wave Field." *Journal of Physical Oceanography* 34:231–246. https://doi.org/10.1175/1520-0485(2004)034<0231:ISFTEB>2.0.CO;2.

Polzin, K. L., J. M. Toole, J. R. Ledwell, and R. W. Schmitt. 1997. "Spatial Variability of Turbulent Mixing in the Abyssal Ocean." *Science* 276:93–96. https://doi.org/10.1126/science.276.5309.93.

Polzin, Kurt L., and Trevor J. McDougall. 2022. "Chapter 7 - Mixing at the Ocean's Bottom Boundary." In *Ocean Mixing*, edited by Michael Meredith and Alberto Naveira Garabato, 145–180. Elsevier. https://doi.org/10.1016/B978-0-12-821512-8.00014-1.

Polzin, Kurt L., Alberto C. Naveira Garabato, Tycho N. Huussen, Bernadette M. Sloyan, and Stephanie Waterman. 2014. "Finescale Parameterizations of Turbulent Dissipation." *Journal of Geophysical Research: Oceans* 119 (2): 1383–1419. https://doi.org/10.1002/2013JC008979.

Roughan, Moninya, Amber J Mace, John L Largier, Steven G Morgan, Jennifer L Fisher, and Melissa L Carter. 2005. "Subsurface recirculation and larval retention in the lee of a small headland: a variation on the upwelling shadow theme." *Journal of Geophysical Research: Oceans* 110 (C10). https://doi.org/10.1029/2005JC002898.

Ruan, Xiaozhou, and Jörn Callies. 2020. "Mixing-Driven Mean Flows and Submesoscale Eddies over Mid-Ocean Ridge Flanks and Fracture Zone Canyons." *Journal of Physical Oceanography* 50 (1): 175–195. https://doi.org/10.1175/JPO-D-19-0174.1.

Ruan, Xiaozhou, and Raffaele Ferrari. 2021. "Diagnosing Diapycnal Mixing from Passive Tracers." *Journal of Physical Oceanography* 51 (3): 757–767. https://doi.org/10.1175/JPO-D-20-0194.1.

Ruan, Xiaozhou, Andrew F. Thompson, and John R. Taylor. 2019. "The Evolution and Arrest of a Turbulent Stratified Oceanic Bottom Boundary Layer over a Slope: Downslope Regime." *Journal of Physical Oceanography* 49 (2): 469–487. https://doi.org/10.1175/JPO-D-18-0079.1.

Rudnick, Daniel L, Timothy J Boyd, Russell E Brainard, Glenn S Carter, Gary D Egbert, Michael C Gregg, Peter E Holloway, Jody M Klymak, Eric Kunze, Craig M Lee, et al. 2003. "From Tides to Mixing along the Hawaiian Ridge." *science* 301 (5631): 355–357.

Ryan, Jp, Fp Chavez, and Jg Bellingham. 2005. "Physical-Biological Coupling in Monterey Bay, California: Topographic Influences on Phytoplankton Ecology." *Marine Ecology Progress Series* 287:23–32. https://doi.org/10.3354/meps287023.

Saenko, O. A., and W. J. Merryfield. 2005. "On the Effect of Topographically Enhanced Mixing on the Global Ocean Circulation." *Journal of Physical Oceanography* 35 (5): 826–835. https://doi.org/10.1175/JPO2722.1.

Schönau, Martha C, and Daniel L Rudnick. 2015. "Glider observations of the North Equatorial Current in the western tropical Pacific." *Journal of Geophysical Research: Oceans* 120 (5): 3586–3605. https://doi.org/10.1002/2014JC010595.

Seim, Knut S., and Ilker Fer. 2011. "Mixing in the Stratified Interface of the Faroe Bank Channel Overflow: The Role of Transverse Circulation and Internal Waves." *Journal of Geophysical Research: Oceans* 116 (C7): 2010JC006805. https://doi.org/10.1029/2010JC006805.

Siegelman, Mika, Mark Merrifield, Eric Firing, Jennifer MacKinnon, Matthew H. Alford, Gunnar Voet, Hemantha Wijesekera, Travis Schramek, Kristin Zeiden, and Eric Terrill. 2019. "Observations of Near-Inertial Surface Currents at Palau." *Oceanography* 32 (4): 74–83. https://doi.org/10.5670/oceanog.2019.413.

Signell, Richard P., and W. Rockwell Geyer. 1991. "Transient Eddy Formation Around Headlands." *Journal of Geophysical Research: Oceans* 96 (C2): 2561–2575. https://doi.org/10.1029/90JC02029.

Simmons, Harper, Brian Powell, Sophia Merrifield, Sarah Zedler, and Patrick Colin. 2019. "Dynamical Downscaling of Equatorial Flow Response to Palau." *Oceanography* 32 (4): 84–91. https://doi.org/10.5670/oceanog.2019.414.

Spingys, Carl P., Alberto C. Naveira Garabato, Sonya Legg, Kurt L. Polzin, E. Povl Abrahamsen, Christian E. Buckingham, Alexander Forryan, and Eleanor E. Frajka-Williams. 2021. "Mixing and Transformation in a Deep Western Boundary Current: A Case Study." *Journal of Physical Oceanography* 51 (4): 1205–1222. https://doi.org/10.1175/JPO-D-20-0132.1.

St. Laurent, L, J. M. Toole, and R. W. Schmitt. 2001. "Buoyancy Forcing by Turbulence above Rough Topography in the Abyssal Brazil Basin." *Journal of Physical Oceanography* 31:3476–3495. https://doi.org/10.1175/1520-0485(2001)031%3C3476:BFBTAR%3E2.0.CO;2.

St. Laurent, Louis, Takashi Ijichi, Sophia Merrifield, Justin Shapiro, and Harper Simmons. 2019. "Turbulence and Vorticity in the Wake of Palau." *Oceanography* 32 (4): 102–109. https://doi.org/10.5670/oceanog.2019.416.

Talley, Lynne D. 2013. "Closure of the Global Overturning Circulation through the Indian, Pacific, and Southern Oceans: Schematics and Transports." *Oceanography* 26 (1): 80–97.

Taylor, J. R., S. M. de Bruyn Kops, C. P. Caulfield, and P. F. Linden. 2019. "Testing the Assumptions Underlying Ocean Mixing Methodologies Using Direct Numerical Simulations." *Journal of Physical Oceanography* 49 (11): 2761–2779. https://doi.org/10.1175/JPO-D-19-0033.1.

Thurnherr, A. M., L. Clément, L. St. Laurent, R. Ferrari, and T. Ijichi. 2020. "Transformation and Upwelling of Bottom Water in Fracture Zone Valleys." *Journal of Physical Oceanography* 50 (3): 715–726. https://doi.org/10.1175/JPO-D-19-0021.1.

Toole, J. M., K. L. Polzin, and R. W. Schmitt. 1994. "Estimates of Diapycnal Mixing in the Abyssal Ocean." *Science* 264:1120–1123. https://doi.org/10.1126/science.264.5162.1120.

Toole, John M. 2007. "Temporal Characteristics of Abyssal Finescale Motions above Rough Bathymetry." *Journal of Physical Oceanography* 37 (3): 409–427. https://doi.org/10.1175/JPO2988.1.

Umlauf, Lars, and Hans Burchard. 2011. "Diapycnal Transport and Mixing Efficiency in Stratified Boundary Layers near Sloping Topography." *Journal of Physical Oceanography* 41 (2): 329–345. https://doi.org/10.1175/2010JPO4438.1.

van Haren, Hans, and Louis Gostiaux. 2012. "Detailed Internal Wave Mixing above a Deep-Ocean Slope." *Journal of Marine Research* 70 (1): 173–197. https://doi.org/10.1357/002224012800502363.

van Haren, Hans, Furu Mienis, and Gerard Duineveld. 2022. "Contrasting Internal Tide Turbulence in a Tributary of the Whittard Canyon." *Continental Shelf Research* 236:104679. https://doi.org/10.1016/j.csr.2022.104679.

van Haren, Hans, Gunnar Voet, Matthew H. Alford, Bieito Fernández-Castro, Alberto C. Naveira Garabato, Bethan L. Wynne-Cattanach, Herlé Mercier, and Marie-José Messias. Submitted. "Near-Slope Turbulence in a Rockall Canyon." *Deep Sea Research Part I: Oceanographic Research Papers.*

Voet, Gunnar, Matthew H. Alford, Jennifer A. MacKinnon, and Jonathan D. Nash. 2020. "Topographic Form Drag on Tides and Low-Frequency Flow: Observations of Nonlinear Lee Waves over a Tall Submarine Ridge near Palau." *Journal of Physical Oceanography* 50 (5): 1489–1507. https://doi.org/10.1175/JPO-D-19-0257.1.

Wain, D. J., M. C. Gregg, M. H. Alford, R. C. Lien, R. A. Hall, and G. S. Carter. 2013. "Propagation and Dissipation of the Internal Tide in Upper Monterey Canyon." *Journal of Geophysical Research: Oceans* 118 (10): 4855–4877. https://doi.org/10.1002/jgrc.20368.

Wain, Danielle J., and Chris R. Rehmann. 2010. "Transport by an Intrusion Generated by Boundary Mixing in a Lake." *Water Resources Research* 46 (8). https://doi.org/10.1029/2009WR008391.

Waterhouse, Amy F., Jennifer A. Mackinnon, Ruth C. Musgravea, Samuel M. Kelly, Andy Pickering, and Jonathan Nash. 2017. "Internal Tide Convergence and Mixing in a Submarine Canyon." *Journal of Physical Oceanography* 47 (2): 303–322. https://doi.org/10.1175/JPO-D-16-0073.1.

Waterhouse, Amy F., Jennifer A. MacKinnon, Jonathan D. Nash, Matthew H. Alford, Eric Kunze, Harper L. Simmons, Kurt L. Polzin, Louis C. St. Laurent, Oliver M. Sun, Robert Pinkel, Lynne D. Talley, Caitlin B. Whalen, Tycho N. Huussen, Glenn S. Carter, Ilker Fer, Stephanie Waterman, Alberto C. Naveira Garabato, Thomas B. Sanford, and Craig M. Lee. 2014. "Global Patterns of Diapycnal Mixing from Measurements of the Turbulent Dissipation Rate." *Journal of Physical Oceanography* 44 (7): 1854–1872. https://doi.org/10.1175/JPO-D-13-0104.1.

Wesson, Joel C., and Michael C. Gregg. 1994. "Mixing at Camarinal Sill in the Strait of Gibraltar." *Journal of Geophysical Research: Oceans* 99 (C5): 9847–9878. https://doi.org/10.1029/94JC00256.

Wijesekera, Hemantha W., Joel C. Wesson, David W. Wang, William J. Teague, and Z. R. Hallock. 2020. "Observations of Flow Separation and Mixing around the Northern Palau Island/Ridge." *Journal of Physical Oceanography* 50 (9): 2529–2559. https://doi.org/10.1175/JPO-D-19-0291.1.

Winters, K. B. 2015. "Tidally Driven Mixing and Dissipation in the Stratified Boundary Layer above Steep Submarine Topography." *Geophysical Research Letters* 42 (17): 7123–7130. https://doi.org/10.1002/2015GL064676.

Wolanski, Eric, Takashi Asaeda, Akihiro Tanaka, and Eric Deleersnijder. 1996. "Three-dimensional island wakes in the field, laboratory experiments and numerical models." *Continental Shelf Research* 16 (11): 1437–1452. https://doi.org/10.1016/0278-4343(95)00087-9.

Wolanski, Eric, Jorg Imberger, and Malcom Heron. 1984. "Island wakes in shallow coastal waters." *Journal of Geophysical Research: Oceans* 89 (C6): 10553–10569. https://doi.org/10.1029/JC089iC06p10553.

Wunsch, C., and R. Ferrari. 2004. "Vertical Mixing, Energy and the General Circulation of the Oceans." *Annual Review of Fluid Mechanics* 36:281–314. https://doi.org/10.1146/annurev.fluid.36.050802.122121.

Wynne-Cattanach, Bethan, Matthew Alford, Nicole Couto, Henri Drake, Raffaele Ferrari, Arnaud Le Boyer, Herle Mercier, Marie-Jose Messias, Alberto Naveira Garabato, Kurt Polzin, Xiaozhou Ruan, Carl Spingys, Hans van Haren, and Gunnar Voet. 2023. *Observational Evidence of Diapycnal Upwelling within a Sloping Submarine Canyon.* Preprint. In Review. https://doi.org/10.21203/rs.3.rs-3459062/v1.

Zeiden, Kristin L., Jennifer A. MacKinnon, Matthew H. Alford, Daniel L. Rudnick, Gunnar Voet, and Hemantha Wijesekera. 2021. "Broadband Submesoscale Vorticity Generated by Flow around an Island." *Journal of Physical Oceanography* 51 (4): 1301–1317. https://doi.org/10.1175/JPO-D-20-0161.1.

Zeiden, Kristin L., Daniel L. Rudnick, and Jennifer A. MacKinnon. 2019. "Glider Observations of a Mesoscale Oceanic Island Wake." *Journal of Physical Oceanography* 49 (9): 2217–2235. https://doi.org/10.1175/JPO-D-18-0233.1.

Zhao, Zhongxiang, Matthew H. Alford, Ren-Chieh Lien, Michael C. Gregg, and Glenn S. Carter. 2012. "Internal tides and mixing in a submarine canyon with time-varying stratification." *Journal of Physical Oceanography* 42:2121–2142. https://doi.org/10.1175/JPO-D-12-045.1.